

UCSF

UC San Francisco Electronic Theses and Dissertations

Title

Application of perfusion-weighted, susceptibility-weighted, and spectroscopic magnetic resonance imaging for characterizing glioma microvasculature at different field strengths

Permalink

<https://escholarship.org/uc/item/4935g8cm>

Author

Lupo, Janine Marie

Publication Date

2006

Peer reviewed|Thesis/dissertation

Application of Perfusion-Weighted, Susceptibility-Weighted, and Spectroscopic Magnetic Resonance Imaging for Characterizing Glioma Microvasculature at Different Field Strengths

by

Janine Marie Lupo

DISSERTATION

Submitted in partial satisfaction of the requirements for the degree of

DOCTOR OF PHILOSOPHY

in

Bioengineering

in the

GRADUATE DIVISIONS

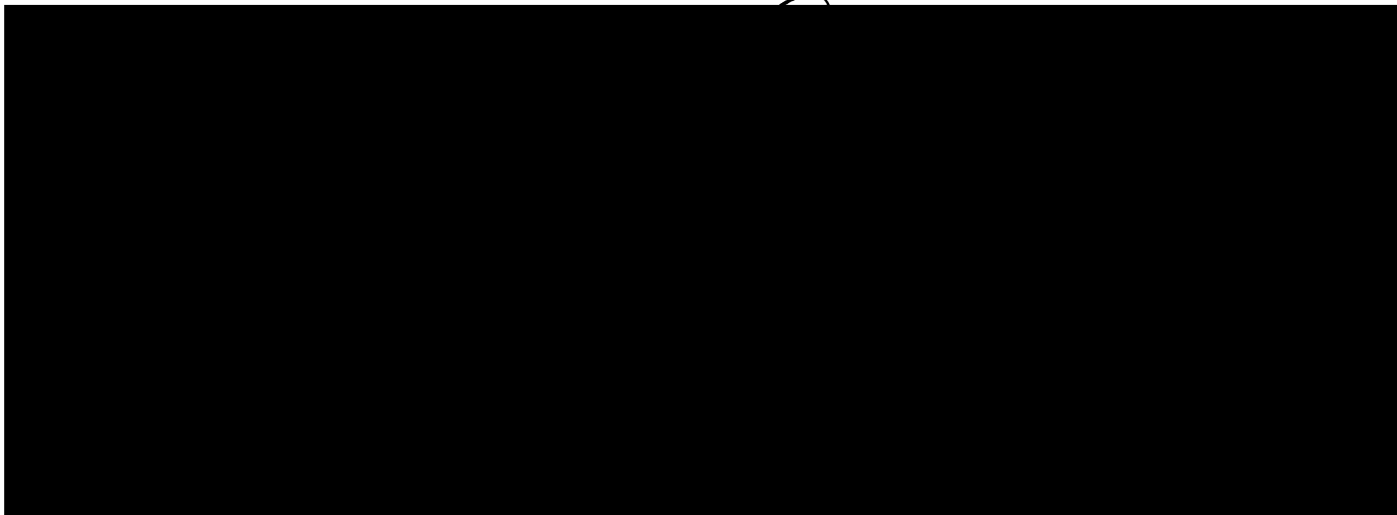
of the

UNIVERSITY OF CALIFORNIA SAN FRANCISCO

and

UNIVERSITY OF CALIFORNIA BERKELEY

UNIVERSITY LIBRARY



Date

University Librarian

Degree Conferred:

Acknowledgements

Above all, to Sarah Nelson, whose endless guidance, encouragement, and support over the years have allowed me to grow as both a scientist and an individual. She has been a wonderful role model whose positive outlook and amazing mentoring skills will continue to impact my life in years to come.

To Mike Lee and Esin Ozturk for being there in every way throughout my entire graduate school experience, for teaching me patience, for always knowing what I'm thinking, for sharing everything from ideas and opinions, to Matlab tricks and day-to-day problems, to food and hobbies,

To Radhika Srinivasan, Joonmi Oh, Xiaojuan Li, and Annette Chan for all their advice and helpful discussions when I first started my Ph.D.,

To Pieter Pels, Joe Osorio, Yan Li, Inas Khayal, Matt Zierhut, Kate Hammond, Paul DiCamillo, Il Woo Park, Forrest Crawford, Rebeca Choy, Jason Crane, and Suja Saraswathy for their constant support, coffee breaks, and contributions to an enjoyable working environment,

To Soonmee Cha and Sharmila Majumdar for sitting on both my quals and thesis committees, for always being themselves no matter who's watching, and for never ceasing to make me laugh,

To Dan Vigneron and Roland Henry for sitting on my quals committee and teaching me that a life in science can be fun,

To Andrea Pirzkall and Susan Chang for all their clinical insight and collaborations,

To Suchandrima Banerjee, Duan Xu, Tim Dunn, Meredith Metcalf, and Albert Chen for always being there to help with pulse sequence development, scanning, or explaining new concepts,

To Niles Bruce and Bert Jimenez for providing humor while scanning,

To Eric Han and Doug Kelley from GE Healthcare who always find the time to answer my never-ending list of questions,

To my roommates Jill and Johanna for always being there when I needed them,

And finally, to all of my parents, Gloria, Frank, Marie, and Rick, for all their love, support, and encouragement over the years no matter how far the distance,

Thank you.

Grant funding for this thesis project was provided by the University of California Discovery Grant with GE Healthcare LSIT-01-10107, the National Cancer Institute SPORE grant P50 CA97297, and the National Institutes of Health grant R01 CA59880.

11007 11000000

Abstract

Application of Perfusion-Weighted, Susceptibility-Weighted, and Spectroscopic Magnetic Resonance Imaging (MRI) for Characterizing Glioma Microvasculature at Different Field Strengths

by

Janine Marie Lupo

The advent of new anti-angiogenic therapies has necessitated the ability to characterize the spatial distribution of abnormal vascularity in heterogeneous high-grade gliomas. The most widespread method for assessing leakage of the blood-brain-barrier (BBB) has been the presence of increased signal intensity on T1-weighted images after an injection of a gadolinium-based contrast agent. However, this type of conventional anatomical imaging is extremely limited in delineating tumor boundaries and assessing hemodynamic function.

Perfusion MRI parameters corresponding to the peak height and percent recovery of the T2* relaxivity curve were investigated to characterize angiogenesis and microvascular leakage within the T2 and contrast-enhancing abnormalities in high-grade gliomas. Areas of BBB breakdown were found outside the contrast enhancing lesion, with grade 4 gliomas experiencing heightened leakage compared to their grade III counterparts. The addition of metabolite levels from lactate-edited spectroscopic MRI within regions of abnormal perfusion revealed elevated lactate and decreased creatine levels for grade IV gliomas only within regions of abnormal leakage, confirming reduced oxygenation where vascular integrity is compromised.

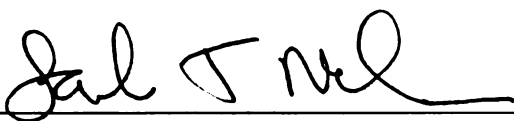
11007 11007A

The implementation of parallel imaging methods such as Sensitivity Encoding (SENSE) to perfusion MRI can reduce the heightened susceptibility artifacts inherent at higher field strengths. This approach yielded a significant elevation in dynamic signal-to-noise-ratio with improved slice coverage at 3T compared to the 1.5T acquisition. A considerable reduction in geometric distortion and signal dropout was achieved with SENSE compared to the standard 8-channel coil acquisition at 3T.

Susceptibility-weighted imaging (SWI), a method for high resolution vascular imaging was employed at 3T and 7T. Applying SENSE at 3T allowed for a two-fold acceleration in scan time without significantly affecting small or vessel contrast. The increased susceptibility inherent at 7T provided heightened vessel contrast and improved the detection of smaller vessels. High correlations were found between vessel volume estimates from SWI and cerebral blood volume calculations from perfusion MRI in high-grade glioma patients at 3T.

This project integrated perfusion-weighted, susceptibility-weighted, and spectroscopic MRI to provide insight into glioma microvasculature physiology at various field strengths. These advanced imaging strategies have been translated into the clinical environment where they have the potential to further impact patient management.

Approved by Sarah J. Nelson, Ph.D.


_____ 8/18/06
date

11/27/06

Table of Contents

Acknowledgements	iii
Abstract	v
Table of Contents	vii
List of Tables	x
List of Figures	xi
1. Introduction	1
2. Background	6
2.1 Brain Tumors	6
<i>Pathology and Classification of Gliomas</i>	7
2.2 Tumor Microvasculature and Angiogenesis	8
2.3 MRI for the Clinical Evaluation of Brain Tumors	10
<i>Signal Formation and Spatial Localization</i>	10
<i>Relaxation and Image Contrast</i>	11
2.4 Treatment Strategies	14
3. Characterization of Spatial Heterogeneity in High-Grade Gliomas Using Dynamic Susceptibility-Contrast Perfusion Imaging	16
3.1 Perfusion-Weighted Imaging of Brain Tumors	16
<i>Basic Principles of Tracer Kinetics</i>	16
<i>Dynamic Susceptibility-Contrast Perfusion and Echo Planar Imaging</i>	20
<i>Cerebral Blood Volume Calculation</i>	24
3.2 Methods	26
<i>Patients</i>	26
<i>MRI Acquisition</i>	26
<i>Image Processing</i>	27
<i>Analysis of T2* Signal-Intensity Time Curves</i>	28
3.3 Results	31
<i>Volumes with Abnormal Perfusion</i>	32
<i>Peak Height</i>	33
<i>Percent Recovery</i>	33
3.4 Discussion and Conclusions	35

11067 1100001

4. Analysis of Metabolic Indices in Regions of Abnormal Perfusion in High-Grade Glioma Patients	41
4.1 3D ¹ H Magnetic Resonance Spectroscopic Imaging	41
<i>Magnetic Resonance Spectroscopy and Detectable Metabolites</i>	<i>41</i>
<i>Signal Localization and Magnetic Resonance Spectroscopic Imaging</i>	<i>42</i>
<i>Lactate-Edited MRSI</i>	<i>44</i>
<i>Assessment of Tumor Oxygenation</i>	<i>45</i>
4.2 Methods	46
<i>Patients</i>	<i>46</i>
<i>MR Imaging and Spectroscopic Acquisition</i>	<i>46</i>
<i>Image and Spectra Post-Processing</i>	<i>47</i>
<i>Statistical Analysis</i>	<i>49</i>
4.3 Results	50
4.4 Discussion and Conclusions	55
5. Dynamic Susceptibility-Contrast Perfusion MR Imaging at 3T	60
5.1 Background	60
<i>Limitations of Echo Planar Imaging</i>	<i>60</i>
<i>Partially Parallel Imaging</i>	<i>62</i>
<i>Effects of Parallel Imaging on EPI Artifacts</i>	<i>63</i>
<i>Sensitivity Encoding</i>	<i>63</i>
<i>SNR Concerns with SENSE</i>	<i>65</i>
5.2 Estimation of Dynamic SNR and Effects of T1 Relaxation	66
<i>Patient Population and Imaging Acquisition</i>	<i>66</i>
<i>Region Definition</i>	<i>67</i>
<i>Dynamic and Image SNR Calculations</i>	<i>68</i>
<i>Results</i>	<i>69</i>
5.3 Quantification of Geometric Distortion with Non-rigid Registration	73
5.4 Assessment of Susceptibility-Induced Artifacts	75
5.5 Discussion and Conclusions	81
6. Extension of Parallel Imaging Techniques for Susceptibility-Weighted Imaging at Higher Fields (3T and 7T)	87
6.1 Background	87
<i>Blood Vessel Imaging Based on Susceptibility</i>	<i>87</i>
<i>Application of SENSE to SWI</i>	<i>90</i>

11007 1100101

List of Tables

Table 2.1. Effects of acquisition parameters on image contrast	13
Table 3.1. Volumes of abnormality expressed as a percentage of the T2 lesion, for grade III and grade IV gliomas	31
Table 3.2. Relative peak height values within the CEL and T2–CEL for grade III and grade IV gliomas	34
Table 3.3. Percent recovery values within the CEL and T2–CEL for grade III and grade IV gliomas	34
Table 3.4. Relative mean peak height and percent recovery values for all voxels within the CEL and T2–CEL combined across grade III and grade IV patients	35
Table 3.5. Relative peak height and percent recovery values for the T2L of non-enhancing grade III patients compared to the T2–CEL of grade IV patients	35
Table 4.1. Volumes of abnormal perfusion and T2h regions expressed as a percentage of the total T2 lesion volume within the PRESS box	51
Table 4.2. Mean metabolite levels within abnormal perfusion and T2h regions compared to contralateral NAWM for grade IV gliomas	54
Table 4.3. Mean metabolite levels within abnormal perfusion and T2h regions compared to contralateral NAWM for grade III gliomas	55
Table 4.4. Comparison of mean metabolite levels within abnormal perfusion and T2h regions from voxels across all patients of each grade	55
Table 5.1. Dynamic SNR, post-bolus SNR, and dynamic to post-bolus SNR ratio in NABT and NAWM regions	71
Table 5.2. Histogram-derived indices of dynamic SNR for each acquisition	72
Table 5.3. Histogram-derived indices of image SNR for each acquisition	72
Table 5.4. Histogram-derived indices of frequency magnitude displacement in mm for the whole brain region	78
Table 5.5. Histogram-derived indices of magnitude displacement in mm for the rim region	79
Table 6.1. SWI scan parameters at 3T and 7T	92
Table 6.2. Mean large and small vessel contrast at 3T and 7T	103
Table 7.1. Correlation results of rCBV with SWI vessel fraction	114

List of Figures

Figure 2.1. Illustration of blood-brain barrier components	9
Figure 2.2. T1 relaxation (left) and T2 relaxation (right) curves for two tissues	12
Figure 2.3. a) T1-weighted image post-gadolinium, b) T2-weighted image, and c) PD-weighted images of a high grade gliomas	13
Figure 3.1. Diagram of tracer distribution in tissue	17
Figure 3.2. Bi-compartmental model of tracer distribution for T2* methods	19
Figure 3.3. Normal and abnormal T2* signal-time intensity curves for different brain regions	21
Figure 3.4. Single-shot gradient echo EPI pulse sequence and corresponding k-space trajectory	22
Figure 3.5. Diagram of spin echo and gradient echo pulse sequences	23
Figure 3.6. Effects of sequence and flip angle selection on rCBV estimation	24
Figure 3.7. Depiction of post-processing steps for analyzing T2* signal-intensity time curves	29
Figure 3.8. Example of abnormal peak height (aPH; <i>left</i>) and abnormal recovery (aRec; <i>center</i>) maps for grade IV (<i>top</i>) and grade III (<i>bottom</i>) gliomas overlaid on a T2-weighted image (<i>top</i> – FSE, <i>bottom</i> – FLAIR) and the $\Delta R2^*$ curves from which they were derived (<i>right</i>)	32
Figure 4.1. Spectra from normal appearing brain tissue, contralateral from tumor location, and voxel from central tumor region in a patient with grade IV gliomas	42
Figure 4.2. Diagram of PRESS pulse sequence for localization of spectra	43
Figure 4.3. Summary of spectral post-processing	44
Figure 4.4. Illustration of lactate-edited spectral acquisition cycles	45
Figure 4.5. Heterogeneity in the distribution of abnormal perfusion regions within a representative grade IV glioma	51
Figure 4.6. Spectral patterns and regions of abnormal perfusion for a representative non-enhancing grade III patient	52

100% LIBRARY

Figure 4.7. Perfusion-derived non-parametric maps of a) peak height and b) percent recovery overlaid on post-contrast T1-weighted images with c) corresponding $\Delta R2^*$ curves for a representative grade IV glioma. In d-f, corresponding metabolite maps of d) choline, e) creatine, and f) lactate	53
Figure 5.1. Illustration of SENSE for a reduction factor of two	64
Figure 5.2. Acquisition subgroups and scan parameters	67
Figure 5.3. Generation of NAWM and NABT regions used in dynamic SNR estimation	68
Figure 5.4. First time point pre-contrast EPI volume with rCBV map overlay and corresponding white matter $\Delta R2^*$ curves for (a) quadrature coil at 1.5T, (b) quadrature coil at 3T, (c) 8-channel coil at 3T, and (d) 8-channel coil with SENSE at 3T	70
Figure 5.5. Whole brain histograms of (a) image SNR and (b) dynamic SNR	71
Figure 5.6. Depiction of geometric distortion and signal dropout in representative echo planar images obtained from the same brain tumor patient	76
Figure 5.7: Axial distortion maps depicting the inverse transformation of the standard EPI acquisition for (a) the frequency encode direction (L/R) and (b) phase encode direction (A/P)	77
Figure 5.8: Displacement histograms for (a) the frequency encode direction (L/R) and (b) phase encode direction (A/P), plotted on a semi-logarithmic scale	78
Figure 5.9: 2D histograms showing the relationship between displacement values for the standard and SENSE EPI acquisitions in the (a) readout and (b) phase-encode directions for all patients	80
Figure 6.1. Depiction of processing steps involved in SWI	94
Figure 6.2. Importance of coil intensity correction and mIPs in small vessel detection at 7T	96
Figure 6.3. Depiction of brain regions used to generate contrast ratios for a) large vessels (green) and b) small vessels (pink)	99
Figure 6.4. Echo time selection for maximum susceptibility weighting of venous vessels as a function of field strength	101
Figure 6.5. GRE SWI with mIP=15mm at 7T for different TEs, enlarged on right for TE=12 & 16 ms	102
Figure 6.6. Final SWI images for each acquisition at 3T (left) and 7T (right) for the same volunteer	103

NAWM NABT
 100% 100%
 100% 100%

Figure 6.7. SPGR SWI images at 3T (left) and 7T (right), enlarged to view small vessels 104

Figure 7.1. SWI post-processing steps with phase unwrapping and low pass filter subtraction for multi-channel coil combination 110

Figure 7.2. rCBV maps overlaid on SWI images (color), anatomic images (center), and original SWI images, for different slices (a-c) of a patient with GBM.. 113

Figure 7.3. rCBV as a function of the fraction of vessels estimated from SWI within the whole brain, normal appearing brain tissue, and tumor for a grade 4 glioma patient 114

UCSF LIBRARY

Chapter 1: Introduction

An estimated 43,800 new cases of primary brain and central nervous system tumors were diagnosed in the United States in 2005, 58% of which occurred in males (1). Gliomas are the most common type primary brain tumors, ranging from benign to highly malignant lesions with extremely heterogeneous vascular characteristics, cell density, and infiltrative potential. The ability to distinguish between different types of gliomas as well as providing an estimate of their malignancy is of great importance since initial prognosis dictates both survival and course of treatment. Grade IV gliomas, or glioblastoma multiforme (GBM), are the most malignant brain tumor, with average survival of only 9 months to a year, and decreasing grade corresponding to lower severity (1).

Magnetic resonance imaging (MRI) is a well-established technique for in vivo visualization of brain tumors due to its superior ability to generate contrast within soft tissue. Clinical use of MRI as a noninvasive tool to image brain pathology has steadily gained popularity since it was first introduced in the early 1970s. The fact that it does not require ionizing radiation facilitates the routine usage of MRI in diagnosis, treatment planning, and monitoring response to therapy. Although effective in characterizing anatomic transformations, research is continually evolving to uncover new ways to understand the underlying functional alterations that give rise to the pathologic morphology, which would improve early disease detection, increase the potential of more effective therapy, enhance the quality of life, and extend survival.

UIC LIBRARY

Although excellent at generating high resolution images of anatomy with flexibility in creating various contrast mechanisms, conventional MRI methods are not always able to fully characterize differences in tumor types, disease progression, and effectiveness of therapy. The interpretation of these data is also highly subjective. Within brain tumor lesions there is heterogeneity and microscopic infiltrative tumor may spread beyond the region of abnormality defined by anatomical images and be confused with areas of inflammation, necrosis, and response to radiation treatment. Thus, the need arises for more quantitative measures to aid in diagnosis and more closely monitor changes in brain tissue.

One functional in vivo imaging technique that has been proposed as a tool for distinguishing between active tumor, necrosis, and edema is Magnetic Resonance Spectroscopic Imaging (MRSI). Recent studies have shown that MRSI provides vital information about the spatial extent and degree of metabolic activity of gliomas which is undetectable with conventional MRI methods (2). Limitations of this technique include the inability to always cover the entire lesion, coarse spatial resolution, and long acquisition times. Although MRSI is an excellent tool for elucidating the cellular metabolite levels in brain tissue, it does not provide a direct measurement of changes in tumor vasculature that result in the recruitment of new vessels to meet the oxygen demands of a rapidly growing tumor and result in blood-brain-barrier breakdown.

With the advent of new anti-angiogenic therapies for the treatment of brain tumors, it is becoming increasingly important to add specificity to the classification of high-grade gliomas by including information based upon vasculature characteristics. Dynamic susceptibility-contrast, perfusion-weighted MRI (DSC MRI) was introduced in the mid-1990's and facilitates the tracking of a contrast agent bolus through the

10/10/10
10/10/10
10/10/10
10/10/10

susceptibility-induced signal dropout and geometric distortions inherent to the EPI pulse sequence can confound accurate quantitation of vascular parameters making it difficult to align dynamic data to structural images. Implementation of partially-parallel imaging methods with multi-channel phased-array coils can reduce these artifacts associated with dynamic perfusion imaging, as well as shorten the long acquisition times required for susceptibility-weighted imaging (SWI) to be applicable in a clinical setting (8-10).

The goal of this project was to develop and apply acquisition, reconstruction, and post processing methods to improve the characterization of vascular structure and function within heterogeneous high-grade gliomas. This included the implementation of new strategies that allowed new vascular imaging techniques to come into fruition with the transition to high field scanners that were feasible to be routinely used clinically and capable of probing structural and functional properties of vasculature within brain tumors. This thesis is organized according to the following chapters that individually review the many facets that comprise the goal. Specifically:

Chapter 2 provides a brief overview of relevant background on brain tumors and vasculature properties characteristic of high-grade gliomas, as well as describing the current use of MRI as a diagnostic tool in the clinic.

Chapter 3 introduces the first vascular imaging technique, DSC perfusion MRI, to probe the functionality of vasculature in high-grade gliomas. A novel, non-parametric approach that analyzes shape characteristics of raw dynamic perfusion curves on a voxel by voxel basis to separately investigate vascular integrity and blood vessel volume in heterogeneous tumor regions is described.

10211821

Chapter 2: Background

This chapter begins by providing an overview of the basic characteristics of primary brain tumors, with a special focus on vascular properties. A brief review of fundamental MR physics and imaging principles is then presented with focus on relevant parameters for imaging brain tumors.

2.1 Brain Tumors

The annual incidence of brain tumors in the United States is 15-20 cases per 100,000 people, with primary gliomas as the most common type in adults (11). Patients usually present with symptoms such as headache, vomiting, disequilibrium, and seizures with no focal onset. Intra cranial brain neoplasms comprise primary and metastatic brain tumors and are further classified based on their cellular origin. Primary brain tumors differ from other types tumors in that they are nonmetastatic, infiltrative, and difficult to treat because of the blood-brain-barrier may prevent drugs from accessing tumor cells. About half of newly diagnosed brain tumors are primary, with the most prevalent type originating from glial cells and constituting more than 90% in adults (12). These tumors are extremely heterogeneous, ranging from benign to highly malignant lesions with varying vasculature, cell density, and infiltrative potential and are the third most common cancer related death in young patients under the age of 35 (11). The ability to distinguish between different types of gliomas as well as providing an estimate of their malignancy is of great importance.

Pathology and Classification of Gliomas

Gliomas, are named due to their origin from neuroglia, the support cells of the brain. Glial cells can be classified into four major subtypes each with their own unique functional role: astrocytes, oligodendrocytes, microglia, and ependymal cells. Astrocytes are the most abundant of these cell types and consequently have the most diverse function, including structural support of neurons and other central nervous system components, neurotransmitter metabolism to maintain the chemical environment within the synapse, transfer of nutritive substances to neurons, provision of pathways for neuronal migration, and participation in repair and regeneration. The monitoring of ionic and molecular contents of extracellular space is carried out by reactive astrocytes when the brain is injured. Oligodendrocytes can be found close to the neuronal cell membranes or adjacent to axons where they play an important role in myelin production. Similar to macrophages but smaller, microglial cells respond to injury by digesting cell debris through phagocytosis. Ependymal cells line the ventricles and central canal of the spinal cord, forming the blood- cerebral spinal fluid (CSF) barrier.

The terminology for classifying gliomas is based on the glial cell from which the tumor originates. Astrocytomas comprise the largest group of primary brain tumors (75% of gliomas) and are further classified by their extent of astrocytic differentiation, with anaplastic astrocytomas being the more aggressive type of tumor (13). Pilocytic astrocytomas, most commonly found in children, are often benign. Oligodendrogliomas tend to align along fiber tracts and have a more favorable prognosis than histologically similar astrocytomas, even though they are more likely to enhance at an earlier stage. It is also possible for a glioma to contain mixed

WEST LIBRARY

oligodendric and astrocytic components, and in which case the term oligoastrocytoma is utilized.

Grading of gliomas is based on the degree of malignancy or aggressiveness that the tumor exhibits in terms of the microscopic appearance of biopsy samples. The World Health Organization formulated a set of criteria (WHO II) for stratifying tumors into four grades based on the level of invasiveness, growth rate patterns, abnormal vascularity, and similarity to normal cells. A grade I tumor is slow growing, lacks all the aforementioned characteristics, and is considered benign since it rarely spreads. The most common example is juvenile pilocytic astrocytoma. Grade II tumors are also deemed low-grade, but exhibit nuclear atypia and can progress if left untreated. The presence of mitotic figures necessitates the diagnosis of a grade III glioma, often termed anaplastic astrocytomas (AA) for their higher cellularity and vascularity than grade II lesions. The distinction between grade III and grade IV glioma is based upon the presence of necrosis. Grade IV gliomas, or glioblastoma multiforme (GBM), also exhibit increased microvascular proliferation and have larger infiltrative potential. AA and GBMs are collectively referred to as high-grade gliomas because they are difficult to differentiate based on radiographical appearance. (13,14)

2.2 Tumor Microvasculature and Angiogenesis

The brain harbors complicated vasculature with branching architecture that is capable of penetrating various levels of tissue to ensure a blood supply highly enriched with nutrients and oxygen, which supports the high metabolic demands of rapidly firing neurons and supporting neuroglia. The physiological boundary between the blood within the vessels and surrounding brain tissue and CSF is

10071001001

known as the blood-brain-barrier (BBB). This conceptual “barrier” or extra lining of blood vessel walls is unique to the brain where it is especially important to maintain a constant environment protected from any foreign substances that may enter the bloodstream. The layers that constitute the BBB are illustrated in Figure 2.1 and are uniquely comprised of endothelial cells with tight junctions, pericytes to regulate them, thin continuous basal lamina or basement membranes, and astrocytic “foot” processes that surround the capillaries.

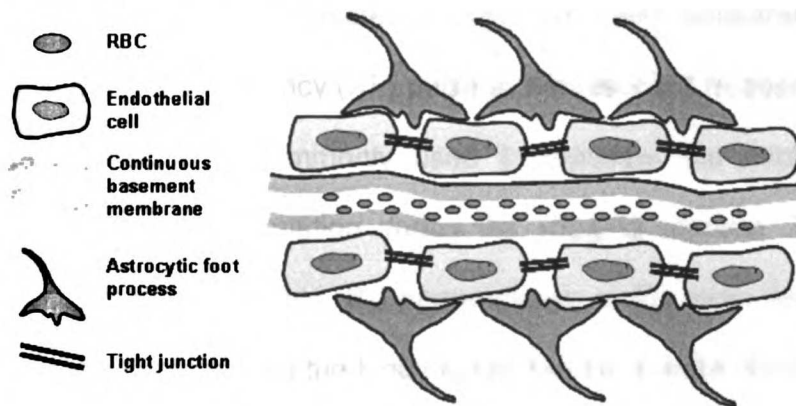


Figure 2.1: Illustration of blood-brain barrier components

As gliomas grow and progress to a higher grade, the vascular supply is no longer adequate to support the increasing metabolic demands of the rapidly proliferating tumor cells (15). Regional hypoxia then ensues, leading to the upregulation of vasoactive endothelial growth factor (VEGF) and the promotion of new blood vessel formation from the existing vasculature, a phenomena known as angiogenesis (16-19). The new vessels that are formed often lack the complex structure of the normal brain vasculature and result in endothelial permeability. Tumor growth can also damage the existing vasculature and promote blood-brain-barrier breakdown which also causes increased microvascular leakage (20).

UCSF LIBRARY

at multiple amplitudes for each frequency encoded line that is read out until an entire plane of k-space, or frequency space, is acquired. Each point in k-space is thus assigned a unique frequency that can be mapped to its corresponding position in the image via an inverse Fourier transform.

Relaxation and Image Contrast

After an RF pulse is applied to excite a slice or slab of tissue, two types of relaxation occur: 1) T1 relaxation, which describes the regrowth of longitudinal magnetization (M_z), and 2) T2 relaxation, or the loss of transverse magnetization (M_{xy}) due to dephasing. These two independent processes occur simultaneously and together determine the contrast of an image. T1 relaxation is also known as spin-lattice relaxation because it characterizes the rate in which excited nuclei return to their equilibrium state through loss of energy to the surrounding environment. The time it takes for 63% of longitudinal magnetization to recover is known as T1, or the recovery time constant. T2 relaxation, or spin-spin relaxation, refers to the signal decay that ensues immediately following an RF excitation pulse due energy exchange between neighboring nuclei causing individual spins to dephase. The decay time constant, known as T2, is the amount of time it takes for only 37% of the original signal (M_0) to remain in the transverse plane. The transverse signal decay that is actually measured, however, is often due to both spin-spin interactions and inhomogeneities of the static magnetic field, which causes the transverse magnetization to diminish even faster unless the sequence is capable of refocusing them. The time constant that describes this effect is referred to as T2*. Figure 2.2 depicts example T1 and T2 relaxation curves for two tissues. Since each tissue has its unique T1 and T2 relaxation rates, sequence timing parameters such as the

UNST LIBRARY

repetition time (TR) between excitation pulses and time to form an echo (TE) can be manipulated to generate the desired image contrast.

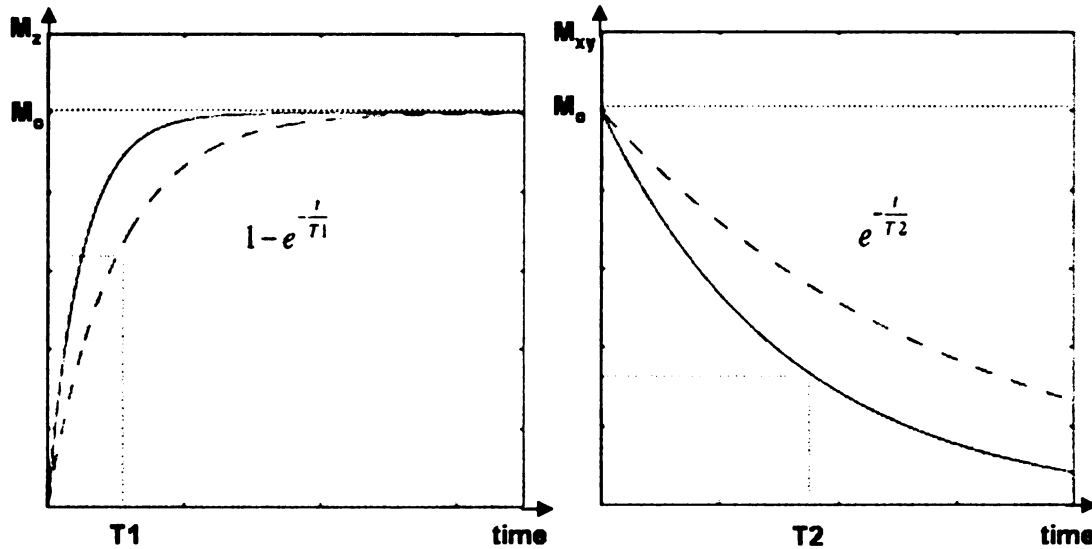


Figure 2.2: T1 relaxation (left) and T2 relaxation (right) curves for two tissues

The strength of the signal received is dependent upon the density of the spin population (ρ), and the rates of T1 and T2 relaxation according to Equation 2.1.

$$S = \rho(x,y,z) (1 - \exp(-TR/T_1)) \exp(-TE/T_2) \quad (2.1)$$

The TR controls the amount of T1 weighting, while changing the TE varies the amount of T2 (or T2*) weighting. Selecting a short TR would therefore accentuate the differences in signal intensity. However, to obtain a purely T1-weighted image, T2-weighting must be minimized to not interfere with the desired contrast, thus requiring a short TE. Thus, on a T1 weighted image, tissues with a shorter T1 that recover faster (ie. fat) appear brighter than those that take longer to recover (ie. water). Similarly, a T2 or T2* weighted image would necessitate a long TE to accentuate the differences in signal intensity due to T2 decay and a long TR to diminish the effects of T1-weighting. As a result, in T2-weighted images, materials with long T2 values are bright, while rapidly dephasing compounds lose their signal

UST LIBRARY
 1001 LIBRARY

and appear dark. In the third type of image weighting, contrast depends on the spin density, ρ . Thus, the effects of both T1 and T2 weighting must be minimized by using a short TE and long TR. These effects of image weighting are summarized in Table 2.1, and illustrated in Figure 2.3.

Table 2.1: Effects of acquisition parameters on image contrast

Image Weighting	Accentuated relaxation	Diminished relaxation	TE values	TR values
<i>T1-weighted</i>	T1	T2	short	short
<i>T2-weighted</i>	T2	T1	long	long
<i>PD-weighted</i>	none	T1 and T2	short	long

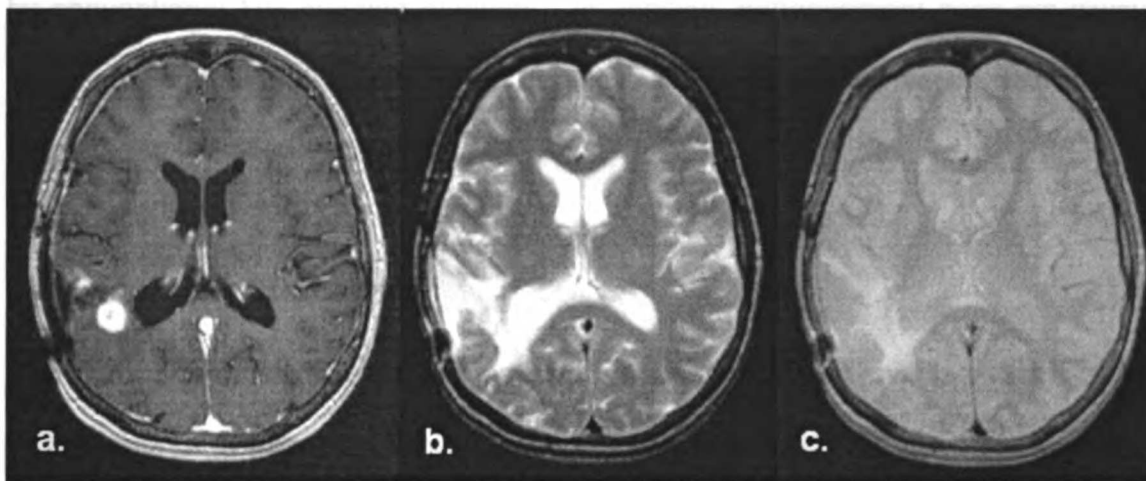


Figure 2.3: a) T1-weighted image post-gadolinium, b) T2-weighted image, and c) PD-weighted images of a high-grade glioma

A typical brain tumor MRI exam consists of T2-weighted and T1-weighted images. In general, tumors tend to elongate both T1 and T2 relaxation times and appear hypointense on T1-weighted images and hyperintense on T2-weighted images compared to the surrounding brain parenchyma. Gadolinium is administered to provide additional contrast (termed contrast enhancement), due to its ability to shorten both T1 and T2* relaxation times, and specify regions where the BBB has been compromised. Presence of contrast enhancement on T1-weighted images reflects abnormal vasculature with disruption of the BBB and is usually indicative of a

UCSF LIBRARY

higher grade tumor. Figure 2.3 shows representative T1-weighted spoiled gradient echo (SPGR), T2-weighted spin echo, and PD-weighted images of a high-grade glioma.

Although they provide useful information, these conventional MRI techniques are not always able to fully characterize differences in tumor types, disease progression, and effectiveness of therapy, and the interpretation of the data is highly subjective. Within both the enhancing and T2-weighted lesion there is heterogeneity and microscopic infiltrative tumor may spread beyond the region of abnormality defined by conventional MR imaging methods. In addition, enhancement does not always represent active tumor and often denotes areas of inflammation, necrosis, or response to radiation treatment.

2.4 Treatment Strategies

Histological classification and patient age are known prognostic indicators that dictate course of therapy. Typical survival rates range from 5-7 years for a grade II glioma, 2-4 years for a grade III glioma, and only 1 year for glioblastoma multiforme (1). Location of the tumor as well as extent of resection also influences survival. Standard treatment protocols begin with surgery (stereotactic biopsy, subtotal resection, or total resection), both to reduce the heavy mass effect and provide an accurate histological diagnosis. An exception is made for tumors in the basal ganglia, thalamus, and brain stem, which cannot be resected without vastly damaging quality of life. Unfortunately, it is rare that surgical treatment alone can remove the entire active lesion due to the infiltrative nature of these tumors, their diffuse boundaries, and the great importance of sparing normal brain function. As a

U.S.F. LIBRARY

result, patients usually receive adjuvant chemotherapy and radiotherapy, to help impede growth of residual tumor cells. Conventional radiotherapy consists of fractionated external beam radiation (xRT) given in small doses over the course of a month. Gamma knife surgery is another viable therapeutic technique where a boost of a single, high dose of radiation is administered to a locally confined target, usually in regions of recurrence. Novel treatment strategies are a topic of ongoing research and include the development anti-angiogenic agents that target the vascular supply to active lesions, immunotherapy, and gene therapy.

11/21/2011 10:21:11 AM

Chapter 3: Characterization of Spatial Heterogeneity in High-Grade Gliomas Using Dynamic Susceptibility-Contrast Perfusion Imaging

Perfusion-weighted imaging is capable of assessing functional characteristics of cerebral vasculature. This chapter investigates MR imaging parameters corresponding to the peak height and percent recovery of the T2 relaxivity curve to characterize angiogenesis and microvascular leakage within the T2-hyperintense and contrast-enhancing abnormalities in high-grade gliomas.*

3.1 Perfusion-Weighted Imaging of Brain Tumors

Basic Principles of Tracer Kinetics

Perfusion evaluates the amount of blood delivered to the capillary bed of a block of tissue in a certain period of time and is related to the amount of oxygen and other nutrients in the tissue. MRI techniques that can aid in characterizing tissue perfusion fall into two main categories: 1) endogenous methods that directly follow labeled blood such as arterial spin labeling and can be employed to measure cerebral blood flow, and 2) exogenous methods that involve the injection of an intravascular contrast agent to measure blood volume and permeability. In this work we focus on exogenous methods, whose theory is based on compartmental modeling of tracer kinetics, in order to characterize blood vessel volume and permeability within high-grade brain tumors.

The theory behind tracer kinetics was originally described by Tofts and Kermode (21) and is represented in Figure 3.1. General assumptions include a short (bolus)

USF
LIBRARY

implemented on a fast enough time scale to directly measure the first passage of a contrast agent bolus, and the compartmental modeling used requires several assumptions and extrapolation to infer blood volume measurements. Dual echo techniques allow for quantification of various parameters by accounting for T1-effects of the contrast agent in the interstitial tissue by taking the ratio of the signal at two different echo times (27-30), but have limited coverage, and hence prevent the characterization of spatial variations in the microvasculature of heterogeneous tumors.

T2*-weighted methods are another way in which to track the perfusion of a contrast medium. These techniques are best for blood volume estimates since they are capable of attaining a high enough time resolution to capture the first pass bolus, but mandate correction for tracer recirculation and vascular leakage as they can only assess the fast leakage component (<2min). Figure 3.2 is a simplified, bi-compartmental model for Figure 3.1 with the following added assumptions: 1) fast mixing of bolus within the plasma, 2) flow in only one direction, 3) leakage is due only to permeability and not blood flow in the capillaries. The total concentration of tracer measured within a voxel at any given point in time is thus the sum of the plasma concentration (C_p) and any concentration of tracer that leaked out of the blood vessel into the extra-cellular, extra-vascular space (C_e), each weighted by the volume fraction (v) of the of the space occupied within a voxel (Equation 3.1).

$$C(t) = v_e C_e(t) + v_p C_p(t) \quad (3.1)$$

The rate of change in contrast agent that enters the leakage space is based on pharmacokinetic theory and is therefore equal to the difference in tracer

concentration between the two compartments multiplied by the permeability transfer constant, K^{trans} (Equation 3.2).

$$\frac{dC_e(t)}{dt} = K^{trans} \frac{(C_p(t) - C_e(t))}{v_e} \quad (3.2)$$

Solving equation 3.2 yields an expression for the concentration of contrast agent in the extra-cellular, extra-vascular space (Equation 3.3).

$$C_e(t) = \frac{K^{trans}}{v_e} \int (C_p - C_e) dt \quad (3.3)$$

Substitution of this equation back into Equation 3.1 results in a formula for total contrast agent concentration expressed as a sum of the concentration within the plasma plus the amount that has leaked out into the extracellular extravascular space (Equation 3.4).

$$C(t) = v_p C_p(t) + K^{trans} \int (C_p - C_e) dt \quad (3.4)$$

Since T2*-based methods use the change in T2* relaxivity ($\Delta R2^*$) due to a paramagnetic contrast agent as a function of time, as a relative measure of concentration, the measured $\Delta R2^*$ signal can then be modeled as a linear combination of T2*-weighted and T1- plus permeability-weighted components.

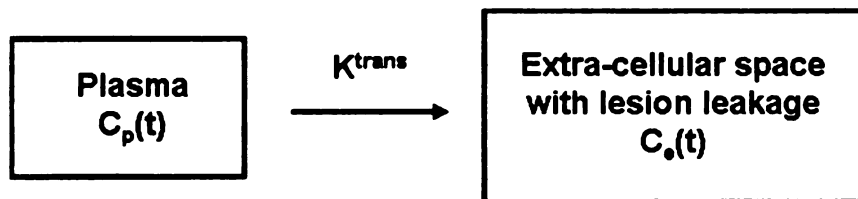


Figure 3.2: Bi-compartmental model of tracer distribution for T2* methods

Dynamic Susceptibility-Contrast Perfusion and Echo Planar Imaging

Dynamic susceptibility-contrast (DSC) MRI is a technique that is commonly used to estimate relative cerebral blood volume (rCBV) through examination of the degradation of signal intensity over time associated with a bolus of a paramagnetic contrast agent such as gadolinium DTPA (4,31-38). Magnetic susceptibility is a term used to describe a material's ability to become magnetized by the applied magnetic field. Paramagnetic compounds are easily magnetized and therefore have a magnetic susceptibility larger than one. DSC MRI exploits the fact that changes in the local magnetic susceptibility, can manipulate image contrast. The magnetization (M) experienced by the tissue, is a product of the external field (B_0) and the magnetic susceptibility constant (χ) as shown in Equation 3.5.

$$M = \chi B_0 \quad (3.5)$$

The administration of a paramagnetic contrast agent (a material with a magnetic susceptibility greater than zero) increases the effective magnetic field (B_{eff}) felt by the tissue surrounding the bolus as indicated by Equation 3.6,

$$B_{\text{eff}} = B_0(1 + \chi) \quad (3.6)$$

which in turn accelerates spin-spin dephasing and signal decay, shortening $T2^*$. During the first pass of the contrast agent bolus, the measured signal intensity in that region decreases on $T2^*$ -weighted images and then recovers as the agent recirculates. The $T2^*$ signal intensity time series is converted to the change in relaxation rate or $T2^*$ relaxivity curve ($\Delta R2^*$) according to Equation 3.7.

$$\Delta R2^*(t) = \ln[S_0/S(t)]/TE \quad (3.7)$$

which is proportional to concentration at the doses typically used for patient studies (4,5,32,34,35,37,39-43). Figure 3.3 demonstrates representative $T2^*$ signal-time

intensity curves characteristic of normal-appearing white matter, normal-appearing gray matter, and tumor tissue. The change in signal intensity on these curves is 2-3 times greater for gray matter than white matter due to the increased number and size of vessels in this region. High-grade, vascular tumors can exhibit upwards of three times the drop in signal intensity compared to normal white matter which often does not recover to baseline levels during the recirculation phase due to the presence of tortuous or leaky vessels.

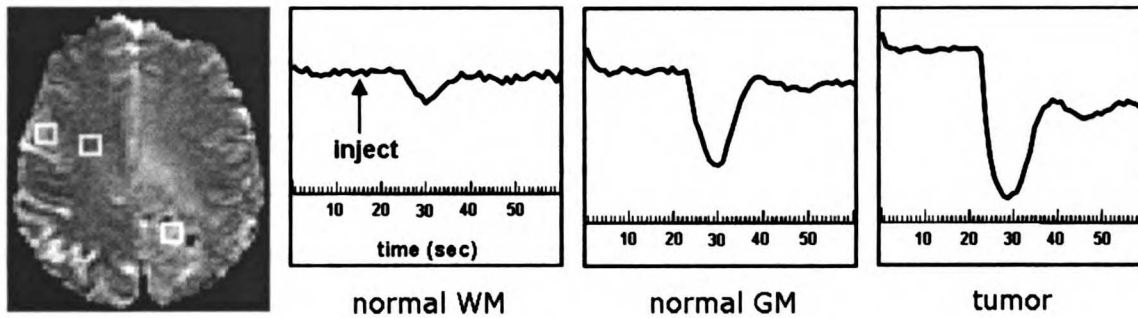


Figure 3.3: Normal and abnormal T2* signal-time intensity curves for different brain regions

DSC MRI requires a fast imaging sequence in order to capture the local susceptibility fluctuations as the bolus passes through the vessels and can be easily implemented clinically where both short scan times and robust results are important factors in order for the data to be immediately incorporated into patient management. The most common rapid imaging technique utilized for this application is echo planar imaging (EPI). In contrast to conventional acquisition schemes that sample only one line of k-space every TR, EPI employs the use of fast, steep gradients to quickly traverse all of k-space within one excitation. Figure 3.4 illustrates the timing diagram for a single shot, gradient echo EPI pulse sequence and corresponding k-space trajectory. With this sampling scheme, rapidly alternating frequency encode

USF
 LIBRARY

gradients produce multiple echoes and allow for the collection of an entire three-dimensional dataset every second. There are, however, several limitations to EPI which will be discussed in detail in Chapter five.

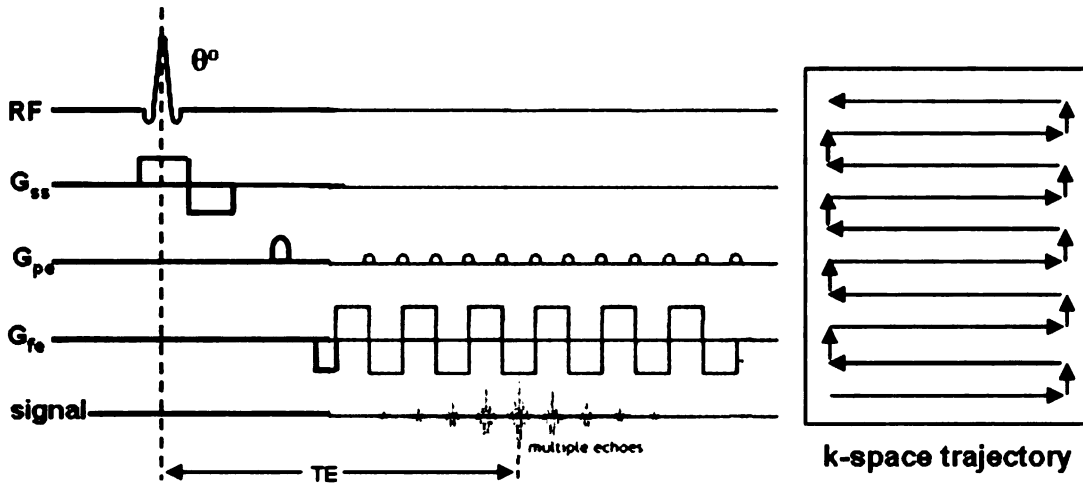


Figure 3.4: Single-shot gradient echo EPI pulse sequence and corresponding k-space trajectory

The two most commonly used pulse sequences in MRI are gradient echo (GRE) and spin echo (SE). The difference between these two pulse designs lies in the way in which they form an echo. As shown in Figure 3.5, a spin echo sequence utilizes an 180° radiofrequency pulse to generate the echo for signal reception, while a gradient echo sequence relies on changing the polarity of the frequency encode gradient for echo formation and usually employs a smaller flip angle pulse for excitation. As a result, faster imaging with reduced T2 decay is inherently possible with GRE sequences. Spin echo sequences, however, have the added benefit of higher SNR since the 180° pulse refocuses dephased spins due to static field inhomogeneities. Thus, SE sequences are usually utilized for T2-weighted images

which necessitate a long TE and TR, while GRE sequences are widely used for T1-weighted imaging where short TE and TR intervals are required.

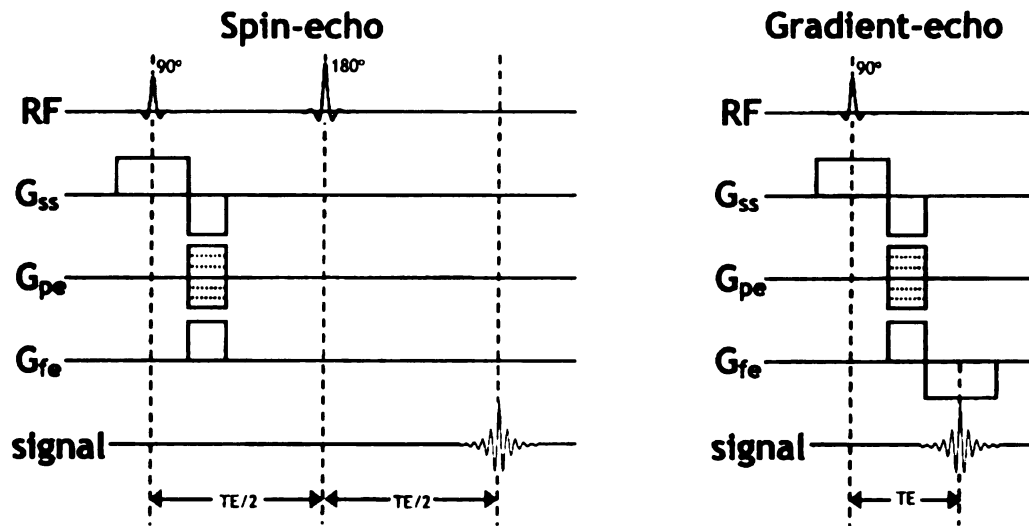


Figure 3.5: Diagram of spin echo and gradient echo pulse sequences

The characteristic signal loss in DSC MRI is due to the susceptibility-induced shortening of T2* by the contrast agent through spin dephasing. Both GRE and SE EPI pulse sequences can be made sensitive to these changes in T2*, with GRE images depicting a greater effective change in signal intensity. The leakage of contrast agent into the extra-vascular space due to BBB breakdown leads to additional changes in signal intensity on echo planar images. The first effect is an increase in intensity based upon the reduction in T1 of the tissue and the second effect is a decrease in intensity due to increased susceptibility-induced T2* shortening. As exhibited in Figure 3.6, for the T1-effects of the leaking contrast agent dominate on SE EPI images and cause an over-shoot in signal intensity beyond the baseline levels. The signal weighting observed in GRE images results from susceptibility-induced T2* shortening of the leaking contrast agent opposing

increases in signal from T1-effects, which is highly dependent on the flip angle. In this work, a small flip angle (35°) was selected in order to provide sensitivity to variations in signal changes due to contrast agent leakage during the recirculation phase so that T2* shortening predominates and prevents the return to baseline signal levels as shown in Figure 3.6.

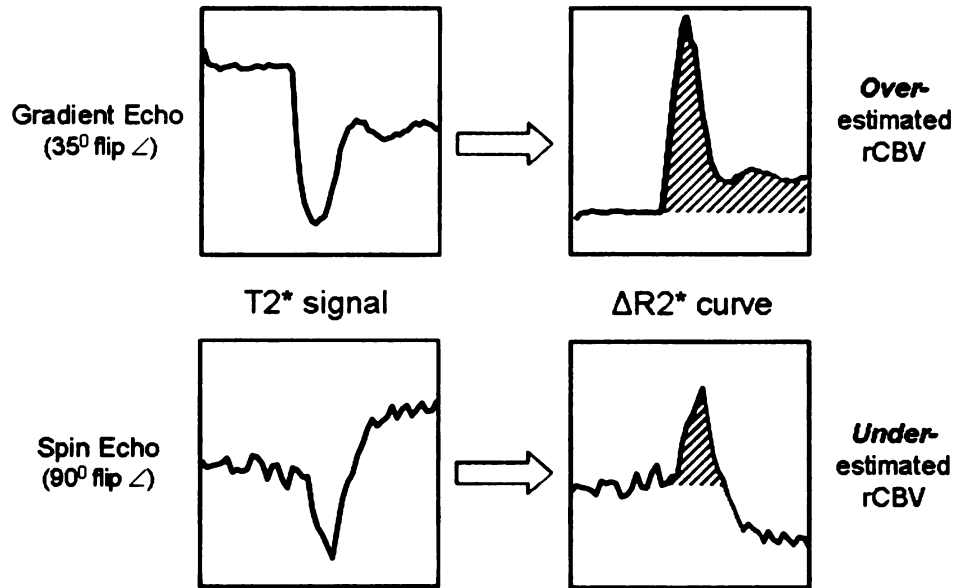


Figure 3.6: Effects of sequence and flip angle selection on rCBV estimation

Cerebral Blood Volume Calculation

Traditional calculations from the dynamic data attempt to estimate the elevated blood volume in a given region relative to normal white matter by taking the area under the concentration vs. time curve (44). The estimation of rCBV using this method relies on the assumption of an intact BBB, which is typically not true for most high-grade gliomas. Numerous studies have attempted to correct for the under or over estimation of rCBV measurements from dynamic susceptibility-weighted perfusion MRI in regions of microvascular leakage and to derive new parameters to more accurately characterize endothelial permeability (4,5,35,36,38,41-43). These

include methods that can distinguish the boundary between the first pass bolus and recirculation, such as baseline subtraction, which attempts to remove a change in baseline by shifting the slope and endpoints of integration(4), or using a non-linear algorithm to fit a gamma variate function, to help eliminate the effects of leakage into the extravascular space (4,34,35). Non-linear fitting procedures are typically unstable in portions of the image that have low signal to noise ratio. More robust attempts to separate rCBV and relative permeability involve generating a model function of the signal as a sum of two components corresponding to the opposing T1 and T2* effects and then implementing a linear fitting method to estimate the properties of each component (5,36,38,45). Other approaches have examined changes in the recirculation phase of bolus tracking using a relative recirculation (rR) parameter as a measure of vascular tortuosity and leakage. Estimates of rR correlate with tumor grade and have been utilized in assessing response to therapy (37,41-43). With all these techniques it is difficult to distinguish the boundary between the first pass bolus and recirculation.

Various groups have compared rCBV and/or permeability in low and high-grade brain tumors. In the majority of these studies, the values used in the analysis have been obtained by a radiologist manually defining three or four regions of interests (ROIs) of $\sim 60 \text{ mm}^3$ in the center of the tumor from the post-contrast T1-weighted imaging and then finding the region with the maximum rCBV or permeability compared to the contralateral white matter (4,32,34,35,45-48). It has also been shown previously that the point of maximum signal drop (MSD) on the T2* signal time curve is correlated with rCBV values and is a more stable measure of vessel volume in brain tumors (40). The purpose of this study is to investigate values obtained on a voxel by voxel basis using a non-parametric model corresponding to

the peak height and percent recovery of the T2* relaxivity curve, in order to characterize heterogeneity in patterns of angiogenesis and microvascular leakage in regions of T2 abnormality and contrast enhancement for patients with high-grade gliomas.

3.2 Methods

Patients

MR imaging was performed on 41 untreated brain tumor patients (20 female, 21 male) immediately prior to surgery. Histopathologic analysis of the resected tissue confirmed the diagnosis of 18 grade III gliomas (median age 47) and 23 grade IV gliomas (median age 54), as classified by the WHO II criteria.

MRI Acquisition

MRI exams were performed on a 1.5 T Signa Echospeed scanner (GE Medical Systems, Milwaukee, WI). The MR imaging protocol consisted of a three-plane localizer (8.5/1.6 ms [TR/TE]), axial fluid-attenuated inversion recovery (FLAIR; 10,000/148/2200 ms [TR/TE/TI]), axial 3D fast spin-echo T2-weighted imaging (FSE; 3000/102 ms), dynamic susceptibility-weighted, gradient-echo, echo planar imaging (EPI; 1000-1250/54 ms, flip angle 35°), and post-contrast 3D spoiled gradient-recalled (SPGR; 34/8 ms) T1-weighted imaging. The T2-FLAIR, FSE, and post contrast T1-SPGR images were acquired and used to define regions of T2 hyperintensity and T1 enhancement.

For the dynamic EPI series, the location and size of the tumor and the position of the superior and inferior margins were determined from the T2-weighted FLAIR or

FSE images. Seven or eight slices were selected to cover the majority of the tumor volume. Slice thickness ranged from 3 to 5 mm and slice gap 0 to 2 mm. A standard dose of 0.1 mmol/kg body weight of gadopentetate dimeglumine (Gd DTPA) was injected intravenously with an MR-compatible power injector at a rate of 5 ml/s, followed immediately by a 20-ml continuous saline flush. A series of T2*-weighted multi-slice image sets (with a $26 \times 26 \text{ cm}^2$ in plane FOV and 128×128 acquisition matrix) were acquired every 1-1.25 seconds during the first pass of the contrast agent until 60 time points were obtained.

Image Processing

The FLAIR/FSE, post-contrast 3D SPGR, and raw T2*-weighted echo planar images were transferred to a UNIX workstation (Sun Microsystems, Mountain View, CA) for off-line post-processing. Image analysis was performed by using in-house software written in C and IDL programming languages (Research Systems, Inc., Boulder, CO). The FLAIR/FSE and post-contrast 3D SPGR images were resampled to the same slice locations and resolution as the echo planar perfusion images. The dynamic dataset was aligned to the anatomical images using affine and perspective transformations and, where necessary, non-rigid B-spline warping (49) by maximization of normalized mutual information (50). The co-registered perfusion series was then resampled to a 32×32 grid in-plane with a $16 \times 16 \text{ cm}^2$ field of view so that the observed signal changes had sufficient signal to noise ratio to be analyzed reliably on a voxel by voxel basis. The pixel size was increased to a $5 \times 5 \text{ mm}^2$ resolution in order to ensure that errors in the alignment to anatomical images due to geometric distortion would be contained within one voxel. This oversampling

was comparable to most other studies that draw several ROIs (4,31,35,45,46,48), each encompassing approximately twenty $2 \times 2 \text{ mm}^2$ voxels, in order to obtain several rCBV or permeability measurements in the same region from which to calculate a maximum value.

For each tumor, ROIs were drawn around the contrast enhancing and T2 lesions from the resampled post-contrast injection 3D SPGR and either FLAIR or FSE images, respectively. Regions of signal dropout due to susceptibility on the echo planar images were excluded from the ROIs. The resampled echo planar image for a single slice of the first image set and corresponding T2* signal intensity time curves is displayed in Figure 3.7a, with overlaying contours depicting the extents of the T2 lesion, T2L (in green), and contrast enhancing lesion, CEL (in red).

Analysis of T2* Signal Intensity Time Curves

The T2* signal time curve acquired during the first pass of gadolinium bolus was converted to the change in relaxation rate ($\Delta R2^*$). The pre-contrast baseline signal, S_0 , was established from six image volumes acquired prior to contrast injection. Since the relative Gd-DTPA concentration is proportional to the $\Delta R2^*$ curve, a plot of the relative concentration of Gd-DTPA in tissue over time was obtained for each voxel as exhibited in Figures 3.7b-c.

Subsequent analysis of the $\Delta R2^*$ curves was performed utilizing in-house programs created with Matlab 6.5 software (MathWorks Inc., Natick, MA) as shown by Figure 3.7c-f. In order to normalize intensity differences between scans, the $\Delta R2^*$ curve was divided by the intensity value at the second peak of the image histogram obtained from the first time point of the echo planar image series. Peak

height (the distance between 2 and 1 in Figure 3.7c) and percent recovery of the post bolus signal from the maximum $\Delta R2^*$ signal (or the distance between 2 and 3 in Figure 3.7c) were determined for each voxel within the T2 and contrast enhancing (CE) lesions. Percent recovery was calculated as the difference between the peak height and average post-bolus signal divided by the peak height signal on the $\Delta R2^*$ curve.

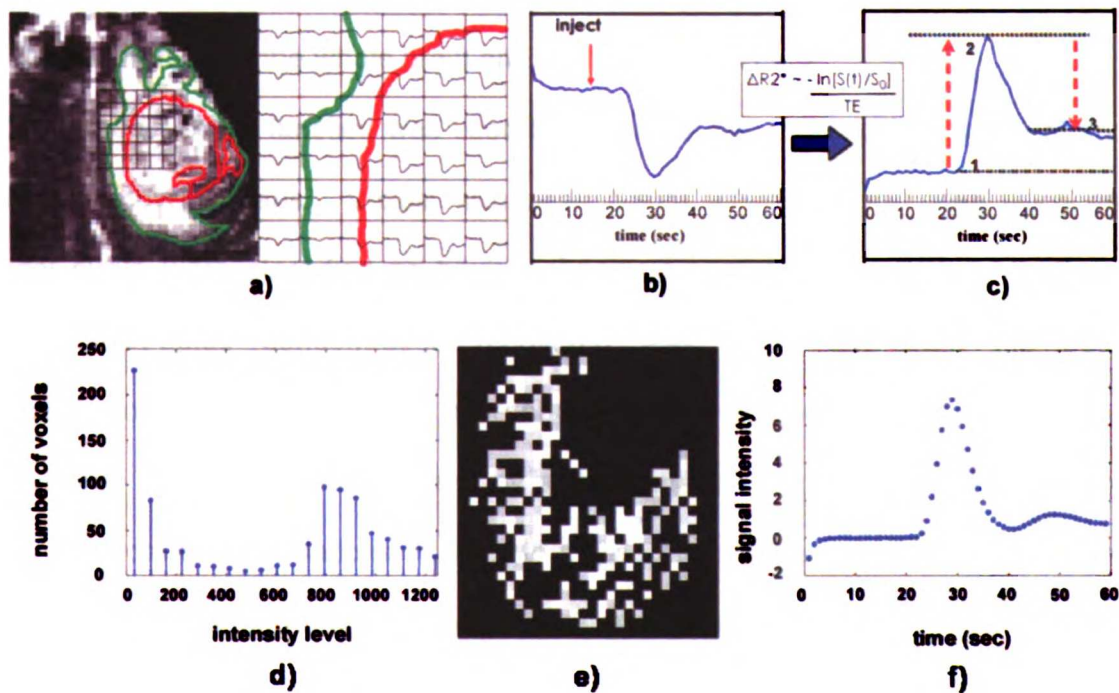


Figure 3.7: Depiction of post-processing steps for analyzing T2* signal-intensity time curves

A model curve function (Figure 3.7f) was derived from averaging the time series data derived from normal appearing brain using the following automated approach. Voxels from the first pre-contrast echo planar image volume were arranged in a histogram based on their image intensity (Figure 3.7d). A varying range of intensities, based on the maximum intensity and histogram peak was experimentally established to select the image intensities that corresponded only to normal brain

tissue (Figure 3.7e). The model function was then generated by averaging $\Delta R2^*$ curves for all voxels displayed in Figure 3.7e. This method proved to be robust and was able to successfully exclude curves within the T2 and contrast enhancing lesions, as well as ventricles, large veins, and necrotic regions. The reliability of the model function generation was assessed in several patients by comparing it to the averaged $\Delta R2^*$ curves within manually-drawn white matter ROIs. In all of the patients examined, the automated model function was within the range of curves generated from both the whole brain and white matter ROIs.

The model curve function was used to normalize and threshold peak height and percent recovery maps. Voxels with peak height values greater than twice the model curve were classified as having abnormal peak height (aPH), while those whose post-bolus concentration recovered less than 75% from the peak concentration were considered to have abnormal recovery (aRec). Regions with no signal drop (NSD), as characterized by a flat signal on the time series data, were excluded from the calculations in order to avoid spurious results. NSD voxels were defined as having both low peak height ($<.5$) and poor correlation ($r < .25$) with the model function.

Volumes of aPH, aRec, NSD, and contrast enhancement were calculated and normalized according to the T2 lesion volume within the perfusion images. Mean and maximum peak height values, as well as mean and minimum percent recovery (the lowest percent recovery value within a given region, indicating the greatest amount of BBB breakdown), were calculated within the contrast enhancing lesion (CEL), T2 lesion (T2L), and T2 lesion excluding contrast enhancement (T2L – CEL) for each patient individually and then averaged across patients within each cohort. Voxels from all patients of the same grade were then combined for each region and

mean values of parameters were computed. Statistical significance of group comparisons was determined through the use of a Wilcoxon ranked sum test. P-values less than .05 were considered significant.

3.3 Results

All patients had large regions of T2 hyperintensity that were assumed to correspond to the area at risk for increased angiogenesis. Seven of the eighteen patients with grade III lesions and all twenty-three patients with grade IV lesions exhibited enhancement on the T1-weighted post-contrast SPGR image. While the intention was to cover the entire region of T2 hyperintensity for each lesion, the limited number of slices that could be acquired for the dynamic imaging meant that this was not always possible. The spatial extent of regions with abnormal MR parameters was therefore expressed as a percentage of the portion of the T2 lesion that was covered. The percentages of this region that were enhancing on the T1-weighted post-contrast images were significantly greater for the patients with grade IV gliomas than for patients with enhancing grade III lesions. Twenty-one of the twenty-three patients with grade IV lesions also had central regions of hypointensity on the post gadolinium T1-weighted images that were interpreted as suggesting necrosis. Similarly, grade IV gliomas also showed a significantly larger volume of NSD compared to grade III patients (Table 3.1).

Table 3.1: Volumes of abnormality expressed as a percentage of the T2 lesion, for grade III and grade IV gliomas

	CEL	NSD	aPH	aRec
<i>grade III</i>	9.8 ± 12.3 %	7.6 ± 10.7 %	13.0 ± 10.0 %	10.1 ± 16.7 %
<i>grade IV</i>	32.7 ± 18.5 %	21.6 ± 22.7 %	24.9 ± 15.8 %	22.7 ± 16.9 %
<i>P - value</i>	<i>P < .01</i>	<i>P < .02</i>	<i>P < .01</i>	<i>P < .001</i>

Volumes with Abnormal Perfusion

There was considerable heterogeneity in the dynamic concentration curves and the abnormal recovery within a grade III and grade IV glioma as showed in Figure 3.8. The grade IV glioma in this example demonstrates a large area of aPH (green) and aRec (magenta) near the center of the lesion while in the grade III glioma both aPH and aRec are more peripherally located. The volumes of aPH and aRec were significantly greater for grade IV than grade III gliomas (Table 3.1).

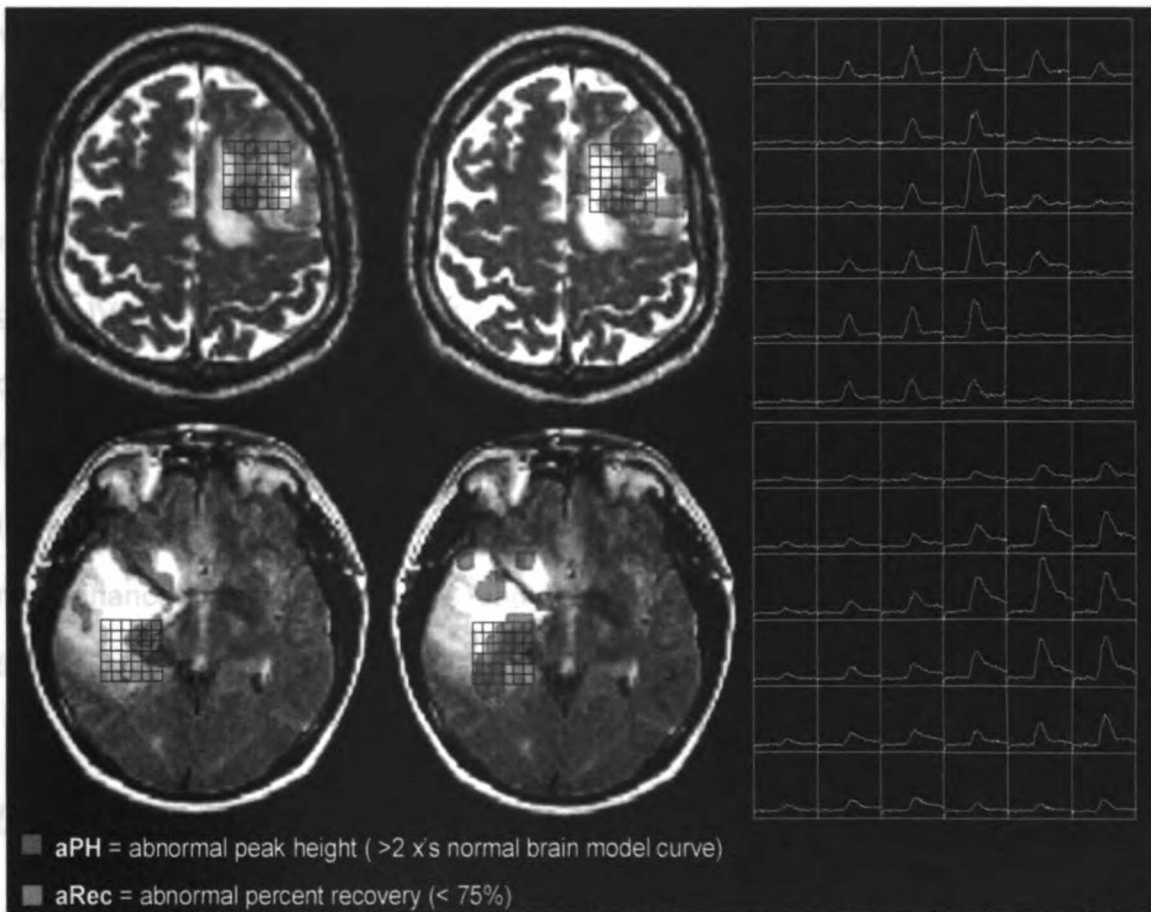


Figure 3.8: Example of abnormal peak height (aPH; left) and abnormal recovery (aRec; center) maps for grade IV (top) and grade III (bottom) gliomas overlaid on a T2-weighted image (top – FSE, bottom – FLAIR) and the $\Delta R2^*$ curves from which they were derived (right).

Peak Height

Grade IV gliomas exhibited significantly higher mean and maximum relative peak height values within the CEL than enhancing grade III patients (Table 3.2). This was mainly due to the significantly elevated maximum peak height values (5.7, $P < .01$) outside the CEL for the grade III cohort. Mean peak height values, however, were similar for both regions of grade III tumors (1.2 for the CEL and 1.1 for the T2L-CEL). Grade IV patients exhibited elevated mean peak height values within the CEL compared to the T2L-CEL (2.0 vs. 1.2, $P < .001$), but the maximum peak height values were comparable (6.0 vs. 5.8). There was no significant difference in mean or maximum peak height values between grade III and grade IV populations in the T2L-CEL region. Analysis of all voxels combined across patients within a given region did show a significant increase in mean peak height in the T2L-CEL region for grade IV patients (see Table 3.4). Although the maximum peak height value lay outside the region of enhancement for all enhancing grade III patients, 61% of grade IV patients showed maximum peak height within the CEL. Table 3.5 shows that there was no significant difference in relative peak height values between the T2L of non-enhancing grade III gliomas and the T2L surrounding the CEL in grade IV tumors.

Percent Recovery

As expected, there was no significant difference in the recovery of the model function between grades ($P > .8$), with grade III = 82.5 ± 4.9 % and grade IV = 83.1 ± 4.0 %, since it is derived by averaging normal voxels. Decreasing trends were observed with higher grade for both the minimum and mean percent recovery values

in all regions (Table 3.3). However, this reduction was only significant ($P < .01$) for minimum recovery values within the CEL. Within the grade III cohort there was a significantly lower minimum recovery of 56.1% in the T2L surrounding the area of enhancement ($P < .03$), compared to 71.1% recovery within the CEL. When comparing all voxels in a specified region grouped together across patients, all of the observed trends for mean recovery values become significant, with voxels of grade IV gliomas having a lower mean recovery than grade III voxels and CEL voxels having a lower mean percent recovery than T2L–CEL voxels for each grade (Table 3.4). The minimum recovery value was outside the CEL for all enhancing grade III patients, but minimum recovery was within the CEL for 22% of the patients with grade IV lesions. Patients with non-enhancing grade III gliomas had significantly higher minimum recovery than the T2L – CEL region in grade IV patients (58.8% vs. 43.3% with $P < .03$, Table 3.5).

Table 3.2: Relative peak height values within the CEL and T2–CEL for grade III and grade IV gliomas

Tumor Grade	Relative Peak Height			
	CEL	T2L – CEL		
	mean	max	mean	max
<i>grade III</i>	1.2 ± 0.8	2.3 ± 1.6	1.1 ± 0.4	5.7 ± 2.7
<i>grade IV</i>	2.0 ± 0.9	6.0 ± 3.2	1.2 ± 0.5	5.8 ± 2.6
<i>P- value</i>	$P < .05$	$P < .002$	$P = 1$	$P > 0.5$

Table 3.3: Percent recovery values within the CEL and T2–CEL for grade III and grade IV gliomas

Tumor Grade	Percent Recovery			
	CEL	T2L – CEL		
	mean	max	mean	max
<i>grade III</i>	80.4 ± 11%	71.1 ± 13%	83.7 ± 6.2%	56.1 ± 14.6%
<i>grade IV</i>	77.5 ± 6.7%	47.7 ± 18%	82.2 ± 4.7%	43.3 ± 18.5%
<i>P- value</i>	$P < .01$	$P > 0.1$	$P > 0.1$	$P > 0.5$

Table 3.4: Relative mean peak height and percent recovery values for all voxels within the CEL and T2–CEL combined across grade III and grade IV patients

Tumor Grade	Relative Peak Height		Percent Recovery	
	CEL	T2L – CEL	CEL	T2L – CEL
<i>grade III</i>	1.1 ± 0.9	1.0 ± 0.9	82.5 ± 10.5 %	84.9 ± 8.8 %
<i>grade IV</i>	2.1 ± 1.6	1.2 ± 1.0	76.4 ± 11.8 %	80.9 ± 10.6 %
<i>P- value</i>	<i>P < .001</i>	<i>P > 0.1</i>	<i>P < .001</i>	<i>P < .01</i>

Table 3.5: Relative peak height and percent recovery values for the T2L of non-enhancing grade III patients compared to the T2–CEL of grade IV patients

Tumor Description	Relative Peak Height		Percent Recovery	
	mean	max	mean	min
<i>T2L, NE grade III</i>	1.2 ± 0.4	5.7 ± 2.8	86.4 ± 3.4 %	58.8 ± 12%
<i>T2L – CEL grade IV</i>	1.2 ± .5	5.8 ± 2.6	82.2 ± 4.9 %	43.3 ± 18.5 %

NE = non-enhancing

3.4 Discussion and Conclusions

The degree of angiogenesis and microvascular leakage are important physiological parameters that can provide insight to the malignant potential of tumors. Dynamic susceptibility-weighted perfusion MRI is able to provide maps of peak height and percent recovery that contain information about these physiological processes. A noteworthy feature of this approach is that it is a fast method in which the calculations do not rely on any prior assumptions as to the biology of the model that they describe. By investigating the two parameters peak height and percent recovery independently, confounding corrections of rCBV and K^{trans} , as well as other permeability measures, can be removed while separating first-pass bolus characteristics from the recirculation phase. Our analysis of data from patients with grade III and grade IV gliomas has shown that there is spatial heterogeneity in these parameters for both the region of contrast enhancement (CEL) and the surrounding region of hyperintensity on T2-weighted images (T2L-CEL). Our goal was to gain insight as to how different regions of each tumor type behave, in addition to

differentiating between the two astrocytic tumor grades. While the presence of such heterogeneity is not surprising based upon the known histological characteristics of these tumors, the fact that it can be measured non-invasively is novel and likely to be important for the clinical management of individual patients. Identifying certain regions of a grade III tumor that have similar vascular features to a grade IV tumor would be useful in determining the more aggressive part of the tumor for planning therapy. This heterogeneity, however, also underlines the potential limitations in describing the characteristics of the tumor from measurements made by considering small regions of interest or by averaging values across the entire T2L.

The choice of metrics used to describe the shape of the dynamic data was dictated by our desire to minimize the dependence on complex, non-linear fitting procedures and to provide robust estimates of meaningful parameters. The calculations of peak height and percentage recovery are simple to implement and are relatively insensitive to signal to noise ratio. Although there was some variation in observed peak widths, the time to peak was remarkably similar (within one time point) for both the normal and tumor voxels. This suggested that there was a close correspondence between the peak heights and the underlying rCBV. The observation of abnormal recovery in the T2L-CEL suggests that this parameter may be more sensitive to the presence of abnormal vasculature than conventional post-contrast images. Whether this is due to increased vessel tortuosity or to a more reliable measure of vascular permeability is yet to be determined.

The measurement of rCBV in tumors is complicated in regions where the blood-brain-barrier is compromised. The leakage of contrast agent into the extra-vascular space leads to additional changes in signal intensity on the echo planar images. The first effect is an increase in intensity based upon the reduction in T1 of the tissue and

the second effect is a decrease in intensity due to increased susceptibility-induced T2* shortening. We chose gradient echo, EPI with a low flip angle (35°), so that the susceptibility-induced T2* shortening of the leaking contrast agent predominates, preventing an overshoot of the baseline signal. As a result, the recovery of the model function for normal tissue ranged from 77% to 90% across all patients (with the exception of one outlier), regardless of tumor grade, and recovery values of less than 75% were considered abnormal. A cutoff of twice the model peak height was selected to define what was considered abnormal peak height or vessel volume, since it has been shown that the blood volume of gray matter, and subsequently the peak height of the $\Delta R2^*$ curve, is two to three times that of white matter (4,40). The peak height of the model function would therefore be approximately 1.5 times that of normal white matter tissue, since the model function is derived from voxels comprising both white matter and the portion of gray matter excluding large vessels. Thus, a threshold of twice the model function height should be a reliable indicator of abnormal blood volume.

The volume of contrast enhancement on post-gadolinium T1-weighted images has been previously shown to increase with tumor grade (51). This was confirmed by the results of our study. Besides signifying a disruption of vascular integrity, the presence of contrast enhancement can indicate either active tumor or macroscopic necrosis. The observed increase in NSD volume with glioma grade was expected since regions of NSD are devoid of vasculature and are likely to coincide with necrotic regions, the presence of which is indicative of grade IV tumor. The significantly larger volumes of aPH and aRec for grade IV gliomas support the idea that there is a global increase in angiogenesis and BBB breakdown in the microvasculature of grade IV gliomas.

Both grade III and grade IV patients exhibited abnormal vessel volume outside the CEL, as indicated by elevated peak height values (Tables 3.2 and 3.4). That the maximum peak height values were lower within the CEL for enhancing grade III gliomas, suggests that there is increased angiogenesis in portions of tumor outside the CEL. This interpretation is consistent with elevated blood volume preceding the appearance of enhancement (52). In grade IV patients, it appears that increased vessel volume is more likely to be localized to the enhancing region based on the mean peak height values. The presence of contrast enhancement in grade IV patients represents a combination of tumor plus necrotic tissue, rather than reflecting BBB breakdown due to tumor alone. The elevated mean peak height values exhibited by grade IV patients and the fact that this increase was localized to the enhancing region can be attributed to the local hypoxia and is a known promoter of angiogenesis (16-19,53,54). The two patient populations had similar peak height values within the edema that surrounds the enhancing tumor. Comparison of voxels across all patients did reveal a significant difference in mean peak height (.1), even though relative peak height values between the T2L of non-enhancing grade III gliomas and the T2L surrounding the CEL in grade IV tumors were similar, as shown in Table 3.5. Comparable elevated peak heights were found in the surrounding T2 lesion of grade III gliomas as in the same region in grade IV gliomas even though these same grade III patients exhibit significantly reduced peak height within the CEL.

As expected, we observed reduced mean percent recovery values in regions of contrast enhancing tumor for both patient populations. The lower mean percent recovery values observed in patients with grade IV gliomas was consistent with the elevated CEL volume observed in these patients (Table 3.1). The decline in

recovery within the CEL can be interpreted as indicating damage to the microvasculature, which leads to leakage of contrast agent into the extravascular space. However, our results also showed an unexpected decrease in minimum recovery in the surrounding T2L for the grade III patient population (Tables 3.3 and 3.4). Minimum recovery refers to the lowest percent recovery value within a given region, indicating the greatest amount of BBB breakdown. Incomplete recovery in the non-enhancing region suggests that either the post-contrast T1-weighted imaging is not sensitive enough to detect all the damaged vessels or that the vessels are extremely tortuous. Patients with non-enhancing grade III gliomas showed a similar recovery pattern to that of the T2L – CEL region of the grade IV population (Table 3.5), further substantiating the differences observed above and the fact that the presence of enhancement may not always reflect the most malignant portion of the tumor.

Abnormalities within the recirculation phase of the contrast agent bolus are often difficult to characterize and accurately interpret with respect to the underlying physiology. Kassner and Jackson et al. have previously described the implementation of a relative recirculation parameter (rR) as a way to characterize changes in the recirculation phase due to the presence of tortuous vessels that form in response to incomplete angiogenic processes (37,43). According to this group, tortuosity manifests as both an increase in blood vessel volume, which is reflected by elevated rCBV (or in our case aPH), and decreased signal recovery in the recirculation phase, as denoted by larger rR values (or reduced percent recovery). The additional presence of contrast enhancement would then suggest increased BBB breakdown in these tortuous vessels. If there is a concomitant increase in vessel volume, the reduction in recovery in non-enhancing tumor suggests the

presence of tortuous but intact vessels. Similarly, the presence of contrast enhancement in patients with grade III gliomas is probably due to breakdown of the BBB, while grade IV glioma patients are probably also experiencing a combination of angiogenesis and/or greater vascular tortuosity within the enhancing region.

Tumor microvasculature characteristics and their spatial distributions have shown considerable heterogeneity in grade III and grade IV glioma patients. Direct measurement of curve-shape parameters such as peak height and percent recovery has clearly improved specificity in characterizing these vascular changes in high-grade gliomas compared to traditional rCBV calculations.

Chapter 4: Analysis of Metabolic Indices in Regions of Abnormal Perfusion in High-Grade Glioma Patients

The previous chapter introduced dynamic susceptibility contrast MRI for perfusion imaging of high-grade gliomas and showed that voxel by voxel comparison of values obtained from a non-parametric model can be employed to characterize regions of abnormal vasculature. This chapter combines lactate-edited 3D MRSI with DSC-MRI to probe tumor oxygenation and gain insight as to how different regions of each tumor type behave.

4.1 3D ^1H Magnetic Resonance Spectroscopic Imaging

Magnetic Resonance Spectroscopy and Detectable Metabolites

Magnetic resonance spectroscopy (MRS) is a non-invasive, functional imaging technique that can provide insight to the biochemical status and metabolic activity of tissue. It emerges from the fact that proton spins within varying chemical environments experience different chemical shielding. This results in variations in precession frequency that are known as chemical shift. At a long echo time of 144 ms, the peaks of five metabolic compounds can be identified in brain tissue: choline (Cho), creatine (Cre), N-acetyl aspartate (NAA), lactate (Lac), and lipid (Lip). Figure 4.1 illustrates example spectra from normal brain tissue, tumor, and necrosis.

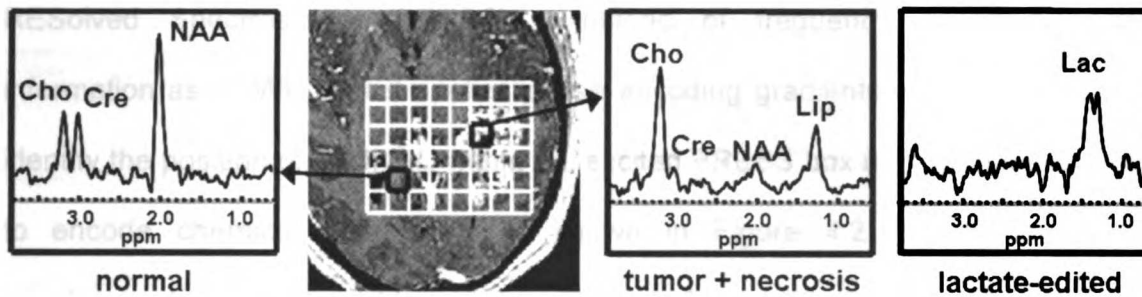


Figure 4.1: Spectra from normal appearing brain tissue, contralateral from tumor location, and voxel from central tumor region in a patient with grade IV glioma

In normal brain, levels of Cho and Cre are similar and the NAA peak is 1.5-2 times larger. Elevated Cho, comprising free choline, phosphocholine, and acetylcholine, is observed in gliomas and thought to be due to increased cell density and membrane turnover. The reduction of NAA in growing gliomas is attributed to displacement and damage of surrounding neurons. As the end product of nonoxidative glycolysis in anaerobic respiration, the presence of lactate can be used as a marker of reduced cellular oxygenation and hypoxia (55-58). Creatine (and phosphocreatine) levels have also been associated with energy metabolism and bioenergetics in tumors and may change in response to increased cellular metabolism within gliomas.(59-61). Elevated lipid levels denote the cellular membrane breakdown associated with cell death and are often observed in spectra from necrotic tissue, where all other metabolic activity is suppressed.

Signal Localization and Magnetic Resonance Spectroscopic Imaging

Magnetic resonance spectroscopic imaging (MRSI) is capable of providing 3-D arrays of spectra, with each gridded voxel representing a specific region of tissue. The signal is localized in space by applying three slice-selective RF pulses to define a box that is the intersection of three orthogonal slabs, a technique known as Point

RESolved Spectroscopy (PRESS). Instead of frequency encoding spatial information as in MRI, MRSI applies phase encoding gradients in each direction to identify the position of each FID within the excited PRESS box and utilizes frequency to encode chemical information as shown in Figure 4.2. Multi-dimensional spectroscopic arrays are obtained through multiple repetitions of the PRESS pulse sequence with gradients applied at varying strengths, followed by a series of post-processing steps depicted in Figure 4.3 (62,63). The degree of metabolic abnormality for each voxel within a heterogeneous region can then be quantified based upon relative metabolite levels and an automated regression technique (64). Numerous studies have implemented MRSI to extract information about brain tumor cellularity and cell membrane breakdown, cellular energetics, neuronal activity, hypoxia, and macroscopic necrosis through its ability to distinguish signals from choline, creatine, NAA, lactate, and lipid molecules (2,60,61,63,65,66).

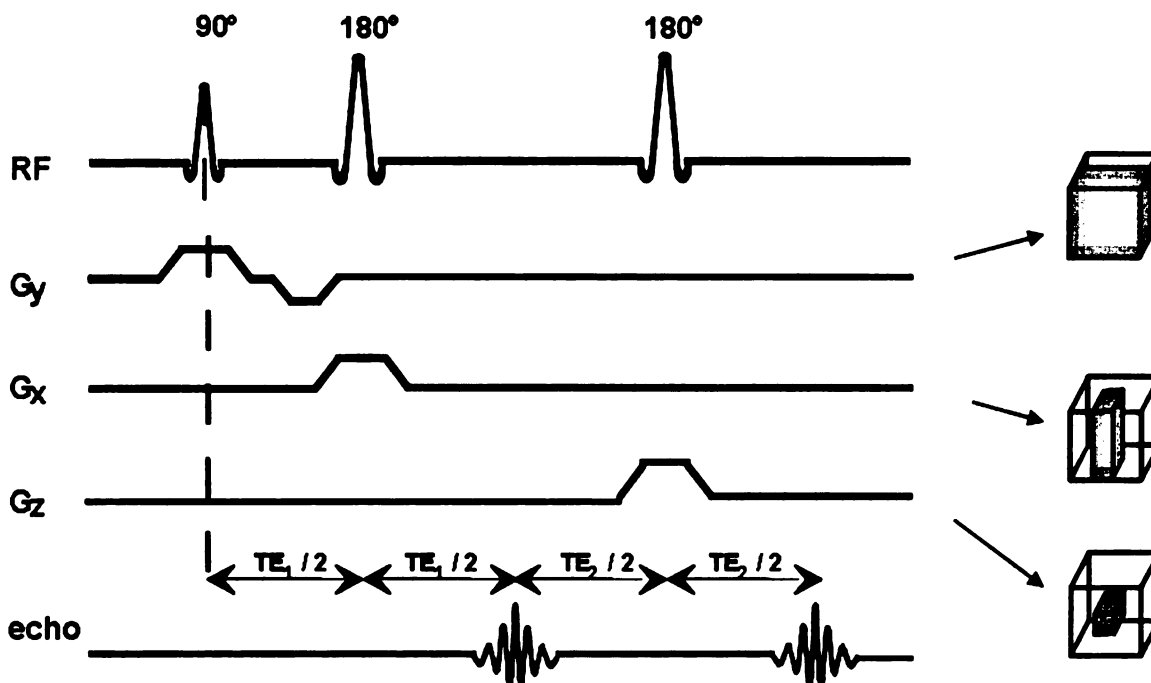


Figure 4.2: Diagram of PRESS pulse sequence for localization of spectra



Figure 4.3: Summary of spectral post-processing

Lactate-Edited MRSI

The lactate resonance overlaps with lipid signals at .9-1.3 ppm in a conventional MRS acquisition, and so spectral editing sequences are required to reliably distinguish them. 3D J-difference lactate-edited MRSI combines PRESS localization with dual BAnd Selective Inversion with Gradient dephasing (BASING) pulses to selectively excite one of the lactate resonances (a quartet at 4.1 ppm), thereby affecting the coupling pattern of the other resonance (a doublet at 1.3 ppm) that overlaps with lipid containing compounds (67-69). Full sensitivity of the lactate doublet is achieved by employing two acquisition cycles per phase encode step in order to discriminate between coupled and uncoupled spins. This means that for the first acquisition cycle, the quartet is placed within the BASING inversion band and the doublet is upright at an echo time of 144ms. In the second acquisition cycle, the quartet resides outside the BASING inversion band and the lactate doublet is inverted. The resulting spectra from each cycle can then be (1) summed to provide spectra containing Cho, Cre, NAA, and lipid peaks and (2) subtracted to reveal an upright lactate doublet. Reduced k-space sampling techniques are simultaneously employed in order to achieve a practical acquisition time for patient studies (6,69).

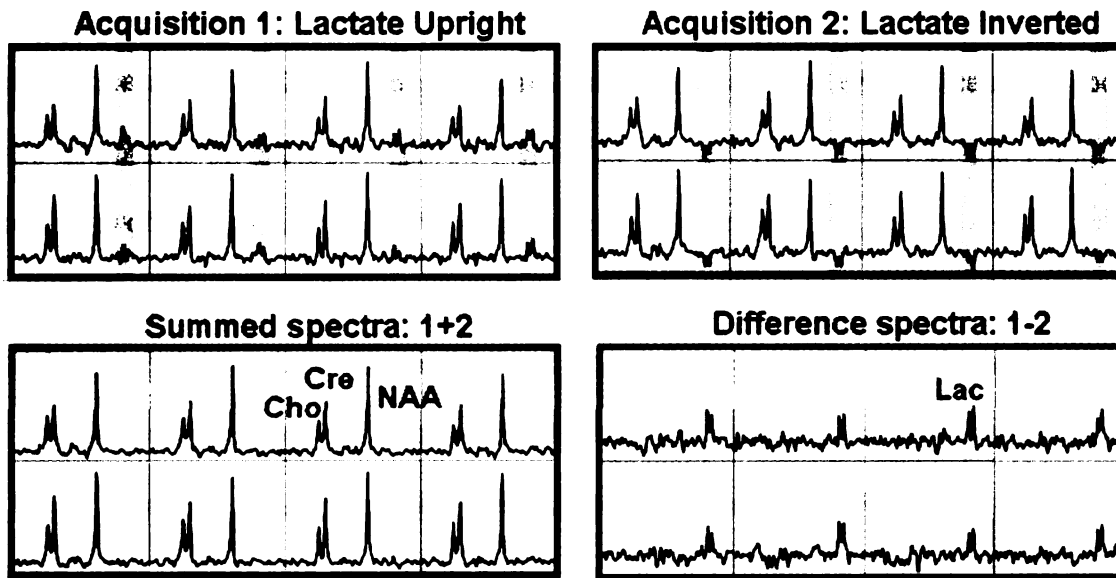


Figure 4.4: Illustration of lactate-edited spectral acquisition cycles

Assessment of Tumor Oxygenation

Although MRSI is an excellent tool for elucidating metabolite levels in brain tissue and quantitatively differentiating between active tumor, necrosis, and edema, it does not provide a direct measurement of changes in tumor vasculature that result in increased vessel volume and/or blood-brain-barrier breakdown and subsequent leakage of contrast agent into brain tissue. DSC MRI facilitates analysis of hemodynamic parameters by tracking an intravenous contrast agent bolus through the vasculature, resulting in a $T2^*$ relaxivity curve proportional to concentration, and therefore, vascular density. Since tumor hypoxia is also related to insufficient perfusion of oxygen from the blood to the surrounding tissue, and is influenced by tortuous, degraded, swollen, and angiogenic tumor vasculature, regions of abnormal perfusion parameters should coexist with elevated lactate and creatine metabolite levels. Assessment of the level of oxygenation is becoming increasingly important in tumors since hypoxia has been shown to be a predictor of aggressive disease,

metastatic spread of tumor cells, and poor response to radiotherapy and chemotherapy (57,70). Thus, surrogate markers for cellular energetics and hypoxia are important physiological parameters that can provide insight to the malignant potential of tumors.

We have shown in Chapter 3 that voxel by voxel comparison of percent recovery and peak height values obtained from a non-parametric model can be employed to independently characterize regions of BBB breakdown and increased vessel volume due to angiogenesis. In addition, regions of abnormal perfusion were found outside the contrast enhancing volume in both grade III and grade IV gliomas. The current section aims to combine lactate-edited 3D MRSI and perfusion-weighted imaging to investigate whether analyzing metabolic levels within regions of abnormal perfusion can assist in characterizing heterogeneity in high-grade gliomas.

4.2 Methods

Patients

MR imaging was performed on 38 untreated brain tumor patients (15 female, 23 male) immediately prior to surgery. Histopathologic analysis of the resected tissue confirmed the diagnosis of 17 grade III gliomas (median age 36; 11 anaplastic astrocytoma, 2 oligodendroglioma, 4 oligoastrocytoma) and 21 grade IV gliomas (median age 58; all glioblastoma).

MR Imaging and Spectroscopic Acquisition

MRI exams were performed on a 1.5T GE Signa Echospeed scanner (GE Healthcare Technologies, Waukesha, WI), using a standard quadrature head coil

with the same MR imaging protocol described in the first section of this chapter. The T2-FLAIR, FSE, and post contrast T1-SPGR images were acquired and used to define regions of T2 hyperintensity and T1 enhancement, while DSC MRI was used to determine locations of abnormal perfusion.

3D J-difference lactate-edited MRSI data were acquired using a PRESS (Point Resolved Spectral Selection) volume localization [TE/TR = 144/1000 ms] with dual BASING (Band Selective Inversion with Gradient dephasing) pulses developed previously in our laboratory (67). CHESS (CHEmical-shift Selective Saturation) and VSS (Very Selective Saturation) pulses were applied for water and outer volume suppression, respectively. The VSS pulses were able to provide a sharper PRESS-selection volume and reduce chemical shift misregistration artifacts (71). The excited PRESS volume (usually 200-300 cm³) was positioned to cover as much as the lesion as possible while avoiding materials such as bone and subcutaneous fat that would complicate shimming and water suppression. Contralateral normal tissue was also included as a reference for post-processing metabolites and region definition. K-space sampling was restricted to the central elliptical region within a 12x12x8 phase encode matrix in order to shorten the acquisition time to approximately half that of the full k-space sampling (69). This technique allowed separation of lactate from lipid within the same total acquisition time (~17 minutes).

Image and Spectra Post-Processing

The metabolite and perfusion images were rigidly aligned to a post-contrast injection 3D SPGR image and resampled to a 32 × 32 grid in-plane with a 16 x 16 cm² field of view. When necessary, the perfusion dataset was aligned to the

anatomical images using affine and perspective transformations or non-rigid B-spline warping (49) by maximizing of normalized mutual information (50). The pixel size of the perfusion data was increased to 5 x 5 mm² resolution so that the observed perfusion signal changes had sufficient signal to noise ratio to be analyzed reliably on a voxel by voxel basis and the degree of interpolation of the metabolite maps was minimized. Peak height and percent recovery of the post bolus signal from the peak were calculated from the $\Delta R2^*$ curve of the perfusion data and normalized to the peak of a model curve function derived from normal appearing brain based on histogram analysis of the pre-contrast echo planar images as described in Chapter 3.2, for each voxel within the PRESS localized volume. Voxels with peak height values greater than twice the model curve were classified as having abnormal peak height, while those whose post-bolus concentration recovered less than 75% from the peak concentration were considered to have abnormal recovery.

The three abnormal perfusion regions were comprised of voxels experiencing (1) abnormal peak height but not abnormal recovery (aPH), (2) abnormal recovery but not abnormal peak height (aRec), or (3) both abnormal peak height and recovery (aPH + aRec). Regions within the T2 lesion that were within the PRESS localization volume were identified by manually delineation on the FLAIR or FSE images. The sub-region that we defined as T2h and used for comparison of metabolite levels excluded regions of contrast enhancement (defined from ROI's on the SPGR), abnormal perfusion, and macroscopic necrosis. Normal appearing white matter (NAWM) regions were determined from visual inspection of spectral voxels and selection of those only located entirely in white matter contralateral to the tumor, without partial voluming with other tissue or contaminated by artifacts. Areas of signal dropout due to susceptibility on the echo planar images were excluded from

all regions. An example of abnormal perfusion, T2h, and NAWM regions overlaid on post-contrast T1-weighted images is shown in Figure 4.5 for a patient with a grade IV glioma. Volumes of aPH, aRec, aPH + aRec, and T2h were calculated and normalized according to the entire T2 lesion volume within the perfusion images.

3D MRSI data were quantified offline using software developed in our laboratory to estimate the levels of choline, creatine, and lactate using the summed and difference spectra from the two acquisition cycles (63). Baseline, phase, and frequency correction parameters from the summed spectra were applied to the difference spectra. Spectral values were determined from the height of each metabolite peak and normalized relative to the noise levels of the right hand end of the spectra.

Statistical Analysis

Metabolite levels were calculated within each region for each patient individually and then averaged across patients within each cohort. Voxels from all patients of the same grade were also combined for each region and mean values of parameters were computed. Statistical significance for differences in metabolite levels between the various regions of the same patient group were quantified using a signed-rank test, while metabolite levels for a given region compared between patient groups were considered significant using a Wilcoxon ranked sum test. P-values less than .05 were considered significant.

4.3 Results

All patients had large regions of T2 hyperintensity that were assumed to correspond to the area at risk for increased metabolic and vascular abnormality. Seven of the seventeen patients with grade III lesions and all twenty-three patients with grade IV lesions exhibited enhancement on the T1-weighted post-contrast SPGR image. While the intention was to cover the entire region of T2 hyperintensity for each lesion, the functional MR and spectroscopic imaging data did not always cover the entire lesion which meant that this was not always possible. The spatial extent of regions with abnormal MR parameters was therefore expressed as a percentage of the portion of the entire T2 lesion that was covered by the PRESS excitation volume.

There was considerable heterogeneity in the distribution of the various abnormal perfusion regions within both grade III and grade IV gliomas as displayed in Figure 4.5. Volumes of abnormal perfusion regions compared to the T2h region were 16% (aPH), 12% (aRec), and 5% (aPH + aRec) for the grade IV lesions and 11% (aPH), 11% (aRec), and 2% (aPH + aRec) for the grade III lesions (see Table 4.1). In both patient populations a decreasing trend was observed in normalized mean volume from aPH to aRec to aPH + aRec regions. When compared to the aPH + aRec region, the volumes of aPH and aRec were significantly larger for both grade III and grade IV gliomas. However, no statistically significant difference was found between aPH and aRec. The normalized mean volumes of aPH + aRec were significantly larger in grade IV than grade III patients, with respective values of 5% and 2%. An increasing trend was observed for aPH volume and aRec volume with grade, but the

differences (11% vs. 16% for aPH and 10% vs. 12% for aRec) were not significant (aPH, $P=.2$ and aRec, $P=.1$).

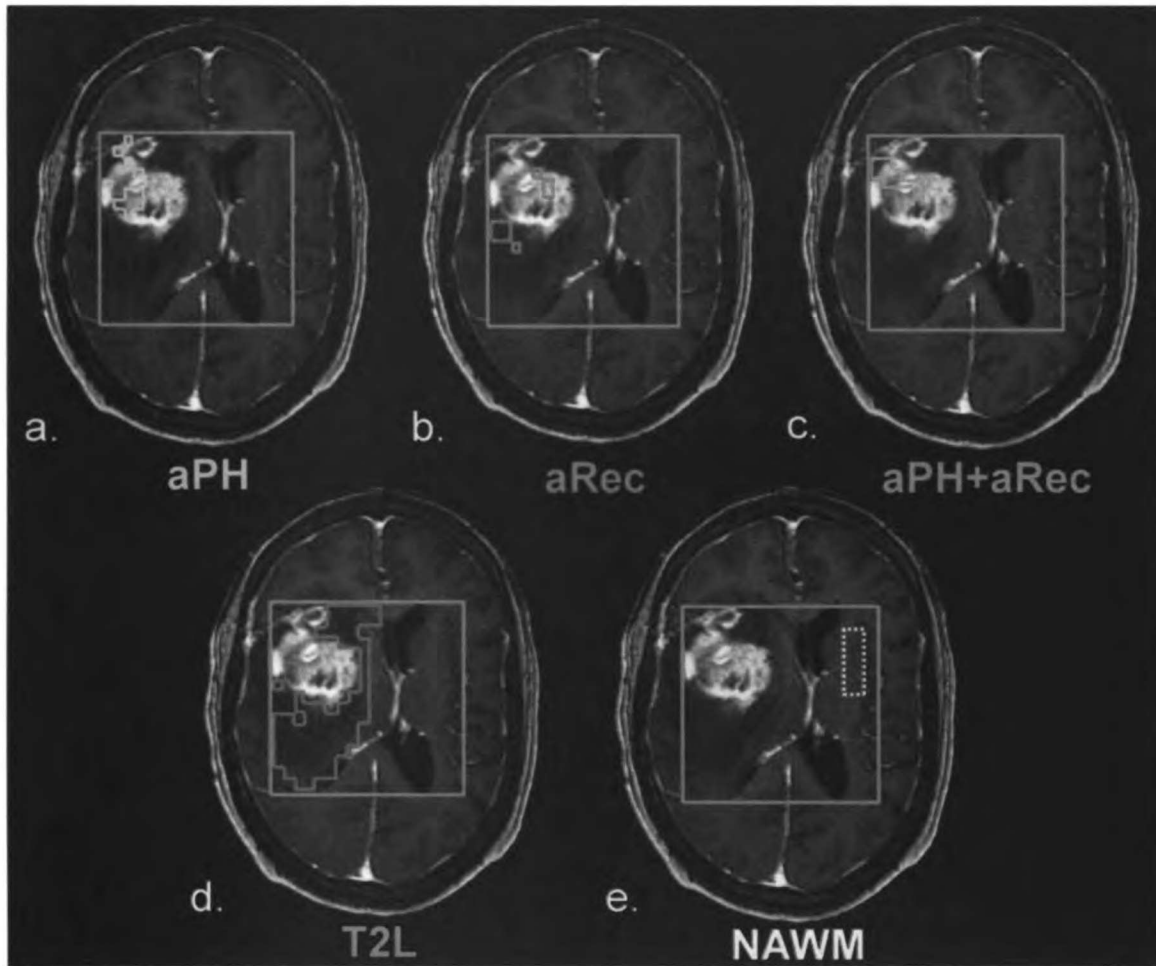


Figure 4.5: Heterogeneity in the distribution of abnormal perfusion regions within a representative grade IV glioma

Table 4.1: Volumes of abnormal perfusion and T2h regions expressed as a percentage of the total T2 lesion volume within the PRESS box

Region	Grade III		Grade IV	
	Volume (%)	No. patients	Volume (%)	No. patients
<i>aPH</i>	11.0 ± 10.5	15	16.3 ± 11.6	20
<i>aRec</i>	10.9 ± 17.5	12	12.3 ± 12.7	20
<i>aPH + aRec</i>	1.6 ± 2.3	10	5.1 ± 6.1	19
<i>T2h</i>	74.4 ± 19.0	16	50.4 ± 17.3	21

Figure 4.6 shows the spectral patterns and regions of abnormal perfusion for a representative non-enhancing grade III patient. From the summed spectra, we notice a clear elevation of choline, especially in the aPH region, and a reduction in creatine levels, most notably in the aRec region, compared to the contralateral NAWM spectra. A uniform presence of increased lactate levels throughout the T1-hypointense lesion is observed from the difference spectra. Figure 4.7 illustrates metabolite maps created from the sum and difference spectra for choline, creatine, and lactate.

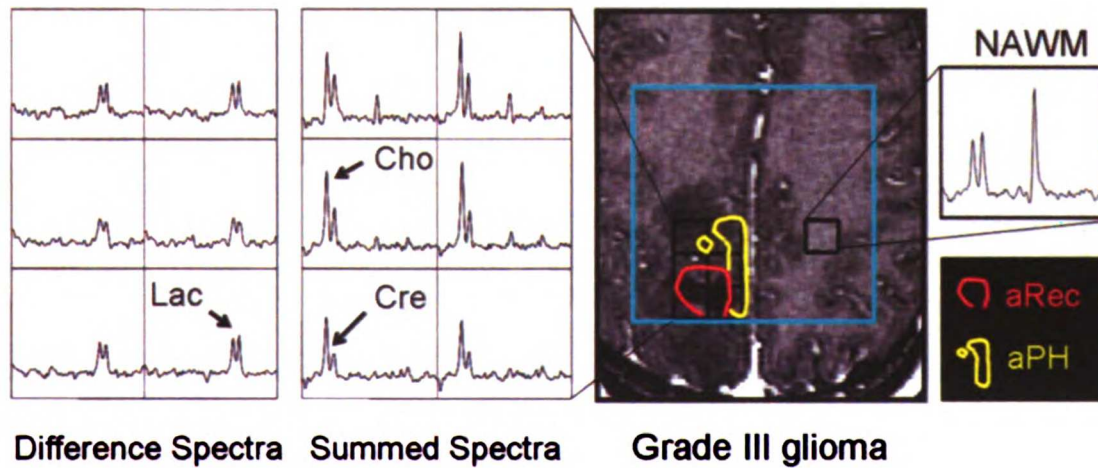


Figure 4.6: Spectral patterns and regions of abnormal perfusion for a representative non-enhancing grade III patient

U.S. LIBRARY

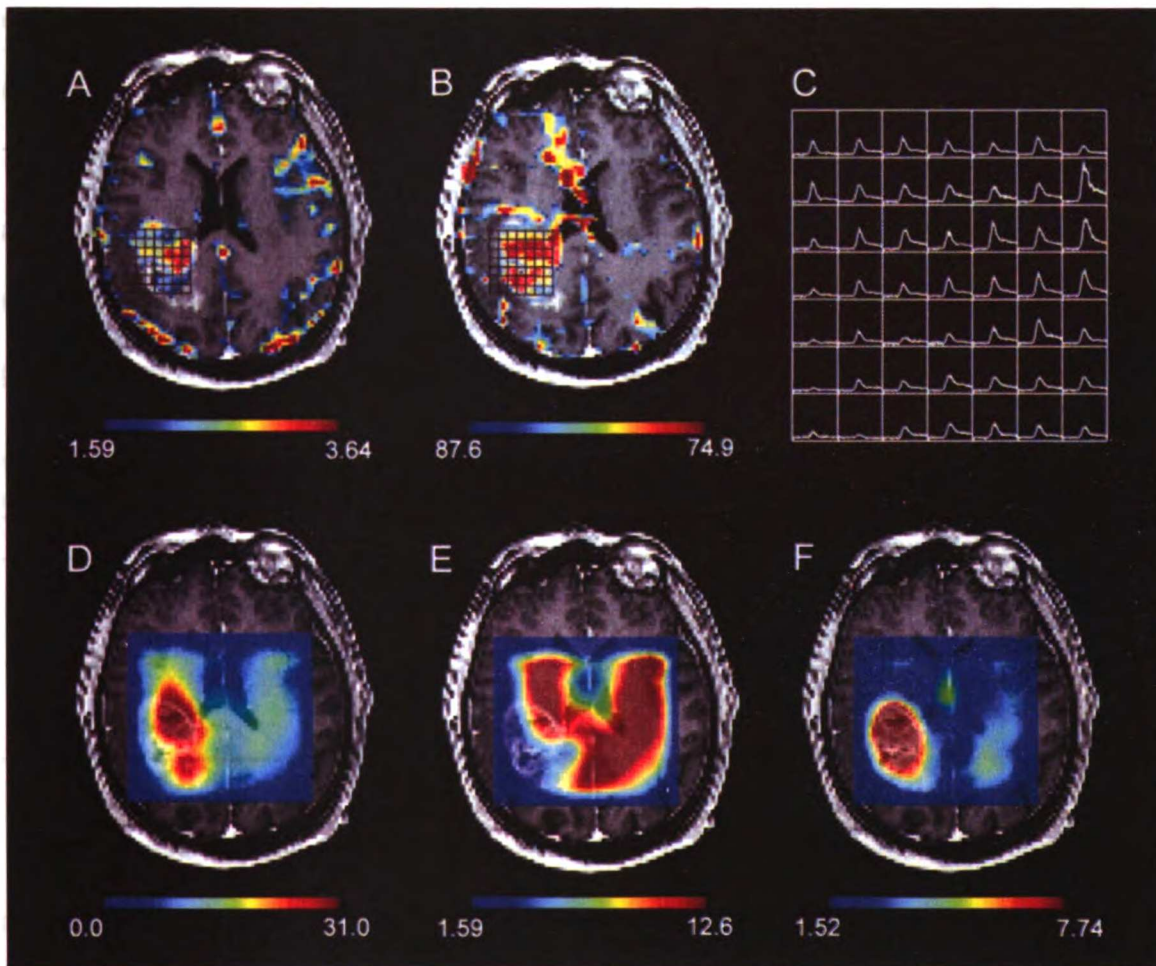


Figure 4.7: Perfusion-derived non-parametric maps of a) peak height and b) percent recovery overlaid on post-contrast T1-weighted images with c) corresponding $\Delta R2^*$ curves for a representative grade IV glioma. In d-f, corresponding metabolite maps of d) choline, e) creatine, and f) lactate.

Different trends were observed for each glioma grade when comparing metabolite levels within the various abnormal perfusion regions compared to the T2h region. For grade IV gliomas (Table 4.2), significantly elevated choline ($P < .02$) was observed in the aPH region compared to the surrounding pure T2 region, while levels of creatine and lactate were similar between these regions ($P > .6$ and $P > .1$, respectively). When comparing the aRec to the T2h region in these same patients, a significant reduction in creatine and increase of lactate levels were also observed ($P < .05$), in addition to elevated choline ($P < .02$). Metabolite peak heights for

choline, creatine, and lactate within the aPH + aRec region were similar to levels observed in the aRec region. All metabolite values within abnormal perfusion and T2h regions were significantly different than those in NAWM, with higher creatine and reduced lactate in NAWM. Choline levels in the different abnormal perfusion regions varied compared to the NAWM region, however, with elevated choline levels greater than NAWM only present in the aPH region.

Table 4.2: Mean metabolite levels within abnormal perfusion and T2h regions compared to contralateral NAWM for grade IV gliomas

Region	Choline	Creatine	Lactate	No. voxels
<i>aPH</i>	17.6 ± 10.2	9.1 ± 5.6	4.3 ± 2.3	54 ± 43
<i>aRec</i>	15.9 ± 7.7	8.2 ± 4.7	4.3 ± 2.6	50 ± 70
<i>aPH + aRec</i>	16.1 ± 8.6	8.1 ± 4.9	4.8 ± 3.3	24 ± 38
<i>T2h</i>	14.4 ± 6.4	9.0 ± 4.7	3.4 ± 2.5	172 ± 117
<i>NAWM</i>	16.4 ± 4.5	14.5 ± 3.6	1.2 ± 1.9	N/A

For grade III patients, no significant differences in metabolite levels was found among regions (Table 4.3) but there was a decreasing trend for creatine in the aRec region compared to all other abnormal perfusion and T2h regions. Creatine was elevated in both the aPH and aPH + aRec regions relative to the T2h region. Choline and lactate levels were similar in all abnormal perfusion and T2h regions, with the exception of a tendency toward increased choline levels in the aPH + aRec region. The lack of significance for these trends was most likely due to the smaller number of patients exhibiting abnormal regions in the grade III cohort. All abnormal perfusion and T2h regions exhibited significantly increased choline and lactate levels and decreased creatine compared to the NAWM region.

Table 4.3: Mean metabolite levels within abnormal perfusion and T2h regions compared to contralateral NAWM for grade III gliomas

Region	Choline	Creatine	Lactate	No. voxels
<i>aPH</i>	18.9 ± 7.1	12.6 ± 4.5	2.9 ± 1.2	31 ± 24
<i>aRec</i>	17.9 ± 8.0	10.6 ± 4.2	2.6 ± 1.5	21 ± 26
<i>aPH + aRec</i>	20.4 ± 9.5	12.7 ± 6.0	2.5 ± 1.9	5 ± 3
<i>T2h</i>	18.9 ± 6.9	11.5 ± 3.6	2.9 ± 1.1	190 ± 122
<i>NAWM</i>	15.2 ± 4.8	14.8 ± 4.4	1.4 ± 1.8	N/A

Lactate levels were significantly elevated in abnormal perfusion regions of grade IV gliomas compared to the corresponding grade III region ($P < .02$, Tables 4.2 and 4.3). Significant differences in choline and creatine between grades were only observed when combining voxels across all patients (Table 4.4). With this analysis, creatine levels were significantly reduced for grade IV patients in all abnormal perfusion and surrounding T2 hyperintense regions except for the *aRec* region. Choline levels within the *aPH* region were significantly elevated in grade III gliomas compared to their grade IV counterparts.

Table 4.4: Comparison of mean metabolite levels within abnormal perfusion and T2h regions from voxels across all patients of each grade

Region	Choline		Creatine	
	Grade III	Grade IV	Grade III	Grade IV
<i>aPH</i>	16.9 ± 9.6	16.5 ± 12.1*	10.7 ± 5.8	7.6 ± 5.9**
<i>aRec</i>	17.9 ± 11.2	16.0 ± 9.4	8.8 ± 5.0	8.2 ± 4.8
<i>aPH+aRec</i>	20.6 ± 12.8	19.0 ± 11.7	11.2 ± 6.9	8.4 ± 5.4*
<i>T2h</i>	18.9 ± 10.7	13.6 ± 8.7	11.0 ± 5.6	8.5 ± 5.5

* $P < 0.02$, ** $P < 0.001$

4.4 Discussion and Conclusions

When the vascular supply is no longer adequate to support the increasing metabolic demands of the rapidly proliferating tumor cells, there is an increased reliance on glycolysis for energy production and this promotes the formation of new blood vessels. Insufficient perfusion of oxygen from the capillary bed to the

surrounding tissue is also caused by tortuous, degraded, and abnormal tumor vasculature. We limited our regions to only abnormal peak height with normal recovery (aPH), only abnormal recovery with normal peak height (aRec), and both abnormal peak height and recovery (aPH + aRec), in order to relate the respective spatial distribution of elevated vessel volume and abnormal recirculation/leakage with metabolic activity, without the confounding effect of tortuosity, which is likely to be manifested as an increase in both parameters and to be in the aPH + aRec region. A 5 mm x 5 mm in-plane resolution was selected as a compromise between ensuring adequate signal to noise of the perfusion data, avoiding over interpolation of metabolite maps, facilitating image registration, and retaining spatial resolution in the definition of our region boundaries, which will eventually be incorporated into treatment planning. The abnormal range of percent recovery and peak height values was determined based on the analysis of the relaxivity curves from normal tissue from Chapter 3.

Grade IV gliomas exhibited the highest choline levels, significantly greater than values found in normal appearing white matter, in the aPH region and suggested increased cell density and/or proliferation. Since increased oxygenation from excess vessels would be available to support the additional and/or rapidly dividing cells, an increase in choline with stable creatine and lactate levels are expected for this region. Within the aRec region, the elevation in choline was accompanied by reductions in creatine and increases in lactate. These changes may reflect the dependence of oxygenation on vascular integrity, where leaky vessels prevent adequate perfusion of oxygen to the surrounding tissue, resulting in anaerobic respiration, the formation of lactate, and lower energy reserves. All metabolite levels

within the aPH + aRec region were similar to those observed in the aRec region, suggesting the presence of leaky vasculature rather than vessel tortuosity.

In grade III gliomas, creatine was the only metabolite that showed differences between abnormal perfusion regions. Decreasing trends were observed in the aRec region and increasing trends in both the aPH and aPH + aRec regions. This may mean that more energy is needed in the initial recruitment and formation of new vessels. None of these trends were significant, however, due to the smaller region sizes and smaller population that was available in the study. The reduction in creatine levels in the aRec region compared to the surrounding pure T2 hyperintensity experienced by grade III patients is consistent with previous findings of lower creatine values for grade III patients in regions of contrast enhancement (27), and supports creatine as a marker for hypoxia, although this reduction may be due to an overall metabolite depression from evolving necrotic tissue.

Grade IV gliomas exhibited significantly elevated Lac compared to grade III gliomas in all abnormal perfusion regions. In grade III patients, the presence of Lac did not appear to be localized to any particular region and the amount of Lac in all abnormal perfusion regions was consistent with levels found in the surrounding T2 hyperintensity. This was consistent with previously published data showing no significant correlation between volumes of elevated lactate and any morphological abnormality (20).

Our results suggest that a reduction in creatine levels and presence of regions with abnormal vasculature may be considered as non-invasive markers of tumor progression from grade III to grade IV gliomas. Increased cellular proliferation, as indicated by elevated choline in the aPH region of grade III gliomas, may initially cause dilation of existing blood vessels and/or the formation of new ones. This

mitosis-induced angiogenic phenomenon is supported by previous studies that demonstrated a positive correlation between vessel volume and choline levels (5). The new vessels that are formed often lack the complex structure of the normal brain vasculature, resulting in increased endothelial permeability. Although diminished creatine levels were observed in regions of microvascular leakage for both glioma grades, lactate levels were only elevated in grade IV tumors. This implicates creatine as an early biomarker of reduced energy reserves from anaerobic respiration prior to lactate accumulation. We hypothesize that once transformation to a more malignant phenotype occurs, the decline of creatine becomes widespread and lactate levels begin to rise, especially in regions with leaky vessels.

An alternative explanation is that the existence of lactate is a marker of hypoxia which induces angiogenesis in tumors (55,58,68). The presence of lactate is the result of heightened glycolytic metabolism within hypoxic regions that are driven by increased proliferation. Li et al found higher rCBV values within regions of elevated lactate and a positive correlation between maximum peak height and volume of lactate of high-grade tumors. In that case vessel wall permeability was not assessed and there was no distinction between the two tumor grades (6,68). The fact that we only observed elevated lactate and reduced creatine within the regions of abnormal recovery suggests that blood-brain-barrier breakdown originating from damage to the existing vasculature plays a role in oxygen depletion. It seems likely that once the angiogenic switch is activated, the oxygenation process is restored as reflected by our results of similar creatine and lactate levels in the aPH region and the surrounding non enhancing T2 lesion. The fact that all metabolite levels within the aPH + aRec region were similar to those observed in the aRec region, further substantiates the importance of vessel integrity on oxygenation. It is possible that the

correlation between lactate and rCBV observed previously may be due to elevated rCBV measurements and microvascular leakage.

While the clinical role of 3D ^1H MRSI and DSC MRI for combined metabolic and vascular assessment of tissue oxygenation requires further evaluation, the current chapter has shown that these two techniques are useful in adding specificity to characterizing spatial heterogeneity in high-grade gliomas. Predicting hypoxic regions would be especially advantageous in determining the most radiosensitive region of the tumor which would respond best to treatment.

Chapter 5: Dynamic Susceptibility-Contrast perfusion MR imaging at 3T

Chapter 3 introduced the use of EPI for DSC MRI as a robust technique in the characterization of abnormal cerebral perfusion in brain tumors. In this chapter, we focus on the limitations of the acquisition, quantification of the artifacts that result, and methods to improve the quality of DSC perfusion MRI when transitioning to from 1.5T to 3T systems.

5.1 Background

Limitations of Echo Planar Imaging

GRE EPI sequences are most commonly utilized for DSC MRI because of their relatively high time resolution and increased sensitivity to changes in T2* relaxivity over time (72). However, EPI techniques also experience heightened sensitivity to image artifacts than conventional imaging methods due to 1) the reversal of every second echo, resulting in N/2 ghosting from misaligned echoes, and 2) the long readout period from which several artifacts described in this chapter arise.

Since the acquisition time for each EPI excitation is longer than what is observed in conventional imaging and both the phase and frequency encode gradients are now played during read out, the effective acquisition time between consecutively sampled points along the phase encode direction is much longer than that of the frequency encode direction. This slow sampling rate or narrow bandwidth per pixel results in several "off-resonance effects" including large fat-water shifts, geometric distortions, and signal loss due to dephasing, in addition to poor spatial resolution

from T2* blurring. The application of fat suppression techniques reduces chemical shift artifacts in the head from misregistration of water and lipid voxels (mainly from the scalp), but other off-resonance effects still remain a challenge, especially at higher field strengths.

Because EPI consists of a series of gradient echoes, the sequence is highly sensitive to main field inhomogeneity off-resonance effects which result in regions of signal dropout and geometric distortion in the image. The off-resonance arises from a spatially varying magnetic field over the imaging volume due to both inherent magnet inhomogeneities and additional magnetic susceptibility differences from the sample being imaged, causing disruptions in the local magnetic field according to Equation 5.1.

$$\Delta B_0 = (\chi_1 - \chi_2) B_0 \quad (5.1)$$

Regions with highly magnetized tissues adjacent to air (termed air-tissue interfaces) produce large disruptions in the local magnetic field, which leads to both dephasing and local phase shifts. Since this effect is not spatially constant, the local phase shifts create geometric distortions and appear as a smearing or blurring of voxels along the phase encode direction in the final image. The amount of local geometric distortion (d) is therefore proportional to the change in field, acquisition time (T_{acq}), and local inhomogeneity difference, but inversely related to the gradient strength (G) and bandwidth as demonstrated in Equation 5.2.

$$d = \Delta B_0 / G \sim \Delta B_0 T_{acq} \quad (5.2)$$

The emergence of high field imaging systems for routine clinical use necessitates the re-evaluation and validation of the GRE-EPI acquisition method through comparison to previously established protocols at lower field. Benefits of imaging at

higher field strengths include longer T1 relaxation times, larger $\Delta R2^*$ changes, and increased SNR that can translate to higher resolution images, increased coverage, or faster acquisitions. However, at higher field strength, increased B_0 inhomogeneity and magnetic susceptibility at air-tissue interfaces exacerbates the effects of signal drop out and geometric distortion artifacts described above, most notably in the phase encode direction, which can confound accurate quantitation from echo planar images (73-77).

Partially Parallel Imaging

Phased-array coils provide the increased sensitivity of individual surface coils with the comparable coverage of larger volume coils. The smaller region of sensitivity for each individual coil reduces the amount of noise received and hence increases the SNR. In partially parallel acquisition methods, phased-array coil elements each simultaneously receive the MR signal and the measurement time is reduced by under-sampling the signal in the Fourier or k-space domain. Under-sampling by a factor of R accelerates acquisition time by R-fold, with the tradeoff of reduced signal-to-noise ratio (SNR). The reduction in the sampling density in k-space is equivalent to reduction of the image field-of-view (FOV) by R times. The missing data points are synthesized after acquisition by incorporating the spatial information from individual coil array elements. The "unaliasing" or parallel reconstruction can be performed either in the spatial or Fourier domain, by direct inversion or indirect reconstruction techniques. Direct techniques like Sensitivity Encoding (SENSE) (78) form the reconstruction matrix by estimating the localized sensitivity of each coil element from a low resolution coil calibration scan and reconstruct the data by direct inversion of the encoding matrix. Indirect techniques,

such as Generalized Autocalibrating Partially Parallel Acquisitions (GRAPPA) (79), acquire a small set of additional phase-encoding lines at the Nyquist sampling frequency that act as training lines for estimating the interpolation weights and then use them to synthesize the skipped phase encoding lines from the acquired lines. Since the coil calibration is built into the actual acquisition in these methods, they are also known as autocalibrating (AC) techniques.

Effects of Parallel Imaging on EPI Artifacts

As discussed at length in the previous sections, the magnitude of distortions due to off-resonance effects is highly dependent upon the receiver bandwidth. In EPI, the phase encode bandwidth corresponds to the echo spacing. Larger receiver bandwidths (or faster sampling rates) in this direction yield a smaller echo spacing between consecutive phase encode lines, resulting in reduced chemical shift artifacts, geometric distortions, and signal dropout. Despite this inherent reduction in SNR, applying parallel imaging acquisition schemes to single shot EPI provide the added benefit of minimizing the amount of geometric distortion and image blurring by decreasing the effective echo spacing and total echo train length (75,76).

Sensitivity Encoding

In SENSE reconstruction, an aliased or reduced FOV image is first obtained for each coil array element as shown in Figure 5.1. The construction of the combined full FOV image is based on the fact that each pixel in the reduced FOV includes the signal contributions from a number of positions in the full FOV. Since the signal superposition from each individual coil image occurs with varying weights based on the local coil sensitivity at that location, an $n_c \times n_p$ sensitivity matrix (S) needs to be

constructed for each voxel in the reduced FOV image where n_c refers to the number of coils and n_p the number of superimposed pixels.

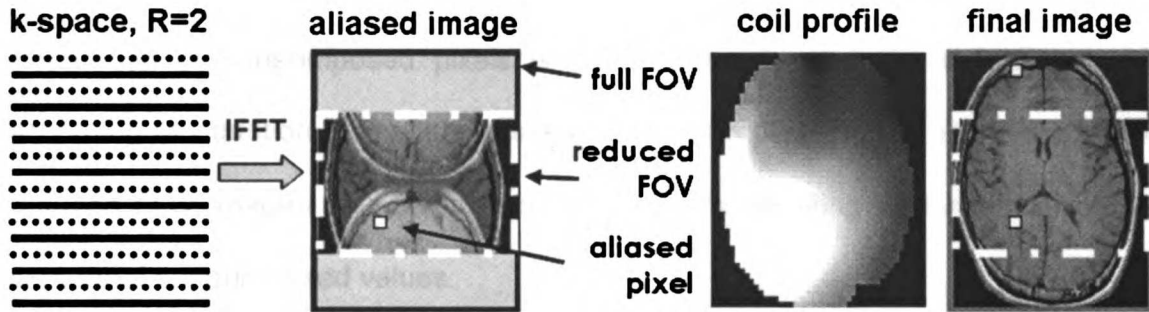


Figure 5.1: Illustration of SENSE for a reduction factor of two

The sensitivity matrix is formulated from normalized individual coil profile images, obtained from either reference measurements on a uniform phantom whose size is larger than any object imaged, or a proton-density weighted, low resolution fGRE calibration scan at the time of acquisition. If the latter method is selected, each individual coil profile image must be normalized or divided by a body coil image or sum-of-squares coil map to remove any variation of signal intensity due to the contrast of the object and scale the intensity values to an appropriate range for successful matrix inversion. Additional low pass filtering may also be applied for noise removal as long as errors at the objects edges are corrected, usually either through edge completion or polynomial fitting algorithms (78,80).

The unfolding matrix (U) is then calculated by taking the pseudoinverse of the sensitivity matrix multiplied by the receiver noise matrix (Ψ) as described in Equation 5.3, where H denotes the transposed complex conjugate.

$$U = (S^H \Psi^{-1} S)^{-1} S^H \Psi^{-1} \quad (5.3)$$

The receiver noise matrix describes the level of correlated noise among any two receive channels (γ, γ') and is modeled under the assumption that the noise in each

γ -th channel (η_γ) arises from mutually independent noise sources with Gaussian statistics and is calculated using Equation 5.4.

$$\Psi_{\gamma\gamma} = \frac{1}{2} [\sigma^2(\eta_\gamma + i\eta_\gamma) + i\sigma^2(\eta_\gamma - i\eta_\gamma) - (1 + i)[\sigma^2(\eta_\gamma) + \sigma^2(i\eta_\gamma)]] \quad (5.4)$$

Separation of superimposed pixels is then achieved using the unfolding matrix according to Equation 5.5, where \mathbf{a} is a vector of complex image values from all the reduced FOV images of a given voxel and \mathbf{v} is the resulting vector containing the separated superimposed values.

$$\mathbf{v} = \mathbf{U}\mathbf{a} \quad (5.5)$$

The unfolding procedure is then repeated for each voxel in the full FOV image. Voxels that are outside the object are excluded from the reconstruction.

SNR concerns with SENSE

Although multi-channel coil arrays along with a partially parallel imaging acquisition and SENSE reconstruction algorithms have been shown to improve image quality by minimizing susceptibility-induced artifacts, the penalty is a decline in SNR. (8-10,75,81,82) This reduction is highly dependent on both the reduction factor and coil geometry (measured by the geometry factor, g), as displayed in Equation 5.6.

$$\text{SNR}_{\text{red}} = \text{SNR}_{\text{full}} / (g\sqrt{R}) \quad (5.6)$$

SENSE reconstruction is affected by both sample noise and noise from estimation of the coil sensitivity profiles. Since the receiver noise matrix inherently represents body-noise dominance, the latter can be considered negligible assuming the coil sensitivity maps are adequately processed. However, image noise is based on both receiver sample noise and noise from the unfolding reconstruction. Unlike conventional imaging, the noise level in SENSE images vary among pixels and

correlated noise exists between superimposed voxels. Thus, the local geometry factor (g) given in Equation 5.7, is used to describe the ability of SENSE reconstruction to accurately separate the aliased superimposed voxels for the given coil configuration and, in the ideal case, would be equal to one.

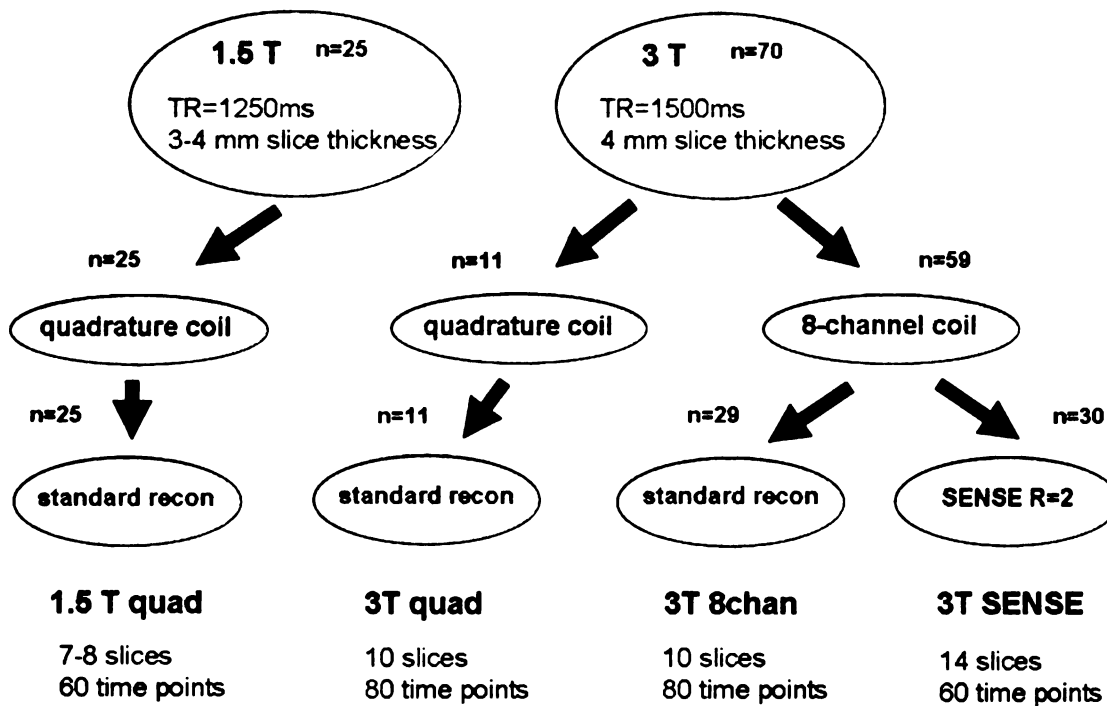
$$g = \sqrt{(S^H \Psi^{-1} S)^{-1} S^H \Psi^{-1} S} \quad (5.7)$$

5.2 Estimation of Dynamic SNR and Effects of T1 Relaxation

Patient Population and Imaging Acquisition

Eighty patients suspected of brain tumors (mean age 47, range 25 to 84) and scanned sequentially at our institution over the course of nine months were included in this study. Histology confirmed seventy-eight of the suspected tumors as primary gliomas with classification ranging from grade II – grade IV, one as a small hemorrhagic infarct, and one as a medulloblastoma. Ninety-five DSC MRI exams from eighty patients were performed on either a 1.5T or 3T EXCITE GE Signa Echospeed scanner (GE Healthcare Technologies, Waukesha, WI) with acquisition parameters listed in Figure 5.2.

Pre-contrast injection T1- and T2-weighted images were acquired and used in region segmentation and image registration. A proton density weighted fast gradient-echo scan (fGRE; 150/2.1 ms [TR/TE], 50° flip angle, 64 x 64 x 35 matrix size, 30 x 30 x 17.5 cm FOV) was performed in order to estimate coil sensitivity profiles needed for the SENSE reconstruction. SENSE images were reconstructed as described previously (78), while fully-encoded multi-coil images were combined using the traditional sum-of-squares method.



* All acquisition groups utilized a TE of 54 ms, 35° flip angle, 26 × 26 cm² in-plane FOV, 128 × 128 reconstructed image matrix.

Figure 5.2: Acquisition subgroups and scan parameters

Region Definition

For each exam, dynamic SNR was calculated within two regions: normal-appearing brain tissue (NABT) and normal-appearing white matter (NAWM), as shown by Figure 5.3. The automated routine described in Chapter 3 to segment NABT voxels based on histogram analysis of the image intensities from the pre-contrast echo planar images was utilized to exclude curves within the T2 and contrast enhancing lesions, ventricles, large veins, and necrotic regions (Figure 5.3d). For the NAWM dynamic SNR calculation, the pre-contrast T1-weighted and T2-weighted images were segmented into grey matter, normal-appearing white matter (Figure 5.3b), CSF, and lesion compartments using a hidden Markov random

field model with an expectation-maximization algorithm (83). In order to only include voxels/regions of complete overlap between the anatomical and distorted perfusion images, a series of erosions interjected with eliminations of non-contiguous pixels was performed at the 5mm x 5mm perfusion resolution on the anatomical NAWM compartment. The final NAWM region is shown in Figure 5.3c, with contour overlaid on a pre-contrast echo planar image. Mean dynamic SNR values from NAWM and NABT voxels were determined for each patient and then averaged across all patients within each group: 1) 1.5T, quadrature coil; 2) 3T, quadrature coil; 3) 3T, 8-channel coil; and 4) 3T, 8-channel coil with SENSE.

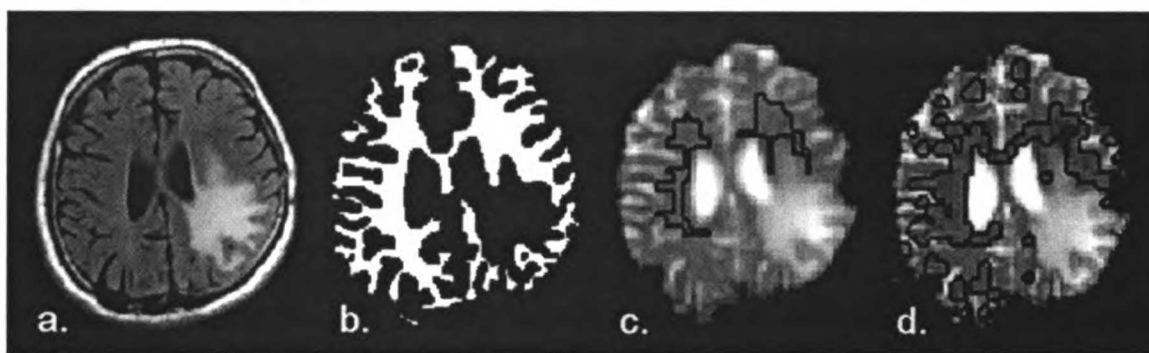


Figure 5.3: Generation of normal appearing white matter (NAWM) and normal appearing brain tissue (NABT) regions used in dynamic SNR estimation.

Dynamic and Image SNR Calculations

Dynamic SNR was defined as the peak height of the $\Delta R2^*$ curve divided by the standard deviation of variations in intensity of 16 points from the pre-contrast injection baseline noise. In order to assure that any differences in dynamic SNR values among acquisitions were not due to T1 effects, the mean of the last five points of the post-bolus baseline $\Delta R2^*$ signal relative to the pre-contrast injection baseline noise was also examined for NAWM regions.

Histogram-derived indices of image SNR and dynamic SNR were computed at the acquired resolution from all voxels combined across patients. Image SNR was calculated from the first time point of the echo planar perfusion images. Brain tissue was segmented from background noise, residual unsuppressed fat, and Nyquist ghosting for each exam. Noise values were determined by manually defining regions of interest outside the image and any residual artifacts. Voxel values from all exams within a group were combined and normalized by the total number of voxels for each patient in order to create histograms of image and dynamic SNR. Peak position and full width at half max, as well as 75th and 95th percentiles of the histograms were calculated for each group. Dynamic SNR values less than four were excluded from the histograms in order to avoid incorrect characterization of signal change yielding a false shift in peak position to lower SNR values.

Results

A slice from the first time point of the dynamic echo planar image series and corresponding $\Delta R2^*$ curves for normal-appearing white matter using a 1.5T quadrature coil, 3T quadrature coil, 3T 8-channel coil, and 3T 8-channel coil with SENSE acquisitions are displayed in Figure 5.4(a-d). As expected, visual inspection of these curves portrays a clear elevation in dynamic SNR with both increasing field strength and number of reception coils. Relative cerebral blood volume maps generated from integrating the area underneath the first pass bolus are overlaid on the echo planar images. The elevated dynamic SNR resulted in a greater signal change that facilitated estimation of rCBV maps.

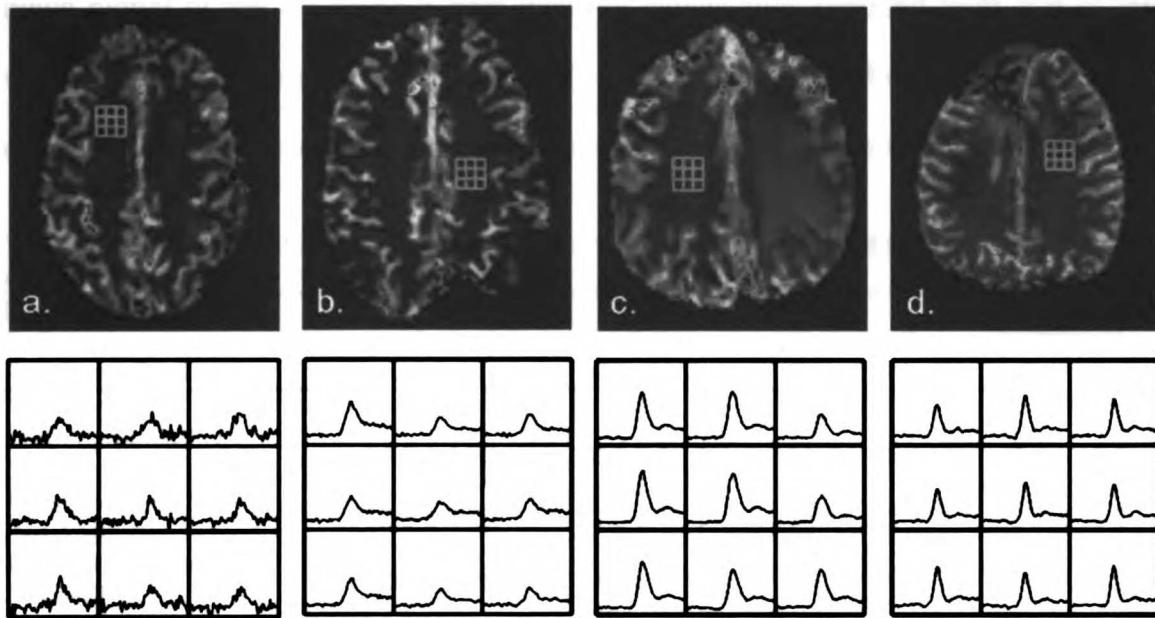


Figure 5.4: First time point pre-contrast EPI volume with rCBV map overlay and corresponding white matter $\Delta R2^*$ curves for (a) quadrature coil at 1.5T, (b) quadrature coil at 3T, (c) 8-channel coil at 3T, and (d) 8-channel coil with SENSE at 3T

Dynamic SNR values within NABT and NAWM as well as post-bolus signal change are listed in Table 5.1. The 1.5T data that were acquired with a 3 mm slice thickness were normalized to the 4 mm thickness of the 3T data. A 2.6-fold elevation in mean dynamic SNR with field strength ($P < .001$) and a 1.6-fold and 1.7-fold increase with coil type is observed for both NABT ($P < .005$) and NAWM ($P < .002$), respectively. Similar increases were found in the post-bolus signal within the NAWM (2.5-fold and 1.7-fold elevations with field strength and coil type, respectively; $P < .001$). The mean percent recovery of the post-bolus signal from the peak height was 81% for all three standard reconstruction acquisitions, regardless of coil or field strength. Although the addition of SENSE at 3T significantly reduces mean dynamic SNR by 21% and 22% for NABT ($P < .02$) and NAWM ($P < .05$), the values are still 1.3 and 1.4 times higher than those obtained from the 3T head coil acquisition, though the difference is not statistically significant ($P = .2$). The post

bolus signal of the 3T SENSE data was not significantly reduced from that of the standard 3T 8-channel coil acquisition (7.4% compared to the 22% decrease in dynamic SNR) and the mean percent recovery for this acquisition was only 78%.

Table 5.1: Dynamic SNR, post-bolus SNR, and dynamic to post-bolus SNR ratio in NABT and NAWM regions

Field strength Coil Recon method	1.5T quadrature standard	3T quadrature standard	3T 8-channel Standard	3T 8-channel SENSE
<i>No. exams</i>	25	11	29	30
<i>Mean dynamic SNR (NABT)</i>	14.6 ± 4.99	38.1 ± 12.4	61.3 ± 25.2	48.2 ± 16.4
<i>Mean dynamic SNR (NAWM)</i>	12.5 ± 4.19	32.1 ± 13.2	55.9 ± 23.4	43.6 ± 15.2
<i>Mean post-bolus SNR (NAWM)</i>	2.30 ± 0.79	5.67 ± 2.30	9.73 ± 3.21	9.02 ± 3.05
<i>Dynamic to post-bolus SNR ratio (NAWM)</i>	5.78 ± 1.75	6.02 ± 2.36	5.77 ± 1.36	5.05 ± 1.36

The differences in dynamic and image SNR among acquisitions are depicted by the histograms displayed in Figure 5.5. A significant increase is observed for the peak position and width, as well as 75th and 95th percentiles, for both dynamic and image SNR with escalating field strength and number of coils as displayed in Tables 5.2 and 5.3 (with $P < .0001$ and $P < .05$ for all image and dynamic SNR histogram indices).

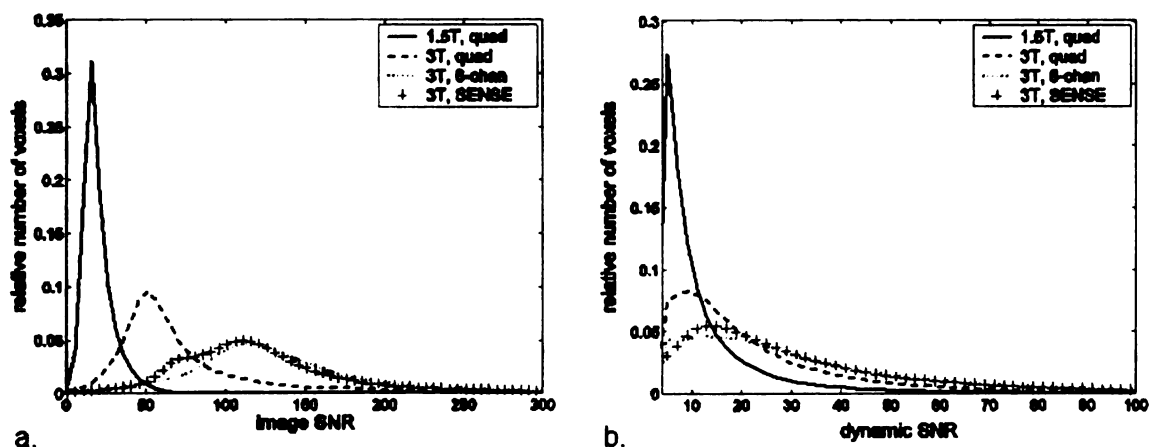


Figure 5.5: Whole brain histograms of (a) image SNR and (b) dynamic SNR

Table 5.2: Histogram-derived indices of dynamic SNR for each acquisition

Field strength	1.5T	3T	3T	3T
Coil	quadrature	quadrature	8-channel	8-channel
Recon method	standard	standard	standard	SENSE
<i>Peak location</i>	6.8 ± 0.8	11.1 ± 3.4	17.3 ± 9.5	17.8 ± 6.2
<i>Peak width</i>	8.9 ± 2.0	18.3 ± 6.5	34.3 ± 19	28.6 ± 11
<i>75th percentile</i>	16.1 ± 4.4	29.4 ± 8.1	45.2 ± 21	44.5 ± 16
<i>95th percentile</i>	39.0 ± 12	65.9 ± 17	91.7 ± 39	88.2 ± 30

Table 5.3: Histogram-derived indices of image SNR for each acquisition

Field strength	1.5T	3T	3T	3T
Coil	quadrature	quadrature	8-channel	8-channel
Recon method	standard	standard	standard	SENSE
<i>Peak location</i>	19 ± 2.6	52.8 ± 9.0	112 ± 21	107 ± 21
<i>Peak width</i>	10 ± 2.2	32.7 ± 7.3	57.9 ± 11	46 ± 12
<i>75th percentile</i>	26.7 ± 4.1	83.3 ± 13	164 ± 29	152 ± 34
<i>95th percentile</i>	44.7 ± 6.9	176 ± 37	303 ± 72	276 ± 74

For image SNR, a 2.8-fold and 2.1-fold larger average peak position value, representing the most frequent SNR value within the whole brain, were observed with increase in field strength and number of coils, respectively. Only a 5% reduction ($P = .2$) in image SNR peak position was encountered with the implementation of a partially parallel acquisition with SENSE reconstruction compared to the conventional 8-channel coil acquisition at 3T. The heightened image SNR values with increasing field strength is even more apparent for regions with higher signal intensity, as exemplified by the 3.1-fold increase in 75th percentile values and 3.9-fold increase in 95th percentiles between 1.5T and 3T head coil data. A 1.9-fold and 1.7-fold increase in 75th and 95th percentiles were observed between the standard quadrature and 8-channel phased-array coil, with only a 7.2% ($P = .04$) and 8.9% ($P = .06$) respective decrease with the application of SENSE. Similar trends were observed for dynamic SNR, but their whole brain differences were less prominent compared to both the image SNR and mean dynamic SNR within NBT

and NAWM results. Nonetheless, statistically significant differences were observed between field strengths (with $P < .0001$ for all histogram indices) and coil types (with $P < .05$ for all histogram indices), but not acquisition method ($P > .2$ for all indices).

5.3 Quantification of Geometric Distortion with Non-rigid Registration

Geometric distortions that are characteristic of the EPI pulse sequence make it difficult to accurately co-register multi-modality MRI. The latter is a growing necessity as parameters derived from functional imaging are routinely incorporated in surgical guidance, planning radiotherapy, and studies that attempt to define boundaries of and correlate parameters within heterogeneous tumor regions (5,52,84). Although post-processing methods such as non-rigid image registration using deformation fields parameterized by cubic B-splines have been verified as accurately transforming distorted echo planar images to a distortion-free reference (49,85), the resulting unwarped images still suffer from susceptibility-induced signal dropout and potential signal intensity errors in regions experiencing large displacements. In addition, the extent to which these registration routines affect parameter estimations derived from the unwarped data is unclear. Nonetheless, the computed transformation can be useful in characterizing and quantifying the amount of distortion present in order to compare various acquisition techniques.

An additional standard GRE EPI sequence was acquired for seventeen of the thirty patients who had undergone the SENSE acquisition at 3T, utilizing the same imaging parameters and slice prescription. Both the standard and SENSE EPI volumes were registered to a geometrically accurate pre-contrast, T1-weighted SPGR reference image by non-rigid B-spline warping through maximization of

normalized mutual information (49,50). The registration results yielded an array of B-spline control points which define deformation vectors that map the positions of the distorted echo planar images to the undistorted reference image. Axial distortion maps for each direction (frequency encode (L/R), phase encode (A/P), and slice select (S/I)) can be derived by separating the deformation vectors into their x-, y-, and z- components respectively. However, in order to directly compare or quantify the amount of distortion in a particular direction between acquisitions, the displacement of any voxel *from* the reference image *to* the echo planar image must first be determined. Since the mapping from a voxel in the echo planar image does not necessarily correspond to a voxel center location on the target reference image, numerical inversion of the distortion maps was computed. For each voxel in the reference image, the corresponding EPI coordinate was found by using a gradient descent algorithm to minimize the distance between the reference voxel and the mapped EPI coordinate in the reference frame. The distortion vectors were then defined as the Δx , Δy , and Δz that would transform each reference voxel to its corresponding point in the EPI frame.

The degree of geometric distortion was quantified from the displacement maps within two regions of interest: the whole brain and outer rim. Here, we focus only on in-plane displacements in L/R and A/P since distortion from the echo planar 2D-multislice acquisition is small and not expected to be affected by the parallel acquisition in the S/I direction. Both whole brain and rim regions were restricted to the intersection of the reference image and the echo planar image transformed into the reference frame, in order to eliminate voxels in the reference image that have no corresponding points in either echo planar image. The rim region extended approximately 1.3 cm inward from the edge of the brain. For each directional

distortion map (L/R, A/P), a scatter plot of displacement values was generated for the standard and SENSE EPI acquisitions. Principal component analysis was then implemented in order to determine the directionality of the variance in the scatter plots. The slope of the dataset was then computed from the first principal component of the data. Median, maximum, and 95th percentile values of distortion, as well as the number of voxels that experienced a displacement of at least 2 mm (one EPI pixel), were then calculated within the whole brain and rim regions for each acquisition in the A/P and L/R directions.

Volumes of geometric distortion were defined as the magnitude of the difference between the masked volumes of the warped and acquired images. The amount of signal dropout was quantified by subtracting the masks of the standard and SENSE warped volumes from the T1-weighted reference volume resampled to the perfusion plane, and expressed as a percentage of the reference volume.

5.4 Assessment of Susceptibility-Induced Artifacts

A notable increase of magnetic susceptibility induced EPI artifacts was observed with higher field strength as shown in Figure 5.6(a-b), which displays representative echo planar images obtained from the same brain tumor patient scanned at (a) 1.5T, (b) 3T without SENSE. The SENSE EPI acquisition helped improve image quality by minimizing the effects of these artifacts (Figure 5.6c). Figure 5.6(d-e) depicts noticeable distortion and signal drop out around air/tissue interfaces of the standard (d) and SENSE EPI (e) images compared to the surrounding T1-weighted reference contour. The reduction of signal dropout and posterior distortion with the addition of SENSE at 3T is evident in (Figure 5.6e). The most obvious distortion evident in

these images occurs in the phase encoding direction, where a prominent nonlinear displacement of voxels is observed at both the anterior and posterior edges of an axial brain slice. This movement results in a spreading of frontal lobe voxels outside of the head and compression of the image at the base of the skull. Also evident in Figure 5.6 is the anterior compression and posterior expansion of the brain in the L/R direction. Signal cancellation is evident in regions where there is a juxtaposition of two materials with different magnetic susceptibility, such as the air-tissue interface present above the sinuses.

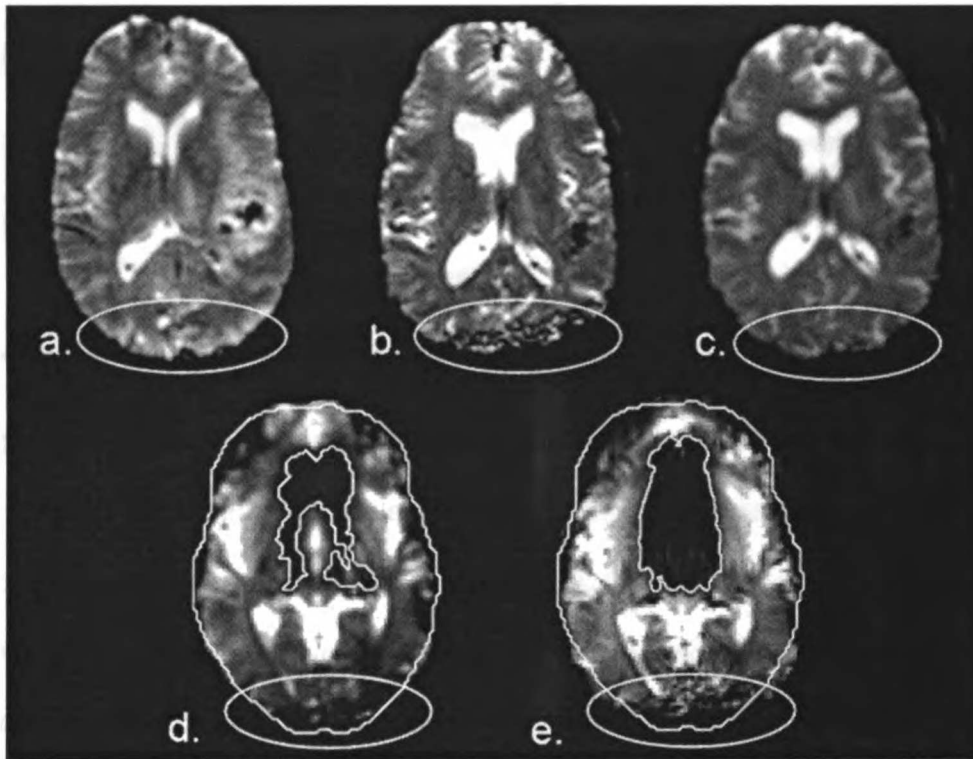


Figure 5.6: Depiction of geometric distortion and signal dropout in representative echo planar images obtained from the same brain tumor patient

Representative distortion maps of the standard EPI acquisition that were generated for each direction (L/R, A/P) are displayed in Figure 5.7(a,b), illustrating the displacement of each reference voxel on the T1-weighted image to its

corresponding point in the EPI frame. Negative intensity values (appearing darker gray to black) correspond to anterior or upward displacements in the phase encode direction and movement to the radiological left side of the brain along the readout direction. These maps accurately characterize the anticipated upward displacement along the anterior and posterior rims of the brain, as well as the often overlooked L/R compression and expansion of the image in the anterior and posterior hemispheres, respectively.

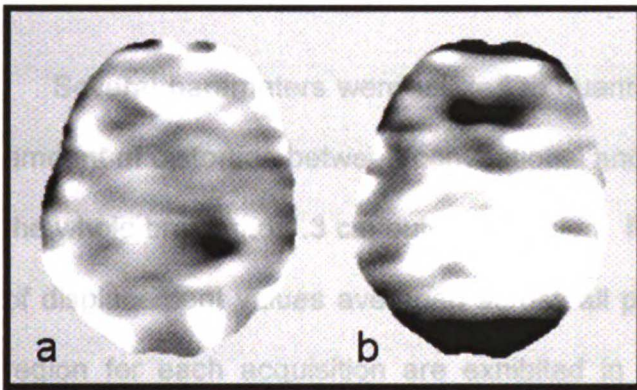


Figure 5.7: Axial distortion maps depicting the inverse transformation of the standard EPI acquisition for (a) the frequency encode direction (L/R) and (b) phase encode direction (A/P)

Figure 5.8 displays the histograms of voxels from all patients combined in a given region, plotted on a semi-log scale. Symmetry of L/R distribution reflects balanced anterior compression and posterior expansion in the frequency-encode direction on an axial slice. The negative tail of A/P histogram represents the overall anterior displacement of voxels along the phase encode axis. The SENSE EPI acquisition appears to reduce the number of voxels experiencing large anterior shifts in the phase-encode direction.

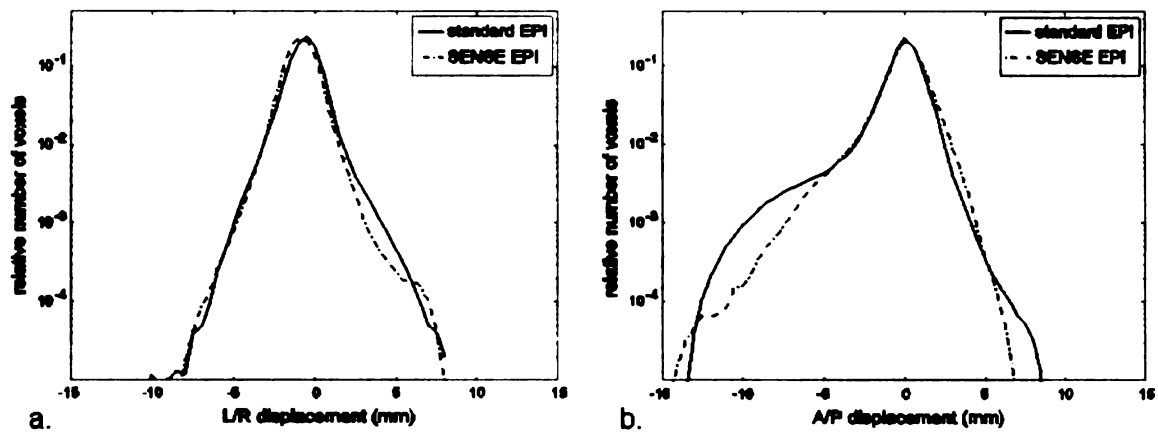


Figure 5.8: Displacement histograms for (a) the frequency encode direction (L/R) and (b) phase encode direction (A/P) plotted on a semi-logarithmic scale.

Several parameters were utilized to quantitatively characterize and compare the amount of distortion between conventional and SENSE EPI acquisitions at 3T, within the whole brain and 1.3 cm outer rim region. Median, maximum, and 95th percentiles of displacement values averaged across all patients within the whole brain and rim region for each acquisition are exhibited in Tables 5.4 and 5.5 for L/R and A/P directions.

Table 5.4: Histogram-derived indices of frequency magnitude displacement in mm for the whole brain region

Displacement direction	Histogram index	standard	SENSE	<i>P</i> value
<i>Frequency encode (L/R)</i>	<i>Median</i>	2.4 ± .12	2.3 ± .12	<i>P</i> < .005
	<i>Maximum</i>	6.8 ± 1.3	5.6 ± 1.4	<i>P</i> < .01
	<i>95th percentile</i>	2.4 ± .32	2.4 ± .45	<i>P</i> > .5
<i>Phase encode (A/P)</i>	<i>Median</i>	3.6 ± .33	2.6 ± .20	<i>P</i> < .001
	<i>Maximum</i>	10.6 ± 2.7	9.2 ± 2.5	<i>P</i> < .05
	<i>95th percentile</i>	3.5 ± .91	3.0 ± .70	<i>P</i> < .01

Table 5.5: Histogram-derived indices of magnitude displacement in mm for the rim region with standard

Displacement direction	Histogram index	standard	SENSE	P value
<i>Frequency encode (L/R)</i>	<i>Median</i>	2.7 ± .19	2.5 ± .32	<i>P</i> < .05
	<i>Maximum</i>	6.8 ± 1.3	5.6 ± 1.4	<i>P</i> < .01
	<i>95th percentile</i>	3.6 ± .46	3.3 ± .85	<i>P</i> < .05
<i>Phase encode (A/P)</i>	<i>Median</i>	4.1 ± 1.0	3.4 ± .66	<i>P</i> < .005
	<i>Maximum</i>	10.5 ± 2.7	9.1 ± 2.5	<i>P</i> < .05
	<i>95th percentile</i>	7.1 ± 2.0	5.3 ± 1.4	<i>P</i> < .001

When SENSE was applied, a significant reduction of all histogram indices was observed in the both the whole brain and rim regions for the A/P direction, with the average percent reduction ranging from 13-28%. The most notable changes in the whole brain region were observed for the median displacement (a 28% decrease), while in the rim region, the SENSE EPI acquisition exhibited the most reduction in the 95th percentile index (25%). The decline in magnitude of displacement with the implementation of SENSE for the L/R direction was not as prominent however, with the greatest average change (a 17% decrease) evident in the maximum displacement parameter, and no difference present in the 95th percentile index within the whole brain. There was also no significant difference in the number of voxels experiencing greater than 2mm (one EPI voxel) displacement between groups for either direction.

Figure 5.9 depicts the 2D histograms of displacement values that were generated of the standard and SENSE EPI acquisitions for each directional distortion map (L/R, A/P), in the whole brain region for all patients on a semi-logarithmic scale. The intensity is proportional to the logarithm of the bin height, in order to emphasize low frequency components. This method for displaying the data allowed displacement

measures to be directly compared on a voxel by voxel basis. Principal component analysis was implemented to determine the directionality of the variance in the histograms. The dashed line in Figure 5.9 represents the slope of the dataset computed from the first principal component of the data and the dotted line is unity. The first principal component of the data, representing the total least squares regression line, was greater than one for all but three out of seventeen patients in the A/P direction for both the whole brain and rim regions, indicating increased distortion in the phase-encode direction for the standard EPI acquisition (plotted on the y-axis). In the L/R direction, two patients showed slopes less than one, four equal to one, and eleven greater than one within the whole brain, while only one and three patients exhibited slopes less than and equal to one when focusing on the rim region only. All comparisons in all regions and directions were significantly larger than one ($P < .02$).

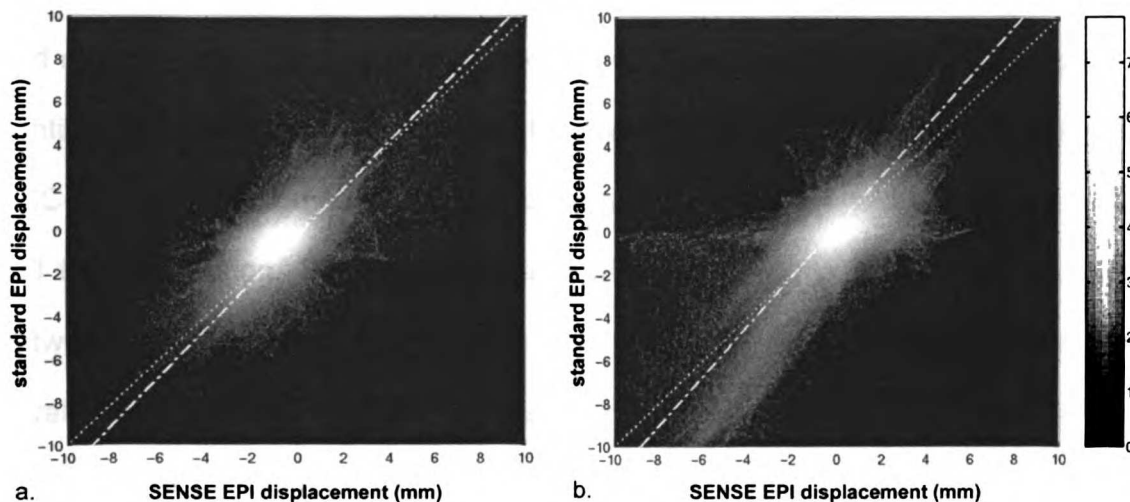


Figure 5.9: 2D histogram showing the relationship between displacement values for the standard and SENSE EPI acquisitions in the (a) readout and (b) phase-encode directions for all patients.

The volume of signal dropout was calculated for both the standard and SENSE EPI acquisitions. The decline in signal dropout volume with the implementation of a SENSE acquisition ranged from 2.0 – 11.5% with greater reductions observed in patients with more inferior lesions. The median difference in signal dropout was $3.5 \pm 2.4\%$, which proved to be significant in a paired signed-rank comparison ($P < .001$).

5.5 Discussion and Conclusions

Dynamic susceptibility contrast MRI is an emerging modality that is becoming more widely incorporated into the standard imaging protocol for patients with brain tumors. The concurrent impetus for deployment of higher field scanners, along with recent FDA approval of scanners with field strengths of 3T for clinical use, is rapidly expanding the number of high field imaging protocols. This means that there is a need to assess the differences between various acquisition types in order to compile and compare data that has been collected over a period of time which technology is continually evolving. Our goal in this study was to quantitatively assess the quality of DSC-MRI data by comparing various 3T protocols with the conventional quadrature coil 1.5T acquisition. By evaluating image SNR and dynamic SNR of the $\Delta R2^*$ curve between field strengths, quadrature versus multi-channel coil arrays, and partially parallel acquisitions, in addition to characterizing the amount of distortion between the standard EPI acquisition and SENSE, we were able to gain insight as to the benefits and limitations in selecting the appropriate acquisition scheme.

Compared to the standard 1.5T acquisition, our results demonstrated improved dynamic and image SNR with field strength and increased number of coils. The addition of SENSE only slightly reduced dynamic and image SNR. Similar trends in

SNR were observed within all brain regions studied. The discrepancy between the peak location of the histogram and mean dynamic SNR values from NABT and NAWM is probably due to the fact that there are several regions within the brain from which dynamic SNR cannot be accurately estimated, due to necrotic tissue, lack of vessels, or susceptibility artifacts, thereby shifting the location of the histogram peak from the whole brain to a much lower value. As a result, the mean values within regions where vasculature is well-characterized are a more accurate measure. The normal-appearing brain tissue region yielded slightly higher dynamic SNR values compared to those obtained from the normal-appearing white matter region because it included some gray matter, which is known to produce two to three times as much signal change.

Our results consistently showed an increase in dynamic and image SNR from 1.5T to 3T that is greater than what would be expected based upon the difference in field strength alone, even though both groups utilized a standard quadrature head coil. We corrected for the variation in slice thickness between 1.5T and 3T data in our SNR calculations and all other acquisition factors affecting SNR, such as echo time and in-plane resolution, were kept constant. Thus, the additional SNR improvement that we observed may be attributed to differences in relaxation times or to enhanced performance of the radiofrequency coil used.

Although the linear relationship between field strength and SNR has been well established in both anatomic and functional imaging paradigms (73,77), the SNR changes with the addition of coil array elements remains an arduous task to characterize. From a statistical point of view assuming normally distributed uncorrelated noise, repeated measurements of the same voxel should increase SNR by \sqrt{N} , where N is the number of coil elements. However, coil views are not

necessarily independent measurements and the method by which the data from each channel is combined influences the SNR of a given voxel. In addition, the size of coil element plays an important role, with a smaller coil radius resulting in an increase in SNR approximating $r^{-5/2}$ (86), while the distance away from the coil yields a reduction in SNR as a function of $1/d^3$. The coil array used in this study was of a dome shape, consisting of eight coils that encircle the anterior, posterior, left, and right sides of the head and merge superiorly at the crown. This coil configuration complicates theoretical SNR calculation even further by producing a spatially varying SNR distribution in the S/I direction. Most of our patients had supratentorial tumors spanning similar S/I locations and susceptibility artifacts limited the extent of the acquired inferior margin. Nonetheless, some of the variation observed within the 8-channel coil data, could be attributed to the fact that several patients with higher image and dynamic SNR possessed tumors located superiorly in the brain so that the prescribed slice coverage was closer to where the coils converged.

A partially parallel acquisition confounds SNR measurements even further. For SENSE reconstruction with a reduction factor of two, there should be a $g\sqrt{2}$ reduction in SNR, where g is the geometry factor for a particular voxel imaged with a certain coil configuration and can be calculated from knowledge of the coil sensitivity profiles and unfolding matrix (78,81). Since g is greater than or equal to one, we expect at best a 30% decrease in SNR for the SENSE acquisition, whereas only around 20% reductions were observed. This result suggests that either the shift in the acquisition window along the $T2^*$ curve decay curve due to SENSE provides additional SNR, or a sum of squares combination of coil elements may not represent the optimal SNR for the fully-encoded case.

The effects of T1 relaxation on dynamic SNR were also considered through examination of the post-bolus $\Delta R2^*$ signal. Changes in the post-bolus signal within normal appearing white matter among all non-SENSE acquisitions were found to be consistent with the observed differences in dynamic SNR. As a result, both the ratio of the peak to post-bolus signal and percent recovery of the post-bolus signal from the peak did not vary significantly between acquisitions, indicating that the observed SNR differences were not confounded by changes in T1 relaxation. The post-bolus signal of the SENSE acquisition, however, was slightly higher relative to the peak of the first pass bolus signal compared to the other groups. This apparent decrease in T1 effects could be the result of altering the relative T1 and T2* contributions from earlier sampling of the T2* decay curve inherent with SENSE. Further investigation to determine the impact of this effect on the quantification of leakage measurements within tumor regions with a compromised BBB is necessary for the accurate planning of treatment strategies.

The implementation of SENSE EPI compared to the standard 3T EPI acquisition with an 8-channel coil resulted in decreased geometric distortion and reduced signal dropout. The displacement maps of both acquisitions had the same spatial patterns describing the distortion; only the magnitude of the displacement was elevated for the standard acquisition. Although SENSE EPI was able to reduce the effects of magnetic susceptibility-induced artifacts throughout the image volume, there was no region of the brain where all distortion was completely removed by SENSE. Distortion is expected to occur mostly in the phase encode direction due to the smaller bandwidth in that direction. Both the A/P distortion maps shown in Figure 5.7b and the displacement histograms in Figure 5.8b support this fact, with the negative intensities in the anterior and posterior regions of the maps and elongated

tail of the negative end of the histogram indicating a large voxel shift towards the anterior direction. As expected, SENSE EPI was able to significantly reduce the magnitude of these distortions as shown by the reduction in mean and median displacement distances, lower 95th percentile values of displacement histograms, and regression line slopes of greater than one. The displacements that indicated compression and expansion of the image in the readout direction were unaffected by the SENSE acquisition, which only reduced the bandwidth in the phase encode direction. Our results were able to both quantitatively confirm these observations and validate the inclusion of a partially parallel acquisition with SENSE reconstruction at 3T.

There are several factors affecting the accuracy of our distortion and signal dropout estimates. As with SNR, the location of slice prescription also influences the amount of both distortion and signal dropout present. Greater reductions in signal dropout from the SENSE EPI acquisition occurred in patients with more inferior tumors, which required coverage of the orbits whose interface with surrounding tissue produces a sizeable susceptibility gradient and results in more signal dropout with even larger voxel displacements. The accuracy of the method used to quantify distortion is also limited by the accuracy of the image registration, even though there was no significant correlation between the initial distortion and the accuracy of the image registration for these data.

Manka et al have shown that the gain in dynamic SNR at 3T compared to 1.5T using a quadrature head coil can translate to halving the dose of contrast agent injected (87). We have the added benefit of increased SNR due to the multi-coil array, and so could potentially simultaneously reduce the patient dose and still be more sensitive to smaller signal changes. In the same study, a Principles of Echo

Shifting using a Train of Observations (PRESTO) sequence was used to reduce the effects of susceptibility artifacts that we saw with increasing field. However, quantitative analysis was not utilized to assess the performance of this technique. Application of a PRESTO SENSE sequence to 3T DSC MRI perfusion studies as Golay et al did for blood-oxygen-level-dependent (BOLD) imaging (88) would perhaps reduce these artifacts even further. With the decrease in dose, additional assessment can be done within the same patient exam to directly compare how a parallel acquisition affects computed rCBV values as well as other parameter estimates.

In conclusion, our results have shown that DSC MRI is a feasible technique at 3T, especially with the implementation of a multi-channel coil array and partially parallel acquisition. The gain in SNR with higher field strength magnets and multi-channel coil arrays manifests in greater sensitivity to smaller signal changes, which is expected to improve quantitation of perfusion-derived parameters that often rely on complex fitting routines in their estimates and also facilitating higher resolution maps for better tumor delineation. In addition to improved image and dynamic SNR, 3T SENSE EPI allows a 1.4-fold increase in slice coverage. Although alignment of the dynamic data to anatomical images remains a challenge due to the magnetic susceptibility-induced artifacts inherent with this technique, application of echo shifting acquisition methods and/or post-processing non-rigid registration routines in conjunction with SENSE EPI is a viable option.

Chapter 6: Extension of Parallel Imaging Techniques for Susceptibility-Weighted Imaging at Higher Fields (3T and 7T)

As even higher field MR systems with multi-channel coil capabilities become available for routine clinical use, the traditional techniques for measuring relative cerebral blood volume in brain tumors described in previous chapters become a challenge due to increased B_0 inhomogeneity and magnetic susceptibility differences at air-tissue interfaces that lead to signal drop out and large geometric distortions in echo planar imaging. An alternative approach is to take advantage of the increased susceptibility effects and apply the phase information contained in conventional gradient-echo sequences to create high resolution susceptibility-weighted venograms. This chapter focuses on developing an imaging protocol for susceptibility-weighted imaging at high field (3T and 7T) utilizing partially parallel imaging with SENSE reconstruction to minimize scan time, but retains heightened large vessel contrast, sensitivity to small vessel detection, image uniformity, and maximum coverage.

6.1 Background

Blood Vessel Imaging Based on Susceptibility

Susceptibility weighted imaging (SWI) is an emergent technique for high resolution, distortion-free imaging of brain vasculature that is recently gaining importance in the clinical setting. The technique utilizes phase data to enhance contrast between tissues with different susceptibilities, typically requiring long echo times to obtain sufficient weighting (89). Several tissues have unique magnetic

susceptibility differences relative to brain parenchyma whose contrast can be manipulated to become sensitive to this effect. These include paramagnetic blood clots, diamagnetic calcification, iron-laden tissue, air-tissue interfaces, and venous vasculature. Phase-sensitive imaging has recently been shown to improve the diagnosis of brain neoplasms, neurological trauma, and vascular malformations, in addition to a variety of cerebrovascular and neurodegenerative diseases (90).

Hemoglobin is the primary oxygen carrier in the blood and is composed of four protein subunits that can be either oxygenated or deoxygenated. The structure of each heme group is comprised of an iron atom (Fe^{+2}), that is capable of binding with oxygen and surrounded by a porphyrin ring. In arterial blood, oxygen is bound to the iron atom and there are no unpaired electrons; oxyhemoglobin is diamagnetic, with magnetic susceptibility less than one. Once the oxygen molecules dissociate from the iron atom in the capillary beds, a conformational change prevents the adjacent water molecules from binding to the remaining unpaired electrons and forms deoxyhemoglobin, a paramagnetic compound with high magnetic susceptibility. Thus, depending on the oxygen saturation, blood can be either more diamagnetic or paramagnetic compared to surrounding tissue. This creates local susceptibility differences that lead to signal dephasing and spatial variations in phase. (91,92)

Two effects arise from magnetic field inhomogeneity due to paramagnetic, deoxygenated venous blood: 1) T_2^* shortening of the magnitude signal, and 2) phase differences between the venous blood and surrounding brain parenchyma. Both phenomena depend upon the amount of oxygen saturation and result in signal loss. The first effect ensues because the T_1 and T_2 properties of blood are dependent on oxygen saturation. As a result, imaging at long echo times can maximize the difference in contrast between arteries and veins, making

deoxyhemoglobin an endogenous contrast agent for the visualization of venous structures. Bulk magnetic susceptibility within the venous vessels is responsible for the second effect, where an average frequency shift occurs for all protons inside the vessel, leading to phase differences between the veins and their surroundings. Since the phase difference varies periodically as a function of echo time, an optimal TE can be chosen to exploit the signal cancellation from these partial volume effects.

Just as was demonstrated in T2* EPI methods for perfusion imaging in Chapter 3, a bicompartamental model can also be applied to describe the mechanism that allows the visualization of venous structures in SWI. The variation in induced field strength (ΔB), for a vessel modeled as an infinitely long, straight cylinder oriented at an arbitrary angle (θ), to the static magnetic field (B_0), is given by Equation 6.1,

$$\Delta B = 2\pi \cdot \chi_{do} B_0 \cdot (\cos^2\theta - \frac{1}{3}) \cdot (1-Y) \cdot Hct \quad (6.1)$$

where χ_{do} is the susceptibility difference between fully deoxygenated and fully oxygenated blood, Y is the degree of oxygen saturation of hemoglobin, and Hct is the average volume fraction of hematocrit in blood. Equation 6.2 describes how this change in local field strength affects the phase angle of the venous blood signal (Φ), highlighting the dependence of phase differences on echo time.

$$\Phi = -\gamma \cdot \Delta B \cdot TE \quad (6.2)$$

Based on these equations, maximum signal cancellation results from a vessel residing parallel to the magnetic field ($\theta=0$). However, since signal dropout also relies on the fraction of signal (not only the orientation and volume fraction) from each component, the same reduction of signal can be achieved as long as the venous signal fraction is at least 50% of the entire voxel signal. As a result, even small, sub-voxel size vessels can be detected.

In order to achieve sufficient susceptibility contrast from vessels while simultaneously minimizing contrast among gray matter, white matter, and ventricles, long echo and repetition times are required. Although the echo time needed to visualize the large phase changes in venous vessels due to the magnetic susceptibility differences between oxygenated and deoxygenated blood is reduced with increasing field strength, long repetition times are still compulsory to avoid T1-weighting. Thus, the need for developing methods to shorten the acquisition time for SWI becomes apparent especially at 7T.

Application of SENSE to SWI

The previous chapter implemented SENSE to reduce susceptibility artifacts inherent in EPI and traded the reduction in sampled phase encode lines for increased coverage. In this chapter, we perform SENSE with SWI in order to reduce lengthy scan times so that high resolution images (sub-millimeter) can be obtained within a scan time that is feasible to add to clinical protocols. Since long repetition times are needed to avoid T1-weighting, the total acquisition time for SWI remains long (>10 minutes for only a 2 cm slab of tissue at 7T) even though the echo time is reduced. This can result in patient discomfort and motion induced artifacts. Thus, the need for faster acquisition times and efficient ways of combining multi-channel coil data without losing the phase information as a result of the reconstruction becomes apparent. Partially parallel imaging (PPI) acquisitions and reconstruction algorithms can be employed to speed up these long acquisition times as long as the concomitant decrease in SNR does not significantly affect the contrast between vessels and brain parenchyma.

The feasibility of PPI techniques has been proposed in the literature for accelerating SWI acquisitions at 1.5T. Sedlacik et al. initially simulated elliptical and GRAPPA k-space undersampling and reconstruction regimes with factor of two reductions for SWI and found reduced contrast of small vessels compared the fully sampled case (93). Both the gain in SNR and increased susceptibility contrast achievable at higher field strengths should facilitate the implementation of PPI techniques for SWI. The goal of this chapter is to develop an imaging protocol for susceptibility-weighted imaging at high field systems (3T and 7T) that minimizes scan time, but retains heightened large vessel contrast, sensitivity to small vessel detection, image uniformity, and maximum coverage.

6.2 Methods

Data acquisition

Nine healthy volunteers were scanned on both a 3T GE Signa Echospeed system equipped with an EXCITE platform and 7T GE Signa scanner (GE Healthcare Technologies, Milwaukee, WI). Eight-channel phased array head coils were used for signal reception at both field strengths (3T: MRI Devices, Gainesville, Florida; 7T: Nova Medical, Wilmington, MA). Uniform excitation was achieved using a body coil for the 3T and volume transmit coil at 7T. 3D flow compensated, SPGR and GRE sequences were acquired at both field strengths with the parameters listed in Table 6.1. The imaging protocol also included the acquisition of a low resolution, proton-density weighted, fast gradient echo sequence (TE/TR=2.1/150 ms, flip angle=20°, a 30 x 30 cm² FOV, 64 x 64 image matrix, and 3 mm slice thickness) for coil sensitivity estimation. An additional volunteer was scanned at 7T only with a

GRE sequence at four different echo times (8, 12, 16, and 20 ms). Informed consent was obtained from the volunteers prior to scanning.

Table 6.1: SWI scan parameters at 3T and 7T

Parameter	3T	7T
<i>TE/TR</i>	28/46 ms	16/80 ms
<i>Flip angle</i>	20°	20°
<i>FOV</i>	24 x 24 x 6 cm ³	24 x 24 x 2.8 cm ³
<i>Matrix size</i>	512 x 256 x 60	512 x 256 x 28
<i>Scan time</i>	12:47 min	10:59 min

SWI Post-Processing of Complex Multi-Channel Data

Each acquired k-space point from the digitized MR signal received from each coil consists of a real and imaginary component. After Fourier transforming the complex data into image space, either magnitude and/or phase images can be constructed. Conventionally, magnitude images are displayed by taking the square root of the sum of squares of the real and imaginary values from each voxel. Alternatively, several applications take advantage of the phase data as well, which can be extracted by taking the arctangent of the imaginary divided by the real signal. Examples of phase sensitive imaging include static field mapping, flow depiction, temperature mapping, and imaging susceptibility distortions.

The main objective behind the SWI post-processing of the T2* weighted images is to use the phase information of the complex signal to further reduce signal intensity from venous vessels. The first step in achieving this goal is to eliminate background field inhomogeneity effects present in the phase data, conventionally done using homodyne demodulation. The raw complex signal contains both background static field components in the central part of k-space and regions of rapidly varying phase transitions from local field inhomogeneities of deoxygenated

hemoglobin that reside in the outer portions of k-space. Thus, low pass filtering the complex data through multiplication with an $n \times n$ point windowing filter in k-space followed by complex division with the original complex k-space data and Fourier transforming it back to image space, effectively achieves a high-pass filtered complex image with the background field inhomogeneity removed. The phase of this filtered image is now of interest since it only contains high spatial frequency phase components, but without impeding phase wraps which conveniently cancel in the complex division. A 64×64 Hanning filter had been previously determined experimentally in the brain (89,92) to be able to remove the low frequency static field inhomogeneity and selectively enhance vessels, while minimizing the amount of high frequency noise which would inhibit the detection of small vessels in the final image.

The next step is to determine a way to effectively use the filtered phase data in conjunction with the original magnitude image. For T2* imaging with the TE selected for maximum signal dephasing, venous vessels already appear darker on magnitude images compared to surrounding brain parenchyma. Since it is only the negative phases that are of interest, a phase mask ($f(x)$) can be constructed according to Equation 6.3 to linearly map the negative phases to values between zero and one. Any positive phases would therefore be set equal to one and would not affect the image.

$$f(x) = (\varphi(x) + \pi)/\pi, \text{ for } \varphi < 0 \quad (6.3) \\ = 1, \text{ otherwise}$$

This negative phase mask can then be multiplied into the magnitude image to enhance contrast by weighting the magnitude signal from the venous vasculature by the scaled phase of a given voxel. The more times the phase mask is multiplied into the magnitude image the greater the susceptibility weighting, although too many

multiplications can lead to noise magnification, thereby inhibiting the detection of smaller vessels. Haacke et al experimentally determined that 3-5 multiplications are optimal for maximum contrast and SNR (89).

In this work, the complex data from all coils was transferred off-line to a Sun workstation and post-processing was performed using a Linux cluster and Matlab 6.5 software (MathWorks Inc., Natick, MA). For the conventional full FOV multi-channel acquisitions, phase masks were constructed from the raw complex data of each individual coil element through complex division by the low-pass filtered image to remove the effects of field inhomogeneity and scaling the resulting negative phase values between zero and one, as illustrated in Figure 6.1 and described above. The phase masks were then multiplied into the magnitude image from each coil four times. The resulting susceptibility-weighted images from each individual coil were combined by summing the images weighted by normalized coil sensitivity profiles obtained from the low resolution PD-weighted fGRE scan.

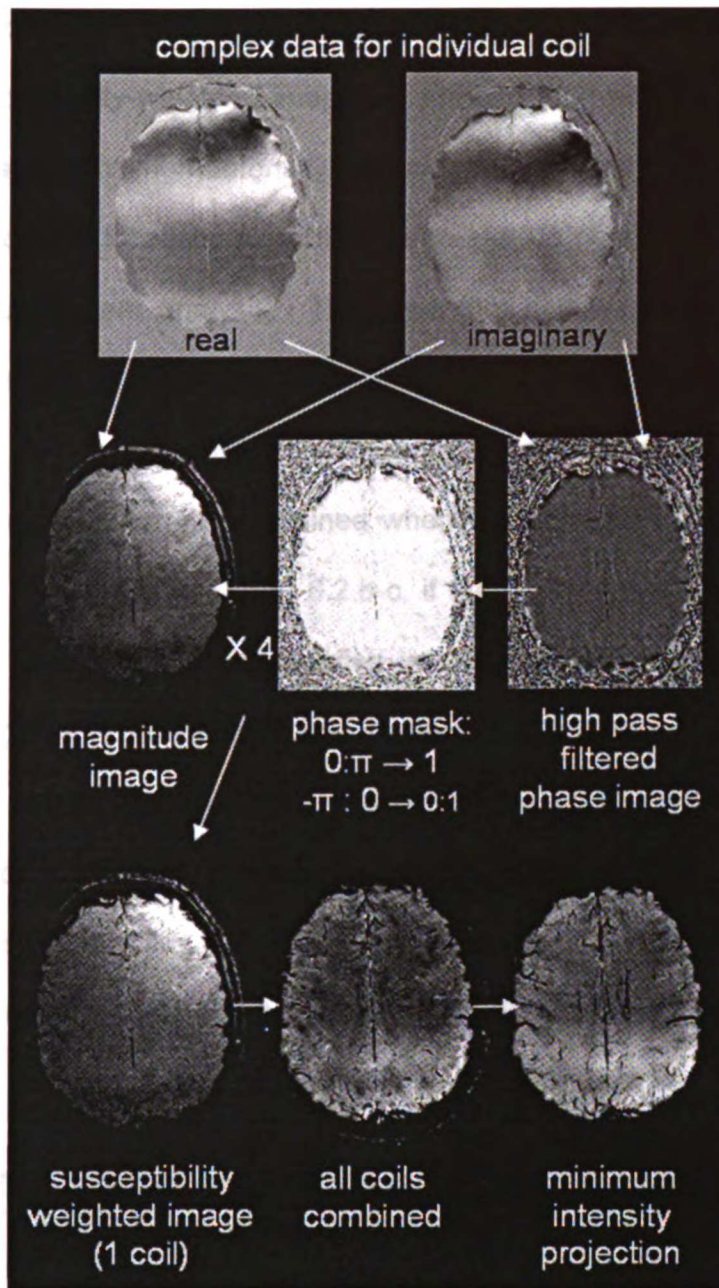


Figure 6.1: Depiction of processing steps involved in SWI

Low Pass Filter Coil Correction and Minimum Intensity Projection

Once the susceptibility weighting and coil combination were completed, two additional processing steps were performed to further improve the contrast between vessels and surrounding brain parenchyma and enhance overall image quality. A

low pass filter correction with edge completion algorithm (80) was first applied to the combined susceptibility-weighted images to remove any residual intensity variation across the image. Minimum intensity projections (mIPs) through 15mm thick slabs of similar anatomical locations were then generated to obtain the final SWI images used in the subsequent analysis. The maximum achievable contrast due to the susceptibility weighting, however, is dependent on the order in which low pass filter correction and mIP is executed. The best visualization of small vessel structures and highest image uniformity is attained when coil correction is done prior to mIP (Figure 6.2.a). As shown in Figure 6.2.b-c, if these processes are reversed (b), or coil correction is omitted (c), degradation in image quality is observed due to the darker shading from non-uniform coil combination interfering with small vessel contrast when minimally projected. Figure 6.2.d-e show coil corrected (d) and uncorrected (e) combined images before projection, further exemplifying the importance of coil correction in detecting small vessels. These observations have a considerable impact on vessel detection at 7T where field inhomogeneity and image uniformity is of greater concern compared to 3T acquisitions.

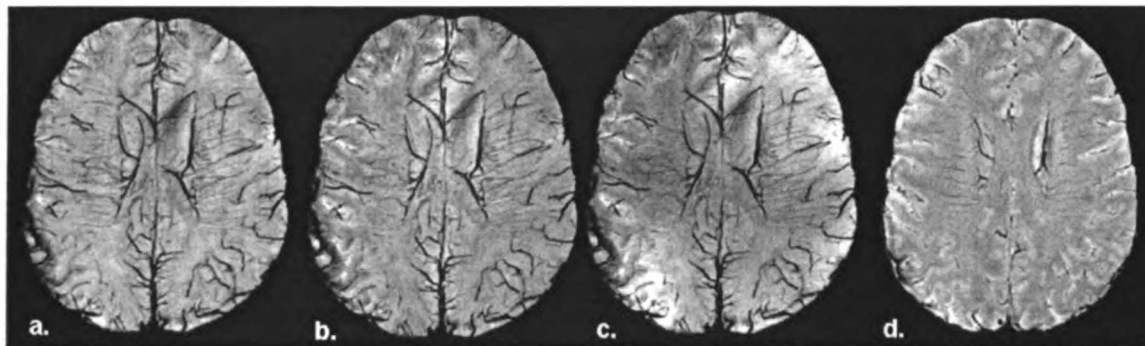


Figure 6.2: Importance of coil intensity correction and mIPs in small vessel detection at 7T

Implementation of SENSE Acquisition and Reconstruction for SWI

Although SENSE acquisition and reconstruction is a commercially available product for magnitude imaging with several fast imaging sequences such as fGRE and EPI on GE Excite scanners, the standard GRE sequence utilized in SWI had to be altered to acquire a reduced FOV dataset. The following modifications to the GRE pulse sequence were necessary in order to scan a fraction of the phase encode lines as shown in Figure 5.1 and obtain one complex raw data file.

1. Control variables to turn on SENSE and set the reduction factor while at the scanner were initialized in the pulse sequence code.
2. Appropriate buttons and pull-down menus were added to the scan display screen on the console.
3. The minimum allowable field of view was updated to permit acquisition of aliased images.
4. The number of frames or acquired phase encode lines was changed according to the reduction factor. This step subsequently required the phase resolution to be reset to the original number of frames in order to maintain the correct spacing between phase encode lines.
5. The maximum amplitude of the phase encode gradient to be played out was calculated based on the phase resolution instead of the number of acquired frames.
6. Within the core of the scan code, the phase encoding loop was updated to only load the appropriate phase encode waveforms to the data acquisition board on the scanner.

7. The executive recon control on the scanner was set to write out one large file containing all the raw complex k-space data from each coil for offline reconstruction and the product magnitude reconstruction was disabled.

In SENSE reconstruction, an aliased or reduced FOV image is first obtained for each coil array element. The construction of the combined full FOV image is based on the fact that each pixel in the reduced FOV includes the signal contributions from a number of positions in the full FOV. Separation of superimposed pixels is then achieved using the local coil sensitivities to determine different weights needed to unfold the signal superposition of each coil image.

In the analysis presented in this chapter, SENSE reconstruction with a reduction factor of 2 was simulated to generate complex reduced FOV images, prior to the changes enumerated above were actually modified in the pulse sequence. The complex coil sensitivity images for each coil element were upsampled to match the high resolution dataset and normalized by the combined coil sensitivity map to remove any additional weighting from the underlying brain anatomy. The unfolding of superimposed pixels was accomplished by direct inversion of an encoding matrix created from the sensitivity profiles. The combined full FOV complex image generated by the SENSE reconstruction was then Fourier transformed back into k-space to perform the susceptibility weighting. Low pass filter correction was performed on the combined magnitude image prior to phase mask multiplication and minimum intensity projections were then created after the weighting.

Data Analysis

Minimum intensity projections of the susceptibility weighted images were analyzed to determine four main regions from which to calculate vessel contrast, as demonstrated in Figure 6.3. Masks of large and small vessels and surrounding brain tissue were created by thresholding the SWI mIP images at varying degrees. Contrast ratios were calculated from the mean signal intensity within each brain mask divided by that of the corresponding vessel mask. The brain parenchyma region was used as the background tissue for the contrast ratio calculation of large vessels, while the sensitivity of detecting small vessels was evaluated using adjacent white matter as the background tissue. Histograms of voxels within the large brain mask were constructed to assess image uniformity and changes in signal intensity between acquisitions. To evaluate the performance of the SENSE reconstructions, contrast ratios of the under-sampled datasets were compared to the full FOV case for each field strength and sequence. Statistical significance was determined through the use of a Wilcoxon rank sum test. Only p-values < .01 were considered significant in order to correct for multiple comparisons.

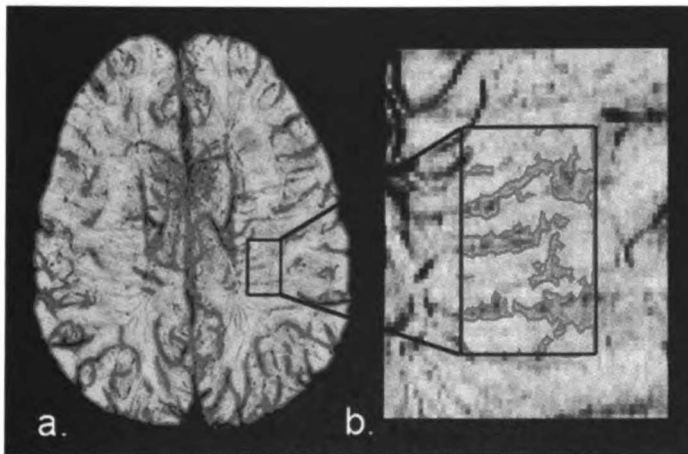


Figure 6.3: Depiction of brain regions used to generate contrast ratios for a) large vessels (green), surrounded by the whole brain region, and b) small vessels (pink), with neighboring white matter region.

6.3 Results

Optimization of SWI at 7T

As described in section 6.1, the echo time that maximizes the amount of signal contrast both due to changes in phase and T2* shortening can be determined for a given field strength using Equations 6.1 and 6.2, along with previously measured values for several constants. Substituting the values Weisskoff et al and Haacke et al measured in healthy volunteers for χ_{do} (0.18×10^{-6}), Y (0.54), and Hct (0.4) (94,95) and a maximum phase angle of π , Equations 6.1 and 6.2 can be reduced to Equation 6.3, where k is a constant (17.7) representing the product of all other terms.

$$TE = 1 / [k \cdot B_0 \cdot (\cos^2\theta - 1/3)] \quad (6.3)$$

Figure 6.4 demonstrates this relationship by plotting TE as a function of field strength for varying vessel orientations. Assuming an axial acquisition where the majority of vessels should be parallel to the field, this results in a TE of 28 ms for a 3T acquisition, whereas a 7T acquisition would in theory necessitate a 12 ms TE in order to achieve the most contrast between venous vessels and surrounding brain parenchyma.

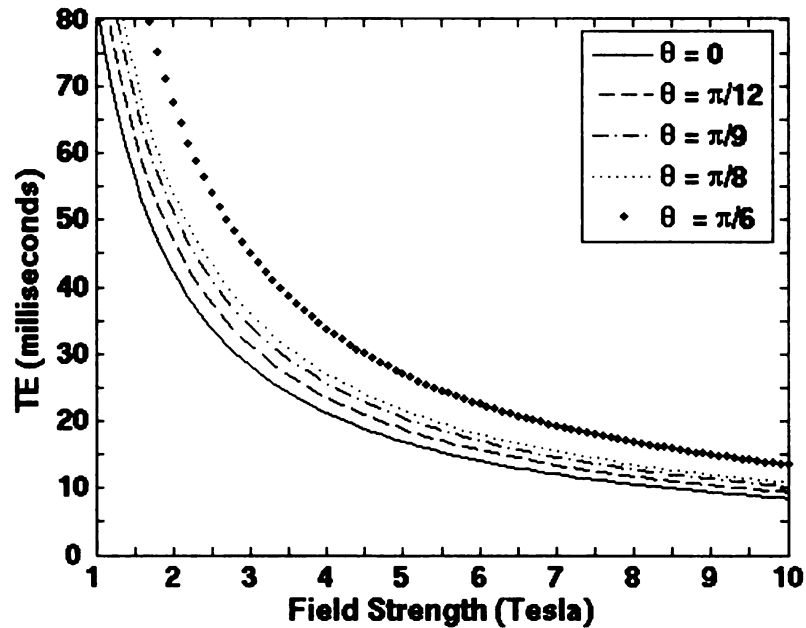


Figure 6.4: Echo time selection for maximum susceptibility weighting of venous vessels as a function of field strength

Although the optimal TE for visualization of phase differences in veins has been established empirically at 3T (92,96), the optimal TE must be verified at 7T. Utilizing the standard gradient echo, flow-compensated sequence, we tested four echo times (8, 12, 16, and 20 ms). Figure 6.5 illustrates the increase in contrast for both large and small veins observed with longer echo times at 7T. The heightened contrast of large vessels is more apparent between 8ms and 12ms TEs, while a TE of 16ms improves the visibility of small vessels. Larger phase distortions are visible at 20 ms due to increased susceptibility distortions that exist at 7T. As a result, a TE of 16 ms was selected for all subsequent 7T acquisitions described in this manuscript.

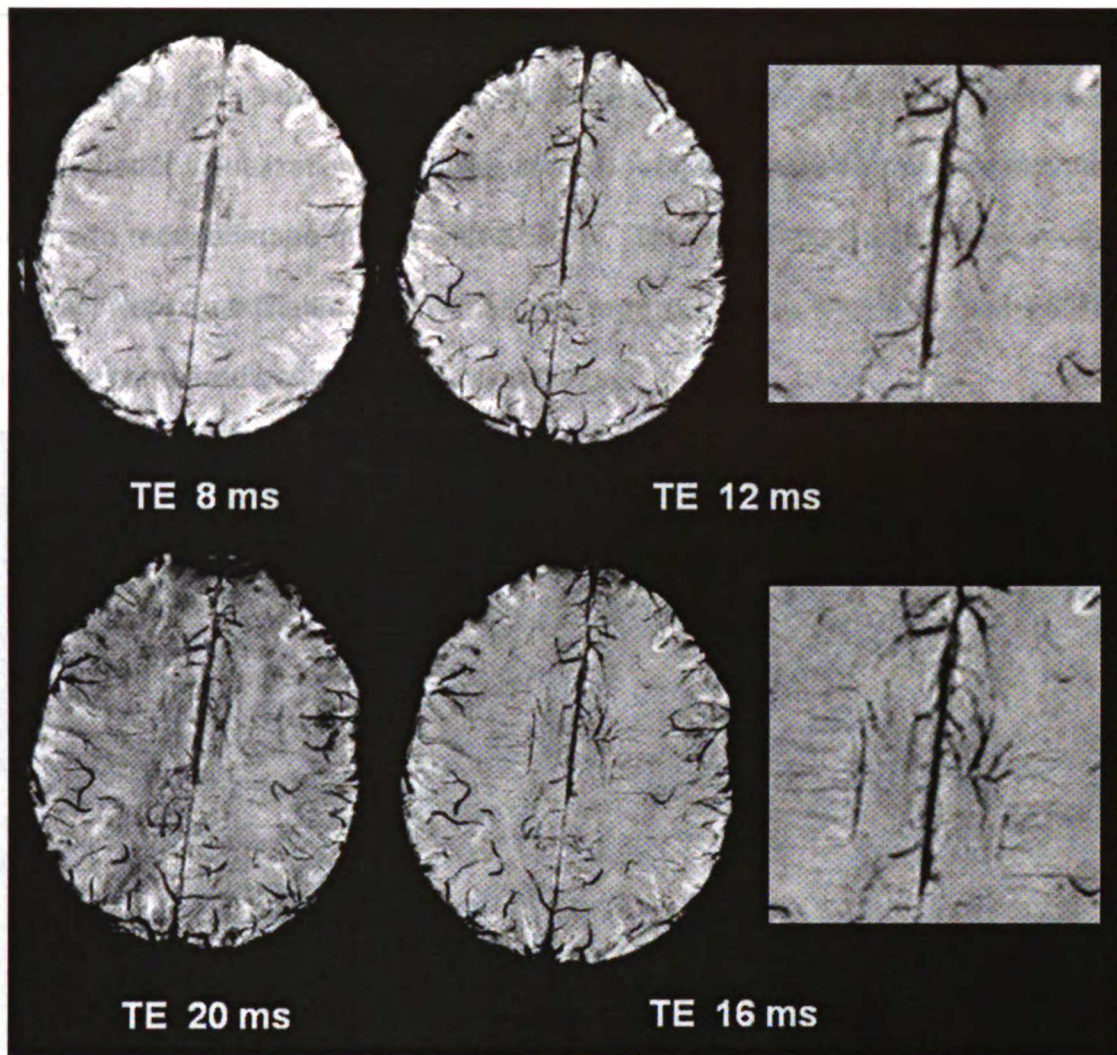


Figure 6.5: GRE SWI with mIP=15mm at 7T for different TEs, enlarged on right for TE=12 & 16 ms

Comparison of Large and Small Vessel Contrast

The final SWI images used for comparing vessel contrast among acquisition groups are depicted by Figure 6.6. Visual inspection of these images reveals heightened large and small vessel contrast at 7T compared to 3T and similar contrast between GRE and SPGR acquisitions. The improved contrast with field strength was due to a decrease in the intensity of vessels, while the background tissue appears similar based on the contrast parameters (TE/TR/flip angle) chosen.

There is no visible disparity amongst the four acquisition schemes displayed in Figure 6.6 at 3T; however at 7T, the SPGR sequence appears to demonstrate slightly better visualization of smaller vessels, and the presence of increased noise seems to reduce image quality with SENSE. These observed differences in vessel contrast were quantified for both small and large vessels as shown in Tables 6.2 and 6.3, and compared between acquisition types.

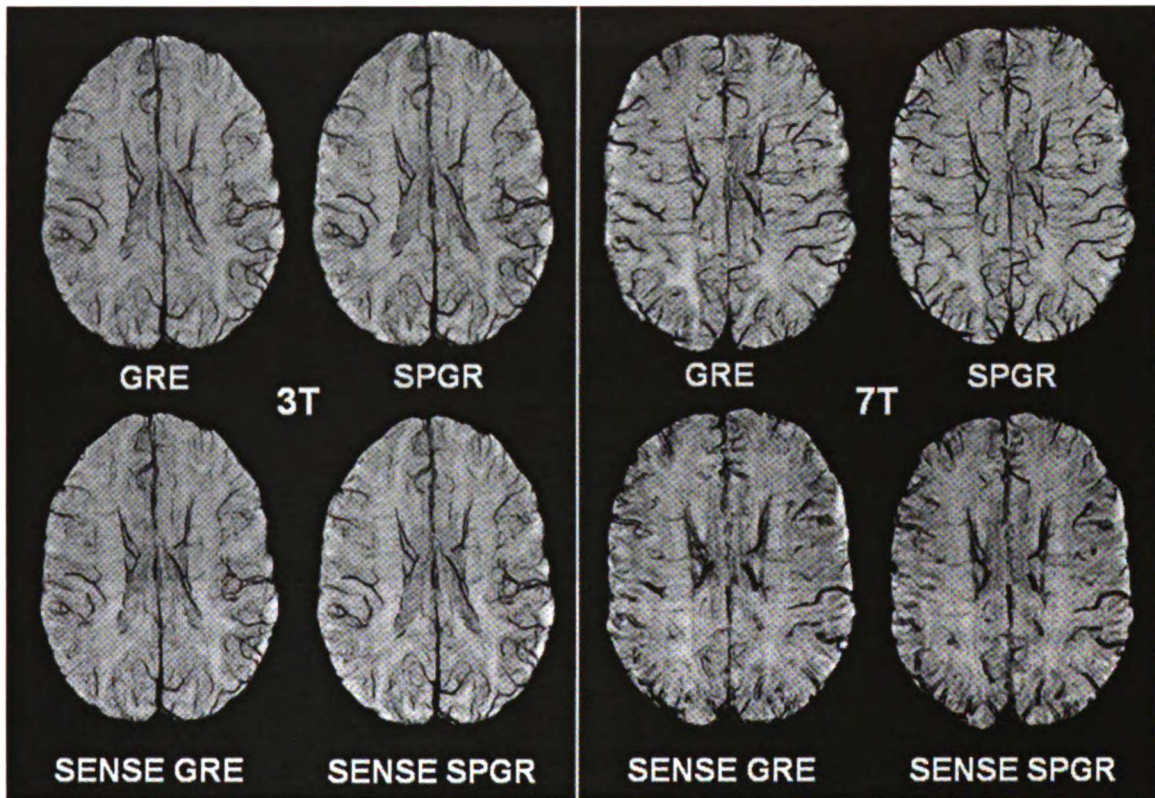


Figure 6.6: Final SWI images for each acquisition at 3T (left) and 7T (right) for the same volunteer

Table 6.2: Mean large and small vessel contrast for each acquisition at 3T and 7T

3T	Full FOV		SENSE, R=2	
	GRE	SPGR	GRE	SPGR
<i>large vessel contrast</i>	3.00 ± .33	3.01 ± .44	2.85 ± .36	2.81 ± .43
<i>small vessel contrast</i>	1.16 ± .05	1.18 ± .06	1.13 ± .07	1.16 ± .08
7T				
<i>large vessel contrast</i>	4.0 ± .88	4.27 ± .74	1.91 ± .19	1.95 ± .15
<i>small vessel contrast</i>	1.35 ± .05	1.37 ± .06	1.07 ± .03	1.06 ± .03

As expected, the greatest differences in contrast ratios were observed with field strength. A 1.34 and 1.42 – fold increase in large vessel contrast was observed for GRE ($P < .003$) and SPGR ($P < .001$) at 7T compared to 3T. Small vessel contrast was also elevated 1.2 – fold for both GRE and SPGR ($P < .0001$). Figure 6.7 demonstrates the heightened detection of small vessels at 7T with an SPGR acquisition.

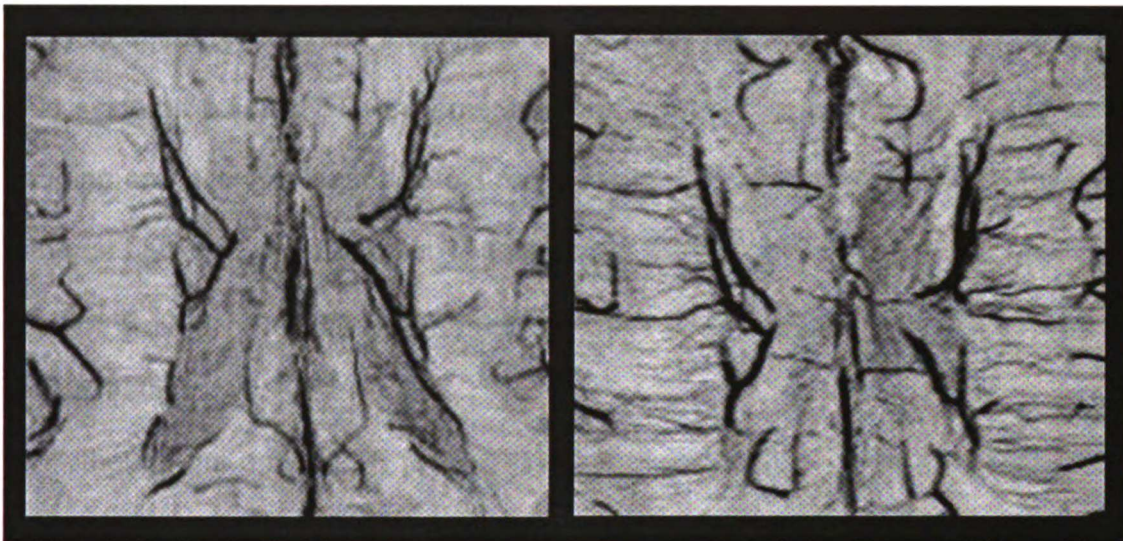


Figure 6.7: SPGR SWI images at 3T (left) and 7T (right), enlarged to view small vessels

No difference was found in large vessel contrast between GRE and SPGR sequences at 3T (3.0 mean contrast, $P = .9$), and only a 1.8% increase was observed in small vessel contrast for the SPGR sequence ($P = .5$). At 7T, the SPGR sequence showed a 5.5% increase in large vessel contrast ($P = .3$), but only a 1.4% elevation in small vessel contrast ($P = .5$) compared to the GRE sequence.

The addition of SENSE showed minimal effect in small and large vessel contrast at 3T, but lowered vessel contrast at 7T. There was a 5.5% and 6.3% reduction in large vessel contrast for GRE and SPGR sequences respectively at 3T, with only

2.7% and 1.9% decreases were observed in small vessel contrast, but none of these trends were significant ($P \geq .2$). At 7T, small vessel contrast decreased by 21-23%, while large vessel contrast was reduced by 52-54% from the addition of SENSE ($P < .00001$).

6.4 Discussion and Conclusions

Susceptibility-weighted imaging is a promising high resolution technique for high field systems beyond 3T. Implementation of a multi-channel coil array and parallel imaging can allow at least a 2-fold reduction in scan time without compromising the contrast between veins and surrounding brain tissue, which is especially attractive at 7T where long repetition times would prevent SWI from being routinely used in a clinical setting.

Although the optimal TE for visualization of phase differences in veins had been established empirically at 3T, the TE needed to first be confirmed experimentally, before comparing vessel contrast among acquisitions. Figure 6.5 demonstrated this relationship between TE and field strength for varying vessel orientations. An axial acquisition where the majority of vessels should be parallel to the field would result in a TE of 12 ms for a 7T acquisition. However, experimentally we found that a 16 ms TE achieved the best vessel contrast without creating large phase changes that would introduce excessive phase wrapping. This slightly higher than expected echo time may be attributed to the fact that many smaller vessels that are not detected at lower field strengths are actually oriented at a different angles to the main magnetic field. The fact that the other constants used in Equations 6.1 and 6.2 were

measured at lower field strengths may also lead to an underestimation in optimal echo time.

In comparison to the 3T acquisitions, the 7T scans exhibited elevated large and small vessel contrast for both standard GRE and SPGR sequences. This increase in contrast was expected due to both the heightened susceptibility difference between deoxygenated and oxygenated hemoglobin and rise in static field strength. As a result, it follows that the enhanced contrast observed with higher field strength was due to a decrease in the intensity of vessels, while the background brain tissue appeared similar due to the contrast parameters (TE/TR/flip angle) selected. Visual inspection of the images exhibited in Figure 6.7 also showed an elevation in the number of small vessels present, especially within the white matter. This phenomenon can be explained by a greater number of voxels experiencing an increased fraction of signal due to vessels, thereby amplifying partial volume effects with surrounding brain parenchyma. These results advocate that 7T is highly beneficial for improved detection of small vessels that are not visible at lower field strengths, although long scan times are still a concern.

The differences in contrast observed between GRE and SPGR sequences were far more subtle than the changes detected with field strength. At 3T, no difference was found in large vessel contrast between GRE and SPGR sequences, but trends toward heightened small vessel contrast for the SPGR sequence were observed. Using an SPGR sequence at 7T, however, showed trends towards increased large and small vessel contrast, possibly suggesting that an SPGR sequence may be a more optimal than the conventionally used GRE at higher field strengths, where spoiling of residual magnetization has a greater effect.

The addition of SENSE does not affect small and large vessel contrast at 3T, but significantly reduces vessel contrast at 7T. The fact that SENSE showed less contrast in small vessels was surprising based on the results at 3T that showed no difference in small vessel detection between SENSE and the full FOV acquisition. This decreased contrast may be due to imperfect estimation of coil sensitivity maps. The arrangement and quality of the receive coil elements of the 8-channel coil at 7T were not necessarily optimized for SENSE. Further evaluation of coil sensitivity profiles and geometry factor maps is necessary to confirm the accuracy of the contrast observed with the SENSE reconstruction. This indicates that SENSE with $R=2$ may be useful at 3T, but further investigation is required to understand the decrease in contrast found when SENSE was simulated at 7T.

In conclusion, susceptibility-weighted imaging is an especially attractive tool for high resolution imaging of brain vasculature, for high field systems beyond 3T. In this chapter we showed the feasibility of accelerating SWI acquisitions two-fold by implementing a multi-channel coil array and parallel imaging with SENSE reconstruction. At 3T SENSE allowed at least a 2-fold reduction in scan time without compromising the contrast between veins and surrounding brain tissue. The increased susceptibility at 7T provided heightened vessel contrast. SPGR should be considered as a practical alternative to GRE sequences, especially at 7T. Alternative methods such as GRAPPA need to be investigated to reduce long scan times at 7T. Future work will explore various reduction factors to determine the acceleration limit for partially parallel imaging techniques on maintaining the same level of sensitivity to small vessel detection.

Chapter 7: Imaging Blood Vessel Volume at 3T using Susceptibility-Weighted Imaging and Dynamic Susceptibility-Contrast Perfusion MRI

Traditional techniques that utilize echo planar imaging to measure cerebral blood volume in brain tumors have been shown in previous chapters to be a challenge at high field. Chapter 6 showed how the heightened susceptibility effects inherent at high field strengths can be exploited using the phase information contained in conventional gradient-echo sequences to create high resolution susceptibility-weighted venograms. The goal of this chapter is to develop a method to assess vessel density from susceptibility-weighted imaging data and evaluate the potential of this technique at higher field strengths compared to dynamic susceptibility contrast perfusion MRI.

7.1 Method for Quantification of Vessel Volume from SWI

Patient Population and MRI Protocol

T2*-weighted SWI and DSC MRI was performed on thirteen high-grade glioma patients (six grade III anaplastic astrocytoma and seven grade IV glioblastoma), all of whom had received prior treatment. Images were acquired on a 3T Signa Echospeed scanner with EXCITE platform (GE Healthcare Technologies, Waukesha, WI), equipped with an 8-channel phased-array coil (Medical Devices, Gainesville, Florida). For the SWI acquisition, high resolution, T2*-weighted magnitude and phase images were obtained prior to the injection of any contrast agent using a 3D flow-compensated GRE sequence with TE/TR=28/46ms, 20° flip angle, 24x24x6 cm³ FOV, and 512x256x60 image matrix. The perfusion imaging

consisted of the injection of a bolus of 0.1 mmol/kg body weight of gadopentetate dimeglumine (Gd-DTPA) contrast agent at a rate of 5 mL/s. A series of 80 T2*-weighted gradient-echo, echo planar images were acquired during the first pass of the contrast agent bolus injection, with a TE/TR of 54/1500 ms, 35° flip angle, 26x26 cm² FOV, 128x128 acquisition matrix, and 4 mm slice thickness. Sensitivity encoding with a reduction factor of 2 was employed to both minimize the amount of distortion and allow a larger volume of coverage (13-14 slices) within the specified time resolution. Standard anatomical imaging included pre-contrast injection T1-weighted SPGR images to use as an intermediate in image registration and T2-weighted FLAIR images to segment the tumor lesion from normal brain tissue. A PD-weighted fGRE scan (150/2.1 ms [TR/TE], 50° flip angle, 64 x 64 x 35 matrix size, 30 x 30 x 17.5 cm FOV) was performed in order to estimate the coil sensitivity profiles needed for SENSE reconstruction of the echo planar perfusion images.

SWI Processing with Phase-Unwrapping

In the previous chapter the susceptibility weighting was performed using homodyne demodulation of the complex k-space data and taking the phase of the resulting image. Although useful in normal brain tissue not adjacent to air-tissue or air-bone interfaces, this method can leave residual phase wraps, or boundaries where the phase extends beyond $\pm \pi$ forms a discontinuity, in these regions and within tumors that can be mistaken for venous vessels. Alternatively, phase variations from static field inhomogeneities can be removed by first unwrapping the phase images and then taking the difference between the unwrapped phase image and a smoothed phase image (97) as described in Figure 7.1.

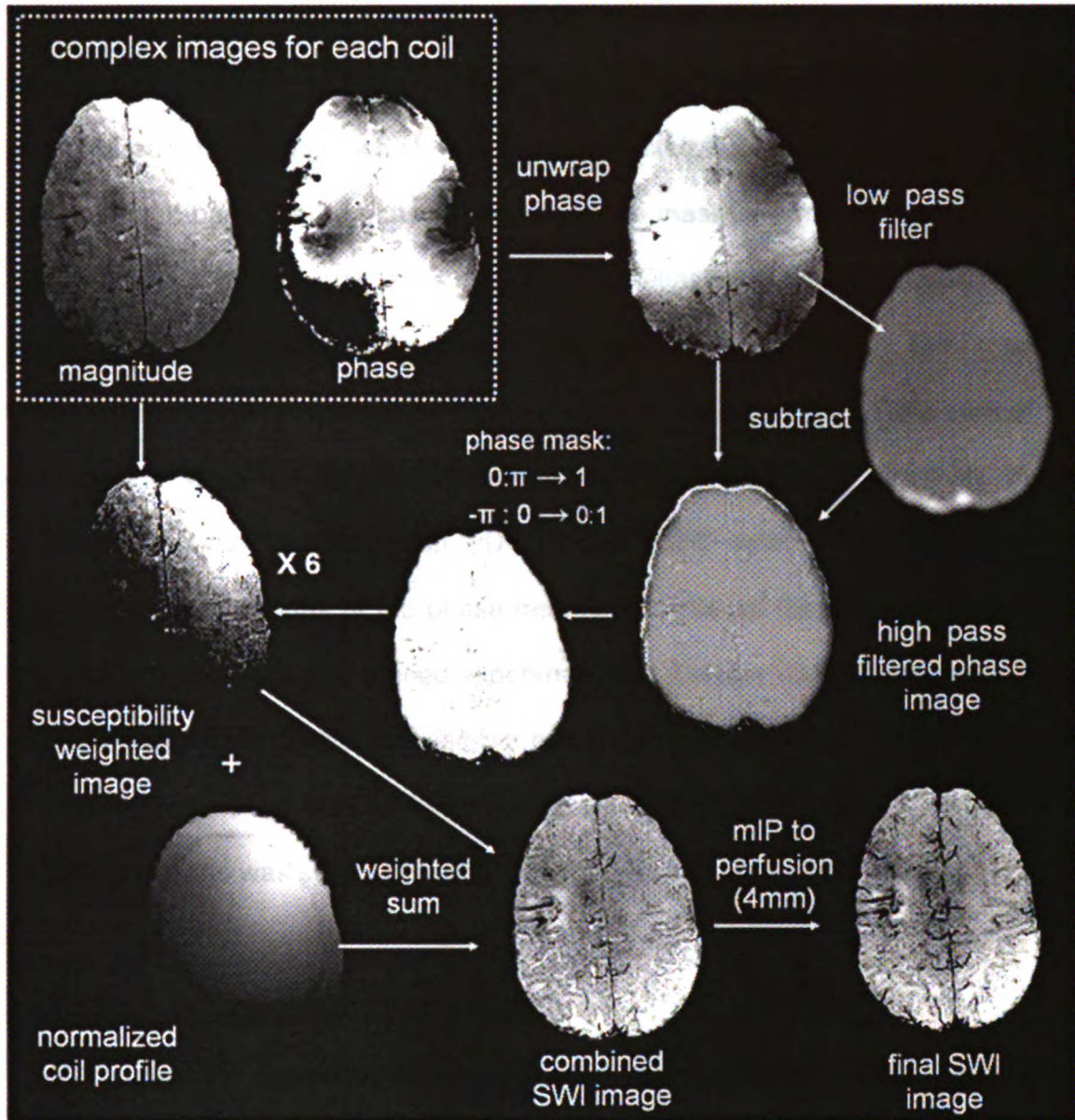


Figure 7.1: SWI post-processing steps with phase unwrapping and low pass filter subtraction for multi-channel coil combination

In this chapter, 2D phase unwrapping was performed on each slice of each individual coil image volume with PRELUDE software (FMRIB, Oxford, UK), a region-merging algorithm that optimizes a cost-function at boundaries (98). The resulting unwrapped phase image was further processed to replace isolated voxels where the phase unwrapping algorithm failed with phase values interpolated from

neighboring voxels, followed by dilation of the outer edges. A 12 x 12 box car mean filter was then applied to the processed unwrapped phase images to create a low pass filtered phase image, which was then subtracted from the original phase image to obtain high pass filtered phase images. Phase masks were constructed from the high frequency phase images as described in Chapter 6 and then multiplied six times into the magnitude image of the corresponding coil. The resulting susceptibility-weighted magnitude images were combined by taking the sum of the coil images weighted by the corresponding normalized coil sensitivity profile obtained from the low resolution PD-weighted fGRE scan. The filter size and number of multiplications of the phase mask that achieved the best vessel contrast and image quality was determined experimentally. Smaller filter widths and number of multiplications degraded the visibility of smaller vessels, where as larger values increased the noise in the final image. The combination of a 12 x 12 filter width and six multiplications was selected as the most optimal parameters for this study.

Perfusion Processing and Coregistration

EPI volumes were registered to the SWI images through rigid body transformations and non-rigid B-spline warping utilizing a pre-contrast, T1-weighted SPGR image as an intermediate distortion-free reference to co-register the images. [4] The volume of interest was restricted to the joint FOV of the SWI and co-registered echo planar images. Minimum intensity projections of the SWI images were created at the same slice thickness and coordinates of the perfusion imaging. rCBV was calculated from the $\Delta R2^*$ curve of the dynamic data using non-linear gamma-variate fitting to correct for leakage (99).

Data Analysis

SWI images were thresholded to generate masks of vessels and brain parenchyma. Tumor regions were defined by the T2 hyperintense lesion drawn on the FLAIR images. The fraction of SWI vessels in each low resolution perfusion voxel was computed and plotted against the rCBV value of that voxel for the whole brain, normal-appearing brain tissue, and tumor regions. Linear regression was performed to calculate the correlation between SWI vessel fraction and rCBV.

7.2 Comparison of DSC and SWI techniques

The locations of elevated blood volume based on rCBV calculations within both normal brain tissue and tumor corresponded to regions of decreased intensity on the SWI images (Figure 7.2), demonstrating how well the two techniques compare for a heterogeneous tumor lesion. Figure 7.2a depicts an edematous region of tumor clearly visible on the T2-FLAIR with minimal vascularity confirmed by both low rCBV values and the absence of vessels on the SWI image. In Figure 7.2b, elevated blood vessel volume is observed within the contrast enhancing portion of the tumor with both techniques. Figure 7.2c illustrates the formation of macronecrosis within a contrast enhancing rim region where DSC perfusion fails to capture the presence of vessels surrounding this lesion.

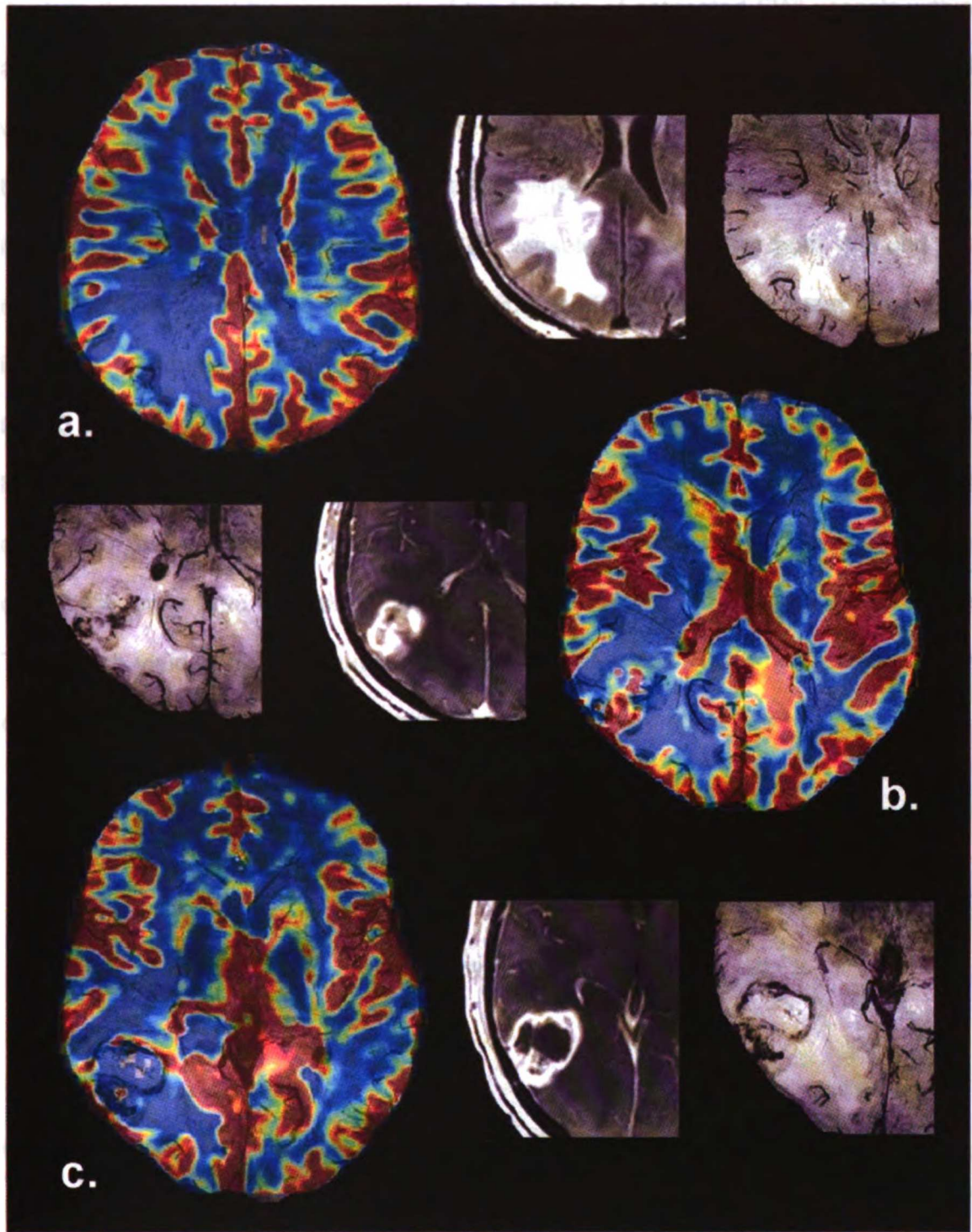


Figure 7.2: rCBV maps overlaid on SWI images (color), anatomic images (center), and original SWI images, for different slices (a-c) of a patient with GBM

Two-dimensional histogram plots of the fraction of estimated SWI vessels within an rCBV voxel plotted against the corresponding rCBV value within the same voxel were generated for each patient for the whole brain (WB), normal-appearing brain tissue (NB), and tumor (T2L). Figure 7.3 illustrates how cerebral blood volume increases with higher percentages of SWI vessels in a voxel for both WB and NB regions. This is confirmed by high correlation coefficients from the linear regression in that were significant in all but one patient for the normal brain region and for 11 of the 13 patients when looking at voxels in the entire brain (Table 7.1). Within the T2 lesion of the tumor, the reverse was found: only one patient showed a significant correlation between estimated rCBV values, even though the median r-value was only 2.4% lower than the normal and whole brain regions. The heterogeneity of the T2L, which yielded highly variable rCBV values, as well as the relative small number of data points, preclude any correlations between the two parameters.

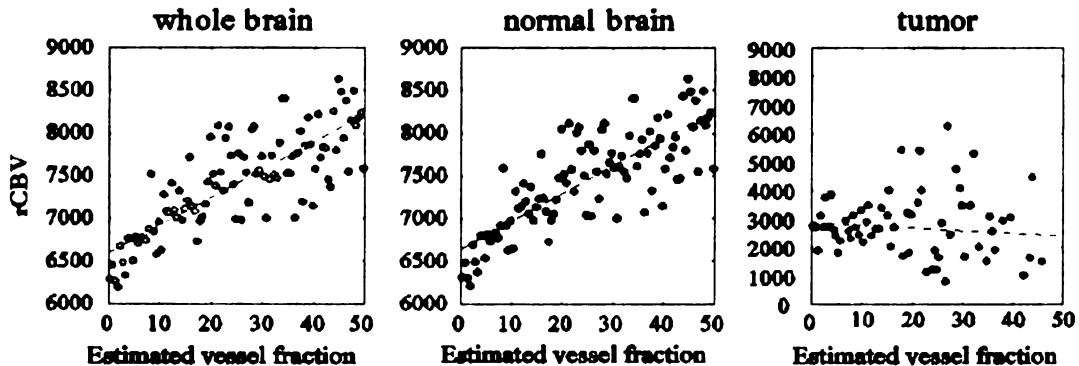


Figure 7.3: rCBV as a function of the fraction of vessels estimated from SWI within the whole brain, normal appearing brain tissue, and tumor for a grade 4 glioma patient

Table 7.1: Correlation results of rCBV with SWI vessel fraction

Region	WB	NB	T2L
median <i>r</i> value	.866	.866	.845
range of <i>r</i> values	.864-.866		.816-.864
# patients with significance*	11/13	12/13	1/13

**P* < .05 was considered significant

7.3 Discussion and Conclusions

This study demonstrates the feasibility of SWI as a technique to measure blood vessel volume in brain tumors, an advantage at higher field strengths where susceptibility contrast is heightened. Automated phase unwrapping with filtered phase subtraction was applied for the first time to a multi-channel dataset and a novel method was developed to assess vessel density from susceptibility-weighted images. The comparable results between techniques that were presented in this chapter clearly illustrated the potential of this SWI method for imaging brain tumor vasculature at higher field strengths (ie. 7T), where conventional methods to estimate cerebral blood volume at lower field strengths either pose an immense challenge or are currently not feasible due to technological limitations.

As previously shown by Rauscher et al and confirmed by our results displayed in Figure 7.2, the phase unwrapping with filtered phase subtraction method for SWI described in this chapter results in higher quality images where phase wraps that result from rapid changes in susceptibility at interfaces can be robustly removed. This is especially of interest in tumors where the conventional homodyne demodulation method described in Chapter 6 can often leave residual phase wraps in these regions due to heterogeneous tumor tissue, surgical resection cavities, biopsy locations, or the effects of novel treatments.

There are several factors affecting the accuracy of the susceptibility-weighting estimated by the method presented in this chapter. The performance of the susceptibility weighting procedure heavily relies on the robustness of the phase unwrapping routine. Regions of individual coil images that are located far from the coil element experience high frequency noise overlapping with the phase wraps that

creates discontinuities along the boundary of the wrap. In these areas it is difficult for the algorithm to fully unwrap the phase. The result is scattered voxels with undefined phase values that need to be estimated from neighboring voxels, which can potentially introduce errors in the phase mask calculation. The phase unwrapping algorithm implemented in this chapter was initially designed to unwrap the phase from low resolution field maps for geometric distortion correction of EPI-fMRI data. Our SWI datasets, however, are at least 4-8 times as large as the field mapping scans and the unwrapping must be performed individually for each coil. As a result, the 3D version of this phase unwrapping algorithm was rendered impractical for SWI data because it necessitated over ten hours of processing time on a lx24-amd64 Linux processor with 4 GB of RAM. Even when implementing the 2D phase unwrapping algorithm, an hour of computation was required as opposed to the twelve minutes of processing time needed for homodyne demodulation.

This study compares the percentage of SWI vessels that occupy a given EPI voxel to the rCBV value at that location. High correlations between parameters estimated from each technique in normal tissue and whole brain regions validate SWI as a method for quantifying blood vessel volume. Within the tumor region, however, no trend was observed between the two methods. Although the potential limitations of SWI are discussed above and in Chapter 6, we cannot necessarily attribute the poor correlations observed within the T2 hyperintensity of the tumors to errors inherent in SWI alone. As discussed in Chapters 3 and 5, DSC perfusion imaging suffers from numerous limitations that arise from both the echo planar data acquisition and post-processing of the T2* curves even at 1.5 T. Within the heterogeneous tumor region, these susceptibility-driven distortions are often exacerbated which can cause errors in alignment to undistorted, susceptibility-

weighted images even after non-rigid registration. In addition, rCBV may be overestimated in regions experiencing blood brain barrier breakdown, even though we attempted to correct for leakage by using a nonlinear gamma variate fitting algorithm to model and remove these effects. The vessel fraction index extracted from SWI, on the contrary, is not affected by leakage.

Another possible explanation for the variability observed between metrics could be the result of an inhomogeneous patient population with inherent heterogeneity within each tumor. The patients recruited for this study all received prior treatment, including sub or total gross resection plus the addition of radiation and/or chemotherapy. This patient population, along with the heterogeneity within the defined tumor region, could have adversely affected the correlation between parameters observed in this region. The bin size of the 2D histograms displayed in Figure 7.3 was selected in order to yield a reasonable number of data points in all regions. Subdividing the T2 lesion even further, based on the presence of contrast enhancement, necrosis, or metabolic abnormality, would help constrain the high variability of CBV values but was not possible with this method. Thus, the lack of correlation in the tumor region may also be attributed to the small number of samples with a larger range of values.

In conclusion, we developed a suitable index for estimating relative blood vessel volume from susceptibility-weighted images. SWI provides the added benefits of increased resolution, no geometric distortion, and does not require the injection of an intravascular contrast agent, but suffers from long scan times and is incapable of evaluating vascular integrity. Future work will use untreated patients with larger active tumor regions and evaluate metrics that can be used to quantify blood volume from susceptibility-weighted images that incorporate both the magnitude of signal

intensity change in regions of vessels compared to surrounding brain parenchyma and the volume of space that this depressed signal occupies.

Chapter 8: Summary

This thesis project has developed and implemented MRI acquisition, reconstruction, and post processing strategies to improve the characterization of microvasculature and tissue oxygenation within heterogeneous high-grade gliomas. Several MRI modalities including DSC perfusion MRI, SWI, and 3D MRSI were applied at different field strengths to achieve this goal. In addition, new parameters were introduced and partially parallel imaging methods were utilized to reduce image artifacts and scan time so that these techniques could be feasible in a clinical setting.

Dynamic susceptibility contrast perfusion imaging was performed on untreated high-grade glioma patients during the first pass and recirculation phase of a gadolinium bolus injection. Normalized peak height and percent recovery of the post-bolus signal were calculated on a voxel by voxel basis within the T2 and contrast-enhancing lesions and compared between grade III and grade IV patients. Grade IV gliomas exhibited significantly higher peak height values than grade III patients in regions of contrast enhancement. Enhancing grade III patients demonstrated less microvascular leakage within both regions compared to grade IV patients. Non-enhancing grade III gliomas exhibited less breakdown of the blood-brain-barrier compared to the non-enhancing portion of the edematous T2 lesion in grade IV patients. These results indicate that vascular transformations that precede the morphologic changes observed on conventional MRI methods are occurring. The improved specificity for characterization of the degree of angiogenesis and microvascular leakage in these tumors may be useful in evaluating response to treatment.

Since regions of abnormal perfusion were found outside the contrast enhancing volume in both grade III and grade IV gliomas, lactate-edited spectroscopic imaging was combined with perfusion imaging to investigate whether analysis of metabolite levels within regions of abnormal perfusion can assist in assessing levels of oxygenation. Grade IV gliomas exhibited significantly elevated choline in regions of heightened blood volume and leaky vessels, with decreased creatine and increased lactate only in regions of blood-brain-barrier breakdown, implicating reduced oxygenation in this area. Grade III gliomas showed trends towards increased creatine in locations of elevated blood volume and reduced levels where the blood-brain-barrier was compromised, suggesting the creatine may be an early marker of hypoxia. Thus, quantification of creatine and lactate levels within regions of leaky vasculature may be relevant for planning focal therapy and assessing response to treatment. Future studies should be performed to determine the prognostic value of these perfusion and metabolic parameters in predicting and evaluating tumor response to anti-angiogenic therapy for high-grade glioma patients.

The feasibility of DSC MRI at 3T was investigated by comparing image and dynamic signal-to-noise ratios of the $\Delta R2^*$ curve between 1.5T and 3T field strengths, a quadrature and 8-channel phased-array coil, and a conventional versus partially parallel echo planar imaging acquisition with SENSE reconstruction. The gain in SNR with higher field strength magnets and multi-channel coil arrays manifests in greater sensitivity to smaller signal changes, which is expected to improve quantitation of perfusion-derived parameters that often rely on complex fitting routines in their estimates and also facilitates higher resolution maps for better tumor delineation. In addition to improved image and dynamic SNR, 3T SENSE EPI allowed a 1.4-fold increase in slice coverage over the standard 1.5T acquisition. A

significant reduction in magnetic susceptibility induced artifacts was achieved with SENSE EPI compared to the standard EPI 8-channel coil acquisition at 3T, implicating SENSE EPI as a practical choice for clinical DSC MRI at 3T. Although alignment of the dynamic data to anatomical images still remains a challenge due to these artifacts inherent with this technique, application of echo shifting acquisition methods and/or post-processing non-rigid registration routines in conjunction with SENSE EPI is a viable option.

Susceptibility-weighted imaging has proved to be a promising technique for high field systems beyond 3T. Implementation of a multi-channel coil array and parallel imaging with SENSE reconstruction at 3T has allowed at least a 2-fold reduction in scan time without compromising the contrast between veins and surrounding brain tissue. The increased susceptibility at 7T provided heightened vessel contrast with improved sensitivity of detecting small vessels. Alternative parallel imaging methods such as GRAPPA will be considered in future studies to reduce long scan times at 7T where the implementation of SENSE reduced both large and small vessel contrast. Other possibilities are to explore higher reduction factors in order to determine the acceleration limit for these partially parallel imaging techniques on maintaining the same level of sensitivity to small vessel detection at both field strengths.

Finally, we have shown that SWI and DSC MRI could be combined to provide a more accurate assessment of tumor vascularity. SWI possesses the added benefits of increased resolution and no geometric distortion, but suffers from long scan times and is incapable of evaluating vascular integrity. Despite the increase in processing time, the phase unwrapping with filtered phase subtraction method for SWI resulted in higher quality images where phase wraps due to rapid changes in susceptibility at

interfaces were robustly removed. A suitable index for estimating relative blood vessel volume from susceptibility-weighted images was developed. The high correlations observed between parameters estimated from each technique in normal tissue and whole brain regions validated SWI as a method for quantifying blood vessel volume. Future studies will be conducted on untreated patients with larger active tumor regions and evaluate metrics that can be used to quantify blood volume from susceptibility-weighted images that incorporate both the magnitude of signal intensity change in regions of vessels compared to surrounding brain parenchyma and the volume of space that this depressed signal occupies.

While the clinical role of surrogate markers for the determination of abnormal vasculature still requires further evaluation, this work successfully demonstrates several methods that elucidate the utility of structural, functional, and metabolic indices in adding specificity to characterizing tumor heterogeneity and the spatial variations of abnormal vasculature. The existence of contrast enhancement on T1-weighted post-gad images has been shown to underestimate tumor burden prior to therapy. Utilizing undistorted maps of parameter indices generated from the MR techniques described in this thesis may be advantageous in treatment planning, including target definition for conformal beam radiation therapy and biopsy guidance to help avoid underestimation of the histologic grading of non-enhancing tumors. Predicting hypoxic regions would be especially advantageous in determining the most radioresistant regions of the tumor which may require additional therapeutic approaches in order to reconstruct the continued growth of tumor. Monitoring how both the magnitude and location of abnormal regions of such parameters change over time could also prove advantageous in characterizing whether new contrast enhancement is due to radiation effects or tumor recurrence. Although individually

these techniques are still currently limited in their ability to improve diagnostic accuracy in distinguishing grade III and grade IV gliomas, their potential in identifying more specific regions of vascular abnormality is still of great importance.

References

1. CBTRUS. Primary Brain Tumors in the United States Statistical Report, 1998-2002; Central Brain Tumor Registry of the United States; 2005-2006. 9-26
2. Nelson SJ, Vigneron DB, Dillon WP. Serial evaluation of patients with brain tumors using volume MRI and 3D 1H MRSI. *NMR Biomed* 1999;12(3):123-138.
3. Calamante F, Thomas DL, Pell GS, Wiersma J, Turner R. Measuring cerebral blood flow using magnetic resonance imaging techniques. *J Cereb Blood Flow Metab* 1999;19(7):701-735.
4. Cha S, Knopp EA, Johnson G, Wetzel SG, Litt AW, Zagzag D. Intracranial mass lesions: dynamic contrast-enhanced susceptibility-weighted echo-planar perfusion MR imaging. *Radiology* 2002;223(1):11-29.
5. Henry RG, Vigneron DB, Fischbein NJ, et al. Comparison of relative cerebral blood volume and proton spectroscopy in patients with treated gliomas. *AJNR Am J Neuroradiol* 2000;21(2):357-366.
6. Li X, Vigneron DB, Lupo JM, et al. Relationship between lactate, choline, creatine, and perfusion parameters in newly diagnosed high grade gliomas. 2004 May 12-17, 2004; Kyoto, Japan.
7. Dashner RA, Kangarlu A, Clark DL, RayChaudhury A, Chakeres DW. Limits of 8-Tesla magnetic resonance imaging spatial resolution of the deoxygenated cerebral microvasculature. *J Magn Reson Imaging* 2004;19(3):303-307.
8. de Zwart JA, van Gelderen P, Kellman P, Duyn JH. Application of sensitivity-encoded echo-planar imaging for blood oxygen level-dependent functional brain imaging. *Magn Reson Med* 2002;48(6):1011-1020.
9. Golay X, de Zwart JA, Ho YC, Sitoh YY. Parallel imaging techniques in functional MRI. *Top Magn Reson Imaging* 2004;15(4):255-265.
10. Preibisch C, Pilatus U, Bunke J, Hoogenraad F, Zanella F, Lanfermann H. Functional MRI using sensitivity-encoded echo planar imaging (SENSE-EPI). *Neuroimage* 2003;19(2 Pt 1):412-421.
11. Oncologychannel. Incidence and Prevalence.
from <http://www.oncologychannel.com/braincancer>.
12. Wrensch M, Minn Y, Chew T, Bondy M, Berger MS. Epidemiology of primary brain tumors: current concepts and review of the literature. *Neuro-oncol* 2002;4(4):278-299.

13. Bernstein M, Rutka J. Neuro-oncology fellowships in North America. *J Neurooncol* 1994;18(1):61-68.
14. Kleihues P, Burger PC, Scheithauer BW. The new WHO classification of brain tumours. *Brain Pathol* 1993;3(3):255-268.
15. Folkman J. The role of angiogenesis in tumor growth. *Semin Cancer Biol* 1992;3(2):65-71.
16. Amoroso A, Del Porto F, Di Monaco C, Manfredini P, Afeltra A. Vascular endothelial growth factor: a key mediator of neoangiogenesis. A review. *Eur Rev Med Pharmacol Sci* 1997;1(1-3):17-25.
17. Brat DJ, Van Meir EG. Glomeruloid microvascular proliferation orchestrated by VPF/VEGF: a new world of angiogenesis research. *Am J Pathol* 2001;158(3):789-796.
18. Damert A, Machein M, Breier G, et al. Up-regulation of vascular endothelial growth factor expression in a rat glioma is conferred by two distinct hypoxia-driven mechanisms. *Cancer Res* 1997;57(17):3860-3864.
19. Wesseling P, Ruiter DJ, Burger PC. Angiogenesis in brain tumors; pathobiological and clinical aspects. *J Neurooncol* 1997;32(3):253-265.
20. Schneider SW, Ludwig T, Tatenhorst L, et al. Glioblastoma cells release factors that disrupt blood-brain barrier features. *Acta Neuropathol (Berl)* 2004;107(3):272-276.
21. Tofts PS, Kermode AG. Measurement of the blood-brain barrier permeability and leakage space using dynamic MR imaging. 1. Fundamental concepts. *Magn Reson Med* 1991;17(2):357-367.
22. Li KL, Zhu XP, Checkley DR, et al. Simultaneous mapping of blood volume and endothelial permeability surface area product in gliomas using iterative analysis of first-pass dynamic contrast enhanced MRI data. *Br J Radiol* 2003;76(901):39-50.
23. Tofts PS, Brix G, Buckley DL, et al. Estimating kinetic parameters from dynamic contrast-enhanced T(1)-weighted MRI of a diffusable tracer: standardized quantities and symbols. *J Magn Reson Imaging* 1999;10(3):223-232.
24. Tofts PS. Modeling tracer kinetics in dynamic Gd-DTPA MR imaging. *J Magn Reson Imaging* 1997;7(1):91-101.
25. Roberts HC, Roberts TP, Brasch RC, Dillon WP. Quantitative measurement of microvascular permeability in human brain tumors achieved using dynamic

- contrast-enhanced MR imaging: correlation with histologic grade. *AJNR Am J Neuroradiol* 2000;21(5):891-899.
26. Jackson A, Jayson GC, Li KL, et al. Reproducibility of quantitative dynamic contrast-enhanced MRI in newly presenting glioma. *Br J Radiol* 2003;76(903):153-162.
 27. Miyati T, Banno T, Mase M, et al. Dual dynamic contrast-enhanced MR imaging. *J Magn Reson Imaging* 1997;7(1):230-235.
 28. Barbier EL, den Boer JA, Peters AR, Rozeboom AR, Sau J, Bonmartin A. A model of the dual effect of gadopentetate dimeglumine on dynamic brain MR images. *J Magn Reson Imaging* 1999;10(3):242-253.
 29. Vonken EP, van Osch MJ, Bakker CJ, Viergever MA. Simultaneous quantitative cerebral perfusion and Gd-DTPA extravasation measurement with dual-echo dynamic susceptibility contrast MRI. *Magn Reson Med* 2000;43(6):820-827.
 30. Heiland S, Benner T, Debus J, Rempp K, Reith W, Sartor K. Simultaneous assessment of cerebral hemodynamics and contrast agent uptake in lesions with disrupted blood-brain-barrier. *Magn Reson Imaging* 1999;17(1):21-27.
 31. Cha S, Knopp EA, Johnson G, et al. Dynamic contrast-enhanced T2-weighted MR imaging of recurrent malignant gliomas treated with thalidomide and carboplatin. *AJNR Am J Neuroradiol* 2000;21(5):881-890.
 32. Aronen HJ, Gazit IE, Louis DN, et al. Cerebral blood volume maps of gliomas: comparison with tumor grade and histologic findings. *Radiology* 1994;191(1):41-51.
 33. Cha S, Johnson G, Wadghiri YZ, et al. Dynamic, contrast-enhanced perfusion MRI in mouse gliomas: correlation with histopathology. *Magn Reson Med* 2003;49(5):848-855.
 34. Guckel F, Brix G, Rempp K, Deimling M, Rother J, Georgi M. Assessment of cerebral blood volume with dynamic susceptibility contrast enhanced gradient-echo imaging. *J Comput Assist Tomogr* 1994;18(3):344-351.
 35. Knopp EA, Cha S, Johnson G, et al. Glial neoplasms: dynamic contrast-enhanced T2*-weighted MR imaging. *Radiology* 1999;211(3):791-798.
 36. Chan A, Nelson S. Simplified gamma variate fitting of perfusion curves. 2004. p 1067-1070.
 37. Kassner A, Annesley DJ, Zhu XP, et al. Abnormalities of the contrast recirculation phase in cerebral tumors demonstrated using dynamic susceptibility contrast-enhanced imaging: a possible marker of vascular tortuosity. *J Magn Reson Imaging* 2000;11(2):103-113.

38. Weisskoff RM, Boxerman JL, Sorensen AG, Kulke SM, Campbell TA, Rosen BR. Simultaneous blood volume and permeability mapping using a single Gd-based contrast injection. 1994; San Francisco. p 279.
39. Benner T, Heiland S, Erb G, Forsting M, Sartor K. Accuracy of gamma-variate fits to concentration-time curves from dynamic susceptibility-contrast enhanced MRI: influence of time resolution, maximal signal drop and signal-to-noise. *Magn Reson Imaging* 1997;15(3):307-317.
40. Cha S, Lu S, Johnson G, Knopp EA. Dynamic susceptibility contrast MR imaging: correlation of signal intensity changes with cerebral blood volume measurements. *J Magn Reson Imaging* 2000;11(2):114-119.
41. Jackson A, Kassner A, Zhu XP, Li KL. Reproducibility of T2* blood volume and vascular tortuosity maps in cerebral gliomas. *J Magn Reson Imaging* 2001;14(5):510-516.
42. Chan A, Pirzkall A, Nelson S. Analysis of serial changes in perfusion parameters for patients with recurrent high grade gliomas being treated with radiosurgery. 2004; Kyoto, Japan.
43. Jackson A, Kassner A, Annesley-Williams D, Reid H, Zhu XP, Li KL. Abnormalities in the recirculation phase of contrast agent bolus passage in cerebral gliomas: comparison with relative blood volume and tumor grade. *AJNR Am J Neuroradiol* 2002;23(1):7-14.
44. Rosen BR, Belliveau JW, Vevea JM, Brady TJ. Perfusion imaging with NMR contrast agents. *Magn Reson Med* 1990;14(2):249-265.
45. Provenzale JM, Wang GR, Brenner T, Petrella JR, Sorensen AG. Comparison of permeability in high-grade and low-grade brain tumors using dynamic susceptibility contrast MR imaging. *AJR Am J Roentgenol* 2002;178(3):711-716.
46. Law M, Yang S, Wang H, et al. Glioma grading: sensitivity, specificity, and predictive values of perfusion MR imaging and proton MR spectroscopic imaging compared with conventional MR imaging. *AJNR Am J Neuroradiol* 2003;24(10):1989-1998.
47. Griebel J, Mayr NA, de Vries A, et al. Assessment of tumor microcirculation: a new role of dynamic contrast MR imaging. *J Magn Reson Imaging* 1997;7(1):111-119.
48. Law M, Yang S, Babb JS, et al. Comparison of cerebral blood volume and vascular permeability from dynamic susceptibility contrast-enhanced perfusion MR imaging with glioma grade. *AJNR Am J Neuroradiol* 2004;25(5):746-755.

49. Rueckert D, Sonoda LI, Hayes C, Hill DL, Leach MO, Hawkes DJ. Nonrigid registration using free-form deformations: application to breast MR images. *IEEE Trans Med Imaging* 1999;18(8):712-721.
50. Studholme C, Hill D, Hawkes D. An overlap invariant entropy measure of 3D medical image alignment. *Pattern Recognition* 1999;32:71-86.
51. Chang L, McBride D, Miller BL, et al. Localized in vivo 1H magnetic resonance spectroscopy and in vitro analyses of heterogeneous brain tumors. *J Neuroimaging* 1995;5(3):157-163.
52. Crawford F, Cha S, Lupo JM, et al. Predicting the emergence of contrast enhancement in glioblastoma multiforme using bolus tracking perfusion MRI. 2004 May 17-21, 2004; Kyoto, Japan.
53. Andersen C, Jensen FT. Differences in blood-tumour-barrier leakage of human intracranial tumours: quantitative monitoring of vasogenic oedema and its response to glucocorticoid treatment. *Acta Neurochir (Wien)* 1998;140(9):919-924.
54. Jensen RL. Growth factor-mediated angiogenesis in the malignant progression of glial tumors: a review. *Surg Neurol* 1998;49(2):189-195; discussion 196.
55. Allen N. Oxidative metabolism of brain tumors. *Prog Exp Tumor Res* 1972;17:192-209.
56. Alger JR, Frank JA, Bizzi A, et al. Metabolism of human gliomas: assessment with H-1 MR spectroscopy and F-18 fluorodeoxyglucose PET. *Radiology* 1990;177(3):633-641.
57. Evans SM, Koch CJ. Prognostic significance of tumor oxygenation in humans. *Cancer Lett* 2003;195(1):1-16.
58. Herholz K, Heindel W, Luyten PR, et al. In vivo imaging of glucose consumption and lactate concentration in human gliomas. *Ann Neurol* 1992;31(3):319-327.
59. Gillies RJ, Morse DL. In Vivo Magnetic Resonance Spectroscopy in Cancer. *Annu Rev Biomed Eng* 2004.
60. Howe FA, Barton SJ, Cudlip SA, et al. Metabolic profiles of human brain tumors using quantitative in vivo 1H magnetic resonance spectroscopy. *Magn Reson Med* 2003;49(2):223-232.
61. McBride DQ, Miller BL, Nikas DL, et al. Analysis of brain tumors using 1H magnetic resonance spectroscopy. *Surg Neurol* 1995;44(2):137-144.

62. Star-Lack J, Vigneron DB, Pauly J, Kurhanewicz J, Nelson SJ. Improved solvent suppression and increased spatial excitation bandwidths for three-dimensional PRESS CSI using phase-compensating spectral/spatial spin-echo pulses. *J Magn Reson Imaging* 1997;7(4):745-757.
63. Nelson SJ. Analysis of volume MRI and MR spectroscopic imaging data for the evaluation of patients with brain tumors. *Magn Reson Med* 2001;46(2):228-239.
64. McKnight TR, Noworolski SM, Vigneron DB, Nelson SJ. An automated technique for the quantitative assessment of 3D-MRSI data from patients with glioma. *J Magn Reson Imaging* 2001;13(2):167-177.
65. Gill SS, Thomas DG, Van Bruggen N, et al. Proton MR spectroscopy of intracranial tumours: in vivo and in vitro studies. *J Comput Assist Tomogr* 1990;14(4):497-504.
66. Li X, Lu Y, Pirzkall A, McKnight T, Nelson SJ. Analysis of the spatial characteristics of metabolic abnormalities in newly diagnosed glioma patients. *J Magn Reson Imaging* 2002;16(3):229-237.
67. Star-Lack J, Spielman D, Adalsteinsson E, Kurhanewicz J, Terris DJ, Vigneron DB. In vivo lactate editing with simultaneous detection of choline, creatine, NAA, and lipid singlets at 1.5 T using PRESS excitation with applications to the study of brain and head and neck tumors. *J Magn Reson* 1998;133(2):243-254.
68. Li X, Vigneron DB, Cha S, et al. Relationship of MR-derived lactate, mobile lipids, and relative blood volume for gliomas in vivo. *AJNR Am J Neuroradiol* 2005;26(4):760-769.
69. Li X, Graves EE, Vigneron DB, Cha S, McKnight TR, Nelson SJ. Reliable estimate of lactate and lipid for newly-diagnosed glioma patients using lactate-edited 3D 1H-MRSI with ellipsoidal k-space sampling. 2003 July 2003; Toronto, Ontario, Canada.
70. Pirzkall A, McKnight TR, Graves EE, et al. MR-spectroscopy guided target delineation for high-grade gliomas. *Int J Radiat Oncol Biol Phys* 2001;50(4):915-928.
71. Tran TK, Vigneron DB, Sailasuta N, et al. Very selective suppression pulses for clinical MRSI studies of brain and prostate cancer. *Magn Reson Med* 2000;43(1):23-33.
72. Heiland S, Kreibich W, Reith W, et al. Comparison of echo-planar sequences for perfusion-weighted MRI: which is best? *Neuroradiology* 1998;40(4):216-221.

73. Frayne R, Goodyear BG, Dickhoff P, Lauzon ML, Sevick RJ. Magnetic resonance imaging at 3.0 Tesla: challenges and advantages in clinical neurological imaging. *Invest Radiol* 2003;38(7):385-402.
74. Hu X, Norris DG. Advances in high-field magnetic resonance imaging. *Annu Rev Biomed Eng* 2004;6:157-184.
75. Pruessmann KP. Parallel imaging at high field strength: synergies and joint potential. *Top Magn Reson Imaging* 2004;15(4):237-244.
76. Yang QX, Wang J, Smith MB, et al. Reduction of magnetic field inhomogeneity artifacts in echo planar imaging with SENSE and GESEPI at high field. *Magn Reson Med* 2004;52(6):1418-1423.
77. Norris DG. High field human imaging. *J Magn Reson Imaging* 2003;18(5):519-529.
78. Pruessmann KP, Weiger M, Scheidegger MB, Boesiger P. SENSE: sensitivity encoding for fast MRI. *Magn Reson Med* 1999;42(5):952-962.
79. Griswold MA, Jakob PM, Heidemann RM, et al. Generalized autocalibrating partially parallel acquisitions (GRAPPA). *Magn Reson Med* 2002;47(6):1202-1210.
80. Wald LL, Carvajal L, Moyher SE, et al. Phased array detectors and an automated intensity-correction algorithm for high-resolution MR imaging of the human brain. *Magn Reson Med* 1995;34(3):433-439.
81. de Zwart JA, Ledden PJ, van Gelderen P, Bodurka J, Chu R, Duyn JH. Signal-to-noise ratio and parallel imaging performance of a 16-channel receive-only brain coil array at 3.0 Tesla. *Magn Reson Med* 2004;51(1):22-26.
82. Stollberger R, Fazekas F. Improved perfusion and tracer kinetic imaging using parallel imaging. *Top Magn Reson Imaging* 2004;15(4):245-254.
83. Zhang Y, Brady M, Smith S. Segmentation of brain MR images through a hidden Markov random field model and the expectation-maximization algorithm. *IEEE Trans Med Imaging* 2001;20(1):45-57.
84. Lupo J, Cha S, Chang SM, Nelson SJ. Dynamic susceptibility-weighted perfusion imaging of high-grade gliomas: characterization of spatial heterogeneity. *AJNR Am J Neuroradiol* 2005;27(4).
85. Studholme C, Constable RT, Duncan JS. Accurate alignment of functional EPI data to anatomical MRI using a physics-based distortion model. *IEEE Trans Med Imaging* 2000;19(11):1115-1127.

86. Wang J, Reykowski A, Dickas J. Calculation of the signal-to-noise ratio for simple surface coils and arrays of coils. *IEEE Trans Biomed Eng* 1995;42(9):908-917.
87. Manka C, Traber F, Gieseke J, Schild HH, Kuhl CK. Three-dimensional dynamic susceptibility-weighted perfusion MR imaging at 3.0 T: feasibility and contrast agent dose. *Radiology* 2005;234(3):869-877.
88. Golay X, Pruessmann KP, Weiger M, et al. PRESTO-SENSE: an ultrafast whole-brain fMRI technique. *Magn Reson Med* 2000;43(6):779-786.
89. Haacke EM, Xu Y, Cheng YC, Reichenbach JR. Susceptibility weighted imaging (SWI). *Magn Reson Med* 2004;52(3):612-618.
90. Sehgal V, Delproposito Z, Haacke EM, et al. Clinical applications of neuroimaging with susceptibility-weighted imaging. *J Magn Reson Imaging* 2005;22(4):439-450.
91. Sehgal V, Delproposito Z, Haddar D, et al. Susceptibility-weighted imaging to visualize blood products and improve tumor contrast in the study of brain masses. *J Magn Reson Imaging* 2006;24(1):41-51.
92. Reichenbach JR, Barth M, Haacke EM, Klarhofer M, Kaiser WA, Moser E. High-resolution MR venography at 3.0 Tesla. *J Comput Assist Tomogr* 2000;24(6):949-957.
93. Sedlacik J, Herrmann KH, Rauscher A, Reichenbach JR. SWI using different k-space undersampling mechanisms. 2005; Miami, Florida.
94. Haacke E, Lai S, Reichenbach JR. In vivo measurement of blood oxygen saturation using magnetic resonance imaging: a direct validation of the blood-oxygen level-dependent concept in functional brain imaging. *Human Brain Mapping*;5:341-346.
95. Weisskoff RM, Kiihne S. MRI susceptometry: image-based measurement of absolute susceptibility of MR contrast agents and human blood. *Magn Reson Med* 1992;24(2):375-383.
96. Barth M, Nobauer-Huhmann IM, Reichenbach JR, et al. High-resolution three-dimensional contrast-enhanced blood oxygenation level-dependent magnetic resonance venography of brain tumors at 3 Tesla: first clinical experience and comparison with 1.5 Tesla. *Invest Radiol* 2003;38(7):409-414.
97. Rauscher A, Barth M, Reichenbach JR, Stollberger R, Moser E. Automated unwrapping of MR phase images applied to BOLD MR-venography at 3 Tesla. *J Magn Reson Imaging* 2003;18(2):175-180.
98. Jenkinson M. Fast, automated, N-dimensional phase-unwrapping algorithm. *Magn Reson Med* 2003;49(1):193-197.

99. Lee MC, Cha S, Chang SM, Nelson SJ. Partial-volume model for determining white matter and gray matter cerebral blood volume for analysis of gliomas. *J Magn Reson Imaging* 2006;23(3):257-266.

Handwritten text, likely bleed-through from the reverse side of the page. The text is extremely faint and illegible due to the high contrast and low resolution of the scan. It appears to be a list or series of entries, possibly containing names and dates, but the characters are too light to be accurately transcribed.

7541991



3 1378 00754 1991

For Not to be taken
from the room.
reference

